

DISSERTATION

LASER IGNITION FOR INTERNAL COMBUSTION ENGINES

VIA FIBER OPTIC DELIVERY

Submitted by

Morgan DeFoort

Department of Mechanical Engineering

In partial fulfillment of the requirements

For the Degree of Doctor of Philosophy

Colorado State University

Fort Collins, Colorado

Summer, 2009



UMI Number: 3385168

All rights reserved

INFORMATION TO ALL USERS

The quality of this reproduction is dependent upon the quality of the copy submitted.

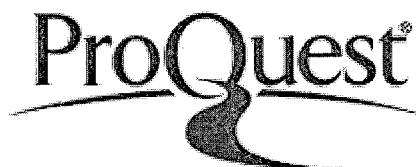
In the unlikely event that the author did not send a complete manuscript and there are missing pages, these will be noted. Also, if material had to be removed, a note will indicate the deletion.



UMI 3385168

Copyright 2009 by ProQuest LLC.

All rights reserved. This edition of the work is protected against unauthorized copying under Title 17, United States Code.



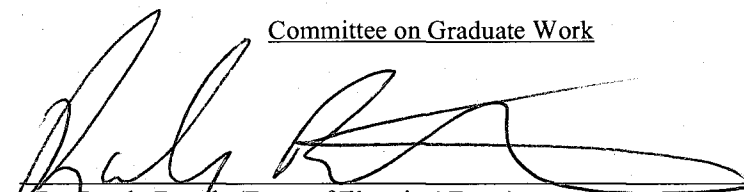
ProQuest LLC
789 East Eisenhower Parkway
P.O. Box 1346
Ann Arbor, MI 48106-1346

COLORADO STATE UNIVERSITY

3, November 2008

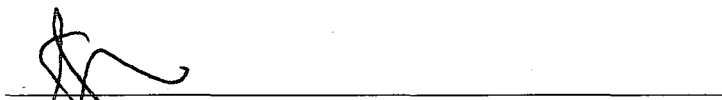
WE HEREBY RECOMMEND THAT THE DISSERTATION PREPARED UNDER OUR SUPERVISION BY MORGAN DEFOORT ENTITLED "LASER IGNITION FOR INTERNAL COMBUSTION ENGINES VIA FIBER OPTIC DELIVERY" BE ACCEPTED AS FULFILLING IN PART REQUIREMENT FOR THE DEGREE OF DOCTOR OF PHILOSOPHY.

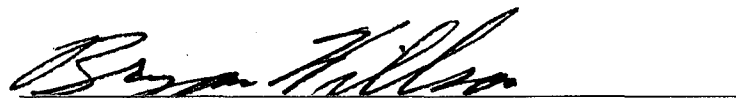
Committee on Graduate Work


Dr. Randy Bartels (Dept. of Electrical Engr.)


Dr. George Collins (Dept. of Electrical Engr.)


Dr. Daniel Olsen (Dept. of Mechanical Engr.)


Dr. Azer Yalin (Adviser)


Dr. Bryan Willson (Co-Adviser)


Dr. Allan Kirkpatrick (Department Head)

ABSTRACT OF DISSERTATION
LASER IGNITION FOR INTERNAL COMBUSTION ENGINES
VIA FIBER OPTIC DELIVERY

In the effort to reduce emissions and improve the efficiency of Otto cycle engines, the ignition system is often a limiting factor. Many “high energy” ignition systems have been developed, but almost all of these are based on traditional electric arc spark plugs. Laser ignition represents a fundamentally different approach to igniting gas mixtures and opens the door to improvements in fuel-lean engine operation and high-pressure combustion environments. Yet the promise of laser ignition remains unexploited, as practical systems have not been developed. In this contribution, we work towards the goal of developing a practical laser ignition system for stationary natural gas engines. Specifically, we focus on fiber optic delivery of the laser beam to the engine, thereby making a significant advance relative to past open-air (free-space) configurations. A combination of modeling and experimentation has been used to develop the needed fiber optic delivery systems, culminating in the first demonstration of fiber-optically delivered laser ignition on an engine.

Morgan W. DeFoort
Department of Mechanical Engineering
Colorado State University
Fort Collins, CO 80523
Summer, 2009

TABLE OF CONTENTS

1	Chapter One - Introduction	1
1.1	The Importance of Natural Gas Engines	1
1.2	Improved Ignition for Increased Efficiency & Reduced Emissions	4
1.3	Limitations of Conventional Electric Spark Ignition.....	6
1.3.1	<i>Spark Creation in an Electric Spark Plug</i>	6
1.3.2	<i>Spark Plug Erosion</i>	8
1.3.3	<i>High BMEP operation</i>	10
1.3.4	<i>Spark Location and Heat Losses</i>	12
1.4	Introduction to Laser Ignition.....	13
1.5	Motivation for Fiber Optically Delivered Laser Ignition	15
2	Chapter Two - Laser Spark Ignition	18
2.1	Phenomenological Description.....	18
2.1.1	<i>Spark Formation</i>	18
2.1.2	<i>Plasma Kernel Expansion and Blast Wave Generation</i>	20
2.1.3	<i>Transition of Plasma Kernel to Flame Front</i>	22
2.1.4	<i>Phenomenological Summary</i>	23
2.2	Parametric Dependencies for Electron Cascade Spark Formation	25
2.3	Key Differences of Laser versus Conventional Ignition	31
2.4	Engine Combustion Benefits of Laser Ignition	34
3	Chapter Three - Laser Ignition via Fiber Optic Delivery	38
3.1	Challenges of Fiber Optic Delivery	38

3.1.1	<i>Delivering light via fiber optics</i>	38
3.1.2	<i>Intensity Damage Threshold</i>	46
3.2	Figure of Merit Development for Fiber Selection	49
3.3	FOM Evaluation of Fiber Candidates.....	52
3.3.1	<i>Solid Core Fibers</i>	52
3.3.2	<i>Hollow Core Fibers</i>	54
3.3.3	<i>Photonic Crystal Fibers</i>	55
3.3.4	<i>Fiber Laser</i>	56
4	Chapter Four - Development of Focusing Optics	59
5	Chapter Five - Fiber Optic Testing and Characterization	70
5.1	Experimental Evaluation of Tapered Solid Core Fibers.....	70
5.2	Experimental Evaluation of Rigid Hollow Core Fibers	75
5.3	Experimental Evaluation of Coated Hollow Core Fibers.....	76
5.3.1	<i>Fiber design and manufacturing</i>	77
5.3.2	<i>Power Transmission and Limits</i>	79
5.3.3	<i>Output Beam Quality & Effect of Launch NA</i>	81
5.3.4	<i>Sparking Demonstration</i>	82
6	Chapter Six - Development of an Optical Spark Plug	87
7	Chapter Seven - Engine Testing	93
7.1	Introduction.....	93
7.2	Optical Design	93
7.2.1	<i>Optical Train</i>	94
7.2.2	<i>Vibration Isolation</i>	99
	Test Results	102
7.2.3	<i>Ignition Reliability</i>	104

7.2.4	<i>Rate of Pressure Rise</i>	104
7.2.5	<i>Mass Fraction Burned</i>	105
7.3	Combustion Stability	107
8	Chapter Eight – Conclusion	109
9	Appendix A: Peak Pressure Plot	113
10	Appendix B: Engine Data	115
11	Appendix C: U.S. Patent # 7340129	117
12	Appendix D: Cylinder Pressure Trace	144
13	Appendix E: Engine Data	146

1 Chapter One - Introduction

1.1 The Importance of Natural Gas Engines

Every day in the United States almost 2 billion cubic meters of natural gas is distributed through 3.5 million kilometers of interstate pipeline, of which approximately one-third is used to generate electricity [1]. Natural gas is increasingly the fuel of choice for generating electricity. In the year 2000, over 23,000 MW of new electric capacity was added in the United States, of this almost 95 percent was fueled by natural gas. As shown in Figure 1-1, the majority of the new electricity generation capacity for the next 15 years is expected to utilize natural gas, primarily because natural-gas-fired generators are projected to continue to have advantages over coal-fired generators including higher fuel efficiency and lower emissions².

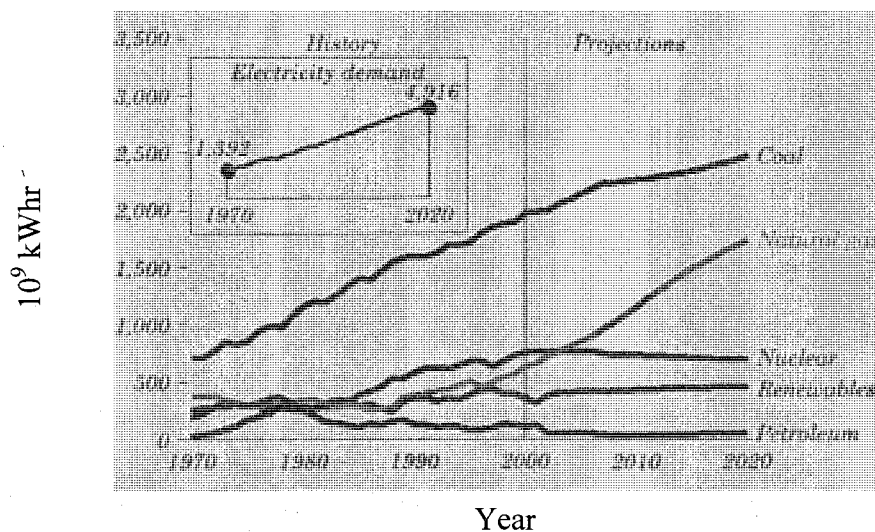


Figure 1-1
Electricity generation by fuel 1970-2020 (billion kilowatt hours) [1].

Reciprocating natural gas engines are currently the fastest-selling and lowest cost type of distributed generation technology. With typical efficiencies between 37 and 44 percent, and installed costs of approximately \$400-450 per kilowatt [3], reciprocating engines meet or exceed current stationary fuel cell efficiencies, with 1/10th to 1/100th of the installed cost per kilowatt [4].

To develop the next generation of natural gas engine technology, the United States Department of Energy established the ARES (Advanced Reciprocating Engine Systems) program with the goals of achieving the following advances:

- improved fuel efficiency and flexibility
- lessened dependence on foreign sources of fuel
- ultra-low emissions
- lower cost power technologies
- improved power system and grid reliability

The ARES program brought together engine manufacturers (Caterpillar, Cummins, and Waukesha) with several national laboratories (Argonne National Laboratory, National Energy Technology Laboratory, and Oak Ridge National Laboratory) and universities (including Colorado State University). At Colorado State University's Engine and Energy Conversion Laboratory, research focusing on laser ignition systems is aimed at partially fulfilling ARES goals related to efficiency and emissions, more specifically:

- 1) High Efficiency – The ARES target for fuel-to-electricity conversion efficiency (low heating value) is 50 percent by 2010, a significant increase from today's average efficiency of typically 38 percent. And,

- 2) Low Emissions – The program has established a NO_x target for gas reciprocating engines of 0.1 g/hp-hr, a 95% decrease from today's NO_x emissions rate.

1.2 Improved Ignition for Increased Efficiency & Reduced Emissions

Karl Benz, while designing the first automobile, called ignition the “problem of problems”, yet given today’s advanced ignition systems utilizing electronic timing, shaped waveforms, and exotic electrode materials, for many applications the ignition problem has essentially been solved. However, in large-bore, high BMEP (brake mean effective pressure), fuel-lean natural gas engines, ignition remains a limiting factor, both in terms of extending the lean limit of the engine and in terms of increasing the BMEP.

Because of its stable chemical structure, natural gas is inherently a difficult fuel to ignite; the flammability range of methane (the primary constituent of natural gas) is limited to an equivalence ratio (ratio of stoichiometric air/fuel ratio to actual air/fuel ratio) of $\Phi = 0.46$ to $\Phi = 1.64$. By comparison, hydrogen has a flammability range of $\Phi = 0.14$ to $\Phi = 2.54$ ⁵. Thus, there is a relatively narrow range of natural gas / air mixtures that will readily combust. To achieve low emissions and high efficiency, lean equivalence ratios are desired. As the lean limit is approached, the increased availability of oxygen leads to more complete combustion (each fuel molecule is more likely to find an oxygen molecule), thereby reducing products of incomplete combustion, which improves efficiency. The increased concentrations of air also lower flame temperatures, reducing thermal (Zeldovich) NO_x formation.

Engine operation near the lean flammability limit is difficult to achieve owing to increased cycle-to-cycle variation of peak pressure. These variations are due to failed or incomplete ignition associated with variations in fuel/air homogeneity (mixing), gas motion in the cylinder, or residual exhaust from un-burnt fuel from previous cycles.

These cycle-to-cycle variations result in unsteady engine performance. Additionally, cycles in which the mixture only partially burns or fails to ignite entirely (i.e. misfires) lead to increased engine emissions. Misfires and partial burns also result in unutilized fuel and thus an efficiency penalty. Based on these considerations, potential improvements in emissions and efficiency are limited by the ability of the engine to maintain reliable and repeatable ignition at lean air/fuel ratios.

Improved ignition systems have been explored as a means to extend the engine's lean operating limit. Novel variations of the traditional electric arc spark plug have been developed, however, all such concepts have fundamental limitations inherent to electric arcs. These limitations, along with turbo-charging, bound the maximum achievable BMEP in industrial natural gas engines. The equation for mechanical efficiency ($\eta_{mech} = BMEP / (BMEP - IMEP)$) shows that as BMEP increases, overall mechanical efficiency (η_{mech}) increases (where IMEP is the indicated mean effective pressure), thus ignition also becomes a limiting factor on efficiency. The limitations of electric arc systems with respect to BMEP will be further discussed in section 1.3.3.

1.3 Limitations of Conventional Electric Spark Ignition

Virtually all stationary, natural gas engines use some form of electric spark ignition. Figure 1-2 illustrates the layout and components of a typical electric spark plug. While spark plugs in themselves are relatively simple devices, a complete ignition system is a highly developed piece of equipment. Although there are many electrode configurations, the overall concept is fundamentally the same, with the design consisting of a center electrode separated by a gap from one or multiple ground electrodes.

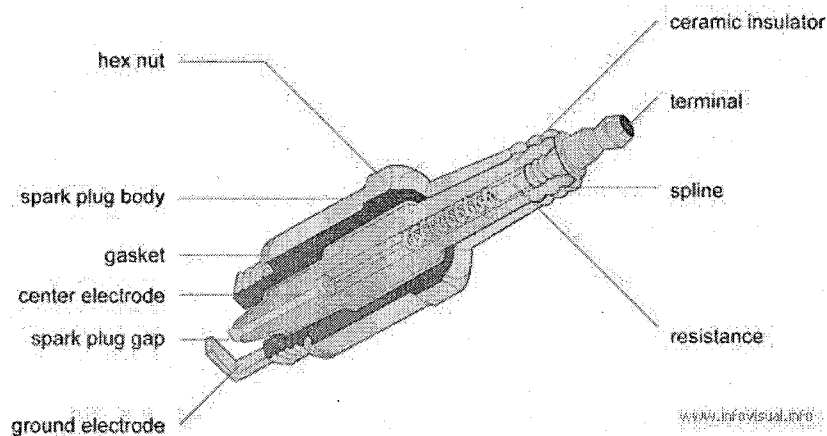


Figure 1-2
Schematic diagram of a typical electric spark plug⁶

1.3.1 Spark Creation in an Electric Spark Plug

To create a spark a sufficient voltage is applied across the spark gap. Typical time dependences of current and voltage are shown in Figure 1-3. There are four distinct phases of an electric arc ignition event, beginning with the predischage phase. At the beginning of this phase the voltage increases until the gaseous mixture in the gap breaks

down (begins to ionize). Ionizing streamers eventually bridge the gap between the two electrodes. The resulting ionization channel provides a circuit or conduction pathway that greatly lowers the resistance of the circuit and allows current to flow between the two electrodes. The point at which current begins to flow marks the transition from the predischage phase to the breakdown phase. During the breakdown phase, the voltage is relatively high (kilovolts), while the current climbs from $\sim 10^{-2}$ to $\sim 10^2$ amperes as the impedance falls. Though the total energy transferred to the mixture is small in this phase of ignition, it is very efficient; the energy transferred to the mixture is high compared to other losses. The total duration of the breakdown phase is relatively short; on the order of a few nanoseconds.

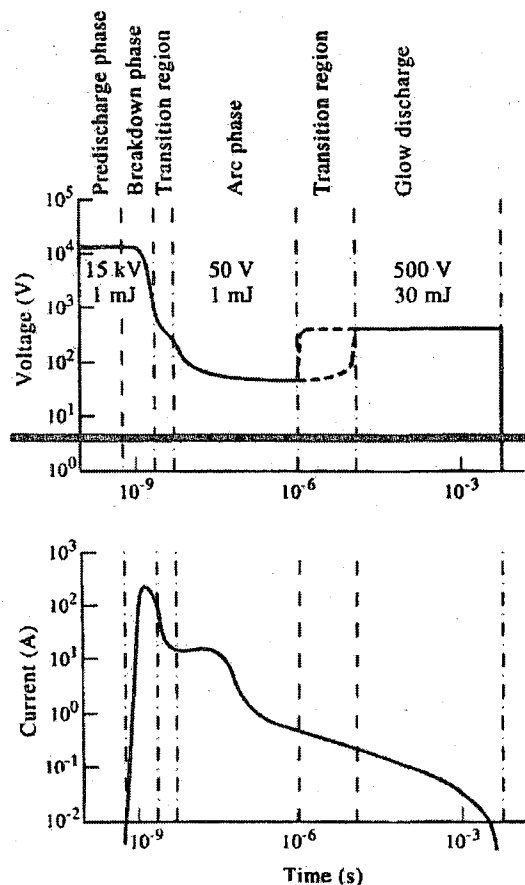


Figure 1-3 Schematic of voltage and current variation with time during an electric spark [7].

The establishment of a low impedance conduction pathway marks the transition from breakdown phase to arc phase. In the arc phase of ignition, the current rapidly decreases. The voltage reduces from approximately $\sim 10^4$ volts to less than ~ 100 volts. The current plateaus from $\sim 10^1 - 10^2$ amps to ~ 1 amp, as the resistance of the circuit temporarily stabilizes. Because of heat conduction and mass diffusion out of the arc region, the temperature is limited to about 6000 K, an order of magnitude lower than the breakdown phase [7].

The final phase of the electrical spark process is the glow discharge, which may last several orders of magnitude longer than the previous phases. During this phase the current will drop below ~ 0.1 amps. The cathode is relatively cold and has a large voltage drop of $\sim 300-500$ V. The ionization fraction falls to approximately 10^{-4} .

As advanced engines push toward improved efficiency and reduced emissions through leaner mixtures and higher pressures, the task of the spark plug becomes increasingly demanding. Higher powers, longer arc durations, increased voltage, and multiple strikes per stroke have all been used to enhance ignition, but these improvements reduce spark plug life for traditional electric spark plugs.

1.3.2 Spark Plug Erosion

In the case of large stationary natural gas engines, a single cylinder can see over a billion ignition events, with a single spark plug surviving roughly 10 million ignition events over its lifetime. The process of creating a spark is a violent one from the perspective of an electrode. The spark process can rapidly erode electrodes through the ejection of charged particles, vaporization of electrode material, and thermal swings so

rapid that electrodes crack and flake apart. The rates at which these mechanisms occur are determined by many different factors including spark gap length, electrode material, size, and shape, temperature, chemical environment, and the manner in which energy is delivered to the spark plug. The primary erosion mechanisms can be summarized as follows:

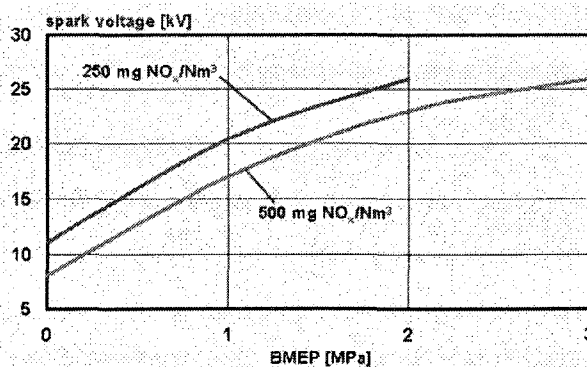
- Removal of material at the atomic scale occurring as a result of ion bombardment [8] (also referred to as sputtering). In the sputtering process cations in the gas collide with the negative electrode with enough kinetic energy to eject atoms from the surface of the electrode leading to erosion [9,10].
- Small pools of molten metal form on the spark plug during the electric arc. These liquid metal pools are highly susceptible to erosion. The momentum of the ion arc itself can eject droplets of molten metal. When the ion arc ceases, the surface tension of the liquid can cause the liquid to pull back on itself and eject a drop of molten metal [11].
- Solid bits of material erode as a result of oxidation, corrosion, and joule heating of the electrodes. If thermal energy is transferred to the electrode faster than it is dissipated, thermal stresses develop leading to fractures and material removal [12].
- Oxidation occurs when atoms in the electrode lose electrons allowing them to easily combine with oxygen, thereby forming metal oxides on the

surface of the electrode. These layers tend to be brittle and can flake away [13].

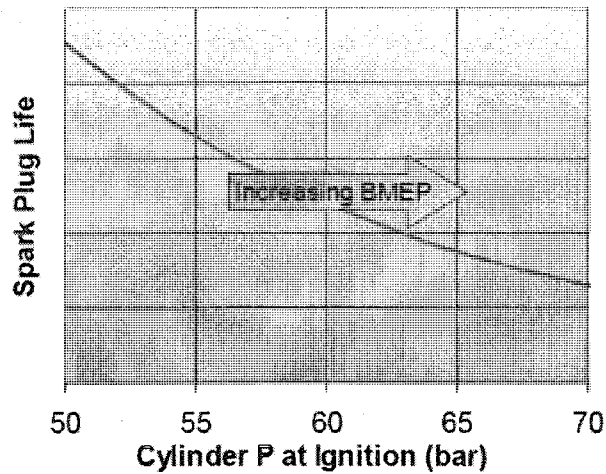
Current lifetimes of typical electric gap spark plugs for high BMEP natural gas engines are on the order of 2-6 months (continuous duty). The goal for the ARES program is an ignition system lifetime of one year or more [14].

1.3.3 High BMEP operation

Today's engine manufacturers desire high in-cylinder pressures to achieve high BMEP operation, which has incumbent emissions and efficiency benefits. In Figure 1-4a one can see that as BMEP is increased, spark voltage must also increase to maintain a constant NO_x emission level. However, increasing spark plug voltage has adverse effects upon spark plug life, as shown in Figure 1-4



(a)



(b)

Figure 1-4

a) Spark voltage vs. BMEP (Jenbacher¹⁵) b) BMEP (as described by cylinder pressure) vs. spark plug life (Cummins¹⁶).

Higher voltages are required to breakdown air at elevated pressures (high BMEP). This relationship between breakdown voltage and pressure is described by Paschen's Law [17] which (at the conditions of interest) dictates that as pressure increases the electric field strength required for breakdown also increases. (The increase is due to the high number density of particles which limits the acceleration of electrons or ions.)

The higher voltage leads to accelerated electrode wear (shorter spark plug life) through the mechanisms previously described, as well as (inadvertent) breakdown in the dielectric separating the electrodes. Dielectric breakdown can be caused by both thermal and electrical mechanisms [18]. Thermal stress is caused by repeated heating of the dielectric and can cause cracking and conduction pathways, while electrical breakdown is caused by the injection of electrons or holes into the dielectric as a result of high strength electric fields.

1.3.4 Spark Location and Heat Losses

Traditional spark plugs also are limited in regards to their physical structure and location in the cylinder. Any protruding or sharp surface in the cylinder will rapidly heat up and become a source for auto-ignition. This fact, along with the path of the piston, limits the suitable locations for the ignition site (spark plug electrode) to locations in close proximity to the surface of the piston head. However, in large bore engines, inhomogeneities in the gas mixture (i.e. locally rich or lean regions) may not be compatible with these possible spark plug locations. Also, because the location of the spark is inherently close to the electrodes, heat losses from the flame kernel to the spark plug electrodes have an adverse impact on flame kernel development (and can limit achievable lean limits). Pischinger et al. demonstrated that smaller diameter electrodes reduced heat losses and thereby extended the stable operating range of the engine [19] (though the smaller electrodes have shorter life spans). The same research also showed that cyclic variations in heat losses to electrodes were related to cyclic variations in flame kernel contact area with those electrodes. These variations were shown to effect initial flame kernel development and thus peak power produced from the cycle.

1.4 Introduction to Laser Ignition

Laser ignition represents a fundamentally different approach to igniting a flammable mixture as compared to the electric arcs created by traditional spark plugs. Many of the limitations of traditional ignition systems can be avoided: There are no quenching electrodes, the location of the spark is much less constrained, plug erosion is no longer an issue, and as will be further discussed, the different breakdown mechanism gives different pressure dependence and ignition physics. Of course, new practical challenges such as cost, cleanliness of the window, reliability, and beam delivery must be addressed.

The phenomenon of laser ignition was first reported in 1963 by Maker et al. [20]. It is interesting to note that just six years later, DeMichelis published a biographical review citing over 160 papers published on the subject [21]. DeMichelis concluded that all laser induced sparks are created in one of two ways: either through multi-photon ionization or cascade ionization. Many years later, Santavicca et al. [22] identified three methods for laser induced breakdown: laser induced photochemical ignition, laser induced thermal ignition (cascade ionization), and laser induced spark ignition (multi-photon ionization). These methods will be examined in the next chapter. In general; however, laser ignition occurs when a pulsed laser beam with sufficient energy is focused into a small region. The local intensity causes the gas to breakdown and form a spark (plasma). As will be further discussed, the underlying physics of spark formation due to electrical and optical breakdown are different. Therefore, in addition to spark location and lack of electrodes, the differing properties of laser and electric sparks opens the door

to other potential advantages of laser ignition. Indeed, a large body of engine test results shows benefits of increased lean limits, reduced emissions, and elevated efficiencies. These results are discussed in the following chapter.

1.5 Motivation for Fiber Optically Delivered Laser Ignition

Despite the potential benefits, laser ignition systems are not found in commercial use. A key limitation has been the open-path beam delivery used in the vast majority of laboratory research. At a Department of Energy Roundtable meeting in 2003, motivations for fiber delivery were discussed. The conclusion drawn between researchers and members of industry was that any practical laser ignition system would need to confine the laser beam.

The first argument for beam containment is safety. The laser intensities required for ignition are high enough to cause permanent eye damage. People working in and around engines (who are generally not familiar with lasers) must be protected from exposure. A collimated laser beam could reflect from engine surfaces causing eye damage, or the user could inadvertently put themselves in the intended beam path.

A second argument for beam containment is the engine environment itself. An open path system would need to compensate for heavy vibration, particulates in the beam path, thermal drift, misalignment, and engine geometries, which are often complex.

One approach to the beam containment problem, explored by several groups [23,24] is the use of a complete laser system on each cylinder of the engine. While the approach has benefits, such as a very simple optical path, the cost of equipment necessary to outfit each cylinder on a production engine with an individual laser is likely prohibitive. In addition, the environment near the engine cylinder is (in terms of temperature and vibration) not conducive to laser operation.

Another approach is to fiber-optically deliver laser pump light (as opposed to the high-power ignition pulse) from a single source to multiple laser rods or amplifiers located on each cylinder. While this approach allows for simple fiber optics (as the requirements for delivery of pump light are less stringent than for the ignition pulse) it still requires the complexity (and cost) of laser gain elements at each cylinder.

Therefore, the approach taken in this work is to use a single laser, which can be multiplexed to multiple cylinders through high power fiber optic cables. This approach is challenging with respect to the requirements of the fiber optic cables (as will be discussed), but if achievable, it presents a potentially low-cost and practical solution to beam delivery.

-
- ¹ U.S. Energy Information Administration (Department of Energy). Web site: www.eia.doe.gov.
- ² Hutzler. (2002). *EIA Annual Energy Outlook 2002 With Projections to 2020*. Web site: [www.eia.doe.gov/oiaf/archive/aeo02/pdf/0383\(2002\).pdf](http://www.eia.doe.gov/oiaf/archive/aeo02/pdf/0383(2002).pdf).
- ³ (2001). "Distributed Energy Resources" *February 2001 DOE Advanced Reciprocating Engines Program Publication*. Web site: www.eere.energy.gov
- ⁴ Services, Parsons. (2000). *Fuel Cell Handbook (Fifth Edition)*. Web site: <http://www.fuelcells.org/info/library/fchandbook.pdf>.
- ⁵ Turns. (2000). *An Introduction to Combustion*. McGraw Hill Publishing, Second Edition.
- ⁶ Graphic from http://www.infovisual.info/05/012_en.html
- ⁷ Heywood. (1998). *Internal Combustion Engine Fundamentals*. McGraw-Hill.
- ⁸ Kalghatgi. (1987). "Spark Ignition, Early Flame Development and Cyclic Variation in I.C. Engines". *Society of Automotive Engineers*. 870163.
- ⁹ Nishio, Oshima, and Ogura. (1994). "A Study on Spark Plug Electrode Shape". *International Journal of Vehicle Design*, 15, 119-130.
- ¹⁰ Donaldson, Kristiansen, Watson. (1986). "Electrode erosion in high current, high energy transient arcs". *Magnetics, IEEE Transactions* 22(6).
- ¹¹ Gray, Pharney. (1974). "Electrode erosion by particle ejection in low-current arcs". *Journal of Applied Physics*. 45, 667.
- ¹² Donaldson. (1990). "Electrode Erosion in High Current, High Energy Transient Arcs", *Thesis (Ph. D.)*, Texas Tech University
- ¹³ Pischinger, Stefan, Heywood. (1990). "How Heat Losses to the Spark Plug Electrodes Affect Flame Kernel Development in an SI-Engine". *Society of Automotive Engineers*. 900021.
- ¹⁴ Baldwin, Gerber. (2005). *DOE Distributed Energy Peer Review*, Arlington VA.
- ¹⁵ Herdin, Klausner. (2005). "Laser Ignition - a New Concept to Use and Increase the Potentials of Gas Engines". *Proceedings of ICEF2005 ASME Internal Combustion Engine Division 2005 Fall Technical Conference*. ICEF2005-1352.
- ¹⁶ zur Loye. (2005). "ARES Technology Development for the Cummins QSK60 Natural Gas Engine" *2nd Annual Advanced Stationary Reciprocating Engines Conference*. March 15-16, 2005, Diamond Bar, CA.
- ¹⁷ Raizer. (1997). *Gas Discharge Physics*. Springer Verlag.
- ¹⁸ Hickmott. (2006). "Formation of Ohmic contacts: A breakdown mechanism in metal-insulator-metal structures" *Journal Of Applied Physics*. 100, 083712.
- ¹⁹ Pischinger, Stefan, Heywood. (1990). "How Heat Losses to the Spark Plug Electrodes Affect Flame Kernel Development in an SI-Engine". *Society of Automotive Engineers*. 900021.
- ²⁰ Maker. (1964). *Optical third harmonic generation Quantum Electronics III*, New York: Columbia University Press.
- ²¹ DeMichelis. (1969). "Laser Induced Gas Breakdown: A Bibliographical Review". *IEE Journal of Quantum Electronics*. QE-5, 4.
- ²² Santavicca, Ho, Reilly, Lee. (1991). "Laser Induced Spark Ignition of Methane-Oxygen Mixtures." *National Aeronautics and Space Administration*.
- ²³ Brinkmann. (2004). "In situ laser diode replaces spark plug", *Laser Focus World*. 10, 31-33.
- ²⁴ McMillian, Woodruff, Richardson, McIntyre, (2004). "Laser Spark Ignition: Laser Development and Engine Testing". *Proceedings of ECEF2004 ASME Internal Combustion Engine Division 2004 Fall Technical Conference*. ICEF 2004-917.

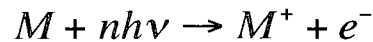
2 Chapter Two - Laser Spark Ignition

2.1 Phenomenological Description

2.1.1 Spark Formation

The nature of the physical process leading to the formation of a laser spark depends on the conditions of both the laser delivery and the mixture to be ignited. The different mechanisms of laser spark formation can be categorized as: multiphoton ionization, electron cascade ionization, or photochemical ionization [1].

Multiphoton ionization (Equation 2-1) is the process in which several photons are absorbed by an atom or molecule of the gas:

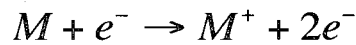


Equation 2-1

where M represents a neutral atom or molecule, n is the number of photons, h is Planck's constant, and ν is the frequency of radiation. For most practical cases, a single photon is not able to directly ionize the gas as its energy level is too low, for example, the fundamental wavelength of a Nd:YAG laser is 1.064 μm corresponding to a photon energy of 1.17 eV while most atmospheric gases have higher ionization potentials (on the order of 10 eV). The probability of an atom simultaneously absorbing n photons is proportional to the energy of the laser's electric field to the power $2n$ [1]. When sufficient photon energy is absorbed, the atom will eject an electron, thus becoming

ionized. The accumulation of electrons is linear with time [2] and if the field is strong enough and of adequate duration, a plasma will form.

In the electron cascade model, one assumes that a small number of electrons appear in the beam focus region due to impurity heating, multiphoton ionization, or excitation by cosmic rays. These electrons are accelerated and acquire energy from the electric field by the absorption of photons (inverse bremsstrahlung), leading to energetic collisions and ionization of the neutral gas atoms. When an electron ionizes an atom, a second electron is produced allowing initiation of a cascade process and avalanche (exponential) breakdown. The chemical formula for electron impact ionization can be given as:



Equation 2-2

where M represents an atom or molecule, and e is an electron. Because two electrons exist after the reaction, the build-up of electrons in an electron cascade is exponential in time [1, 2, 3].

Photochemical ionization can occur when the laser wavelength is tuned to match an absorption wavelength of the target atoms or molecules. Absorbed photons dissociate the target molecules into reactive radicals leading to combustion and/or ionization. Though very effective at creating an ignition event even at low energies or species concentrations, photochemical ionization is generally at a practical disadvantage due to the requirement of a tuned laser, which generally increases system complexity and cost [3]. Furthermore, the approach has only been demonstrated in a limited range of mixtures.

In practice, a combination of the multiphoton and electron cascade mechanisms is usually involved in laser ignition. For the pressure and wavelength regime found in internal combustion engines, it has been determined that the dominant mechanism for the ionization process in laser based gas breakdown is the electron cascade [4]. However, for an electron cascade to occur seed photons must first exist. These seed photons are most likely generated though the multiphoton ionization process [1].

2.1.2 Plasma Kernel Expansion and Blast Wave Generation

If the ignition parameters are amenable, a spark will be formed which has the ability to propagate a flame. The flame propagation process is now described from a phenomenological perspective using data from various researchers that have explored the early processes of laser ignition.

Initially, the plasma kernel formed by the laser spark rapidly expands due to its intense heat and pressure relative to the surrounding gas. A blast wave expands radially with the kernel and by $\sim 1-3\mu\text{s}$ after the initial breakdown the plasma has expanded to an oval shape with a typical dimension $\sim 1-2\text{ mm}$ [5,6]. The blast wave then detaches from the kernel, having two primary effects: transporting energy away from the ignition spot and causing a temperature increase in the surrounding gas [8]. This shock wave propagates in a manner consistent with Taylor's spherical blast wave theory and is described in detail by Bradley [7].

Lackner investigated the early stages of laser-induced ignition of methane/air mixtures in a combustion test chamber at pressures up to 25 bar [8]. Stoichiometric to

fuel-lean mixtures were ignited using an Nd:YAG laser with pulse duration of 5ns, pulse energy of 50mJ, operating at a wavelength of 1.064 nm. Schlieren photography was utilized to observe the ignition kernel and subsequent shock waves and flame front formation.

In the left of Figure 2-1, two shock waves (from a single laser pulse) are clearly seen. The photo is taken in air at a pressure of 25 bar, the diameter of the shockwave is proportional to the energy deposited and is ~ 10 mm. While an unusual case, the photo is useful in that it shows how the propagation of the shockwave is related to the original laser spark. Less energy was deposited in the left region, so the resulting shock wave is smaller. On the right, a multi-exposure photo shows the development of the shockwave. In a methane/air mixture at 10 bar, the plasma will be ~ 2 mm in diameter at about 100 μ s after the laser pulse. After ~ 700 μ s the shock wave will grow to ~ 550 mm (in a sufficiently large vessel).

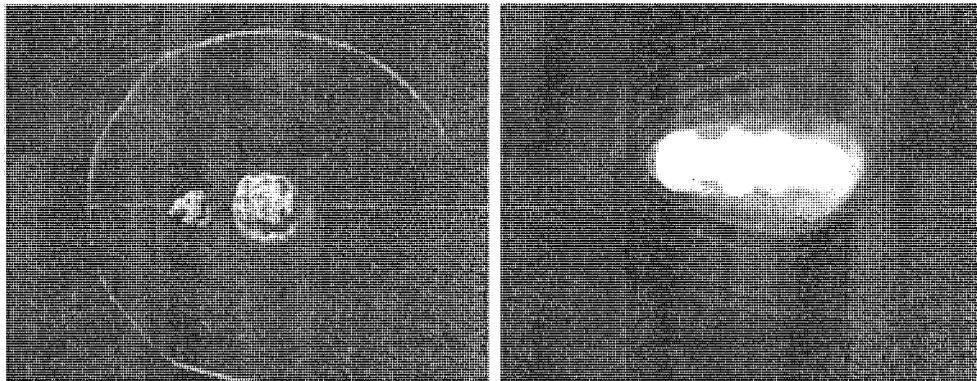


Figure 2-1
Schlieren images of methane air ignition [8].

2.1.3 Transition of Plasma Kernel to Flame Front

The initial shockwave velocity is orders of magnitude higher than the flame front velocity. Once the flame kernel is established, the shockwave has already slowed. Lackner reports shockwaves with velocities between 2000 and 5000 m/s which dissipate approximately 3000 ns after formation. Laser induced fluorescence (LIF) images were obtained and used to visualize the formation of OH radicals during the ignition event. The images in Figure 2-2 show the unique geometry of the fully developed laser induced ignition kernel. A doughnut shaped flame front on the left side of the kernel is associated with the gas-dynamic effect of the strong energy deposition on the side of the kernel closest to the laser (ride side).

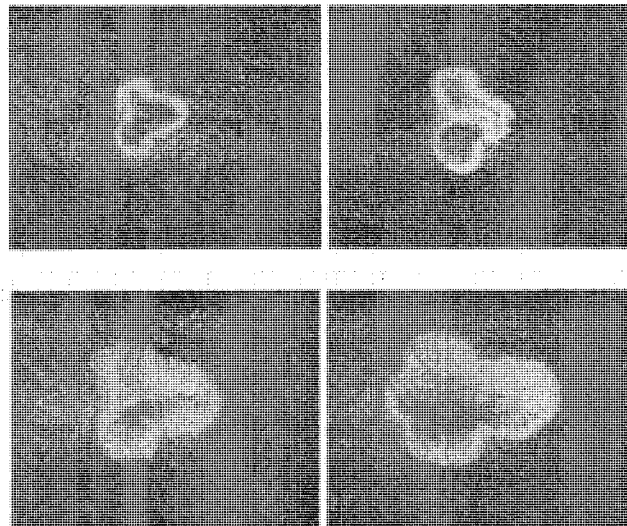


Figure 2-2

Planar laser-induced fluorescence images of the OH radical. The ignition laser entering from the right side. Conditions: $\lambda = 1.0$; CH_4/air , 25 bar. Image widths are 18 mm. Timing: (from left to right) 0.2, 0.5, 1.5, and 2.5 ms after ignition. [18]

The increase in energy deposition to the “upstream” side of the kernel can be explained by the fact that as a plasma is formed in the focal region, the area becomes opaque, allowing a greater percentage of energy to be deposited into the gas on the side of the plasma which is facing the beam. Lackner notes that these features (shape and dynamics) of the early plasma kernel are closely tied to the early flame growth and thus are thought to have a significant influence on early flame propagation. These laser ignited flame kernels tend to have high flame speeds, causing them to be thermally overdriven (temperature increases even as kernel expands). In such cases it is suggested that this overdrive may allow the kernel to avoid extinction in the early time period when flame stretch hinders flame growth (discussed in more detail in section 2.3).

2.1.4 Phenomenological Summary

From the literature cited previously, the complete process leading to laser ignition can be described. The sketch below is adapted from [2]. In (a) photons are absorbed through multiphoton ionization to produce initial electrons. These seed electrons absorb energy from incident photons through an inverse bremsstrahlung process.

These energized electrons collide with other neutral atoms or molecules ejecting more electrons leading to an electron cascade (b). In (c) the plasma begins to form in the focal region. The laser incidence is from left right, causing the plasma to grow from right to left. The plasma, now opaque, readily absorbs laser energy. In (d) the shock wave begins to expand into the volume, while in (e) a toroid shaped flame kernel grows.

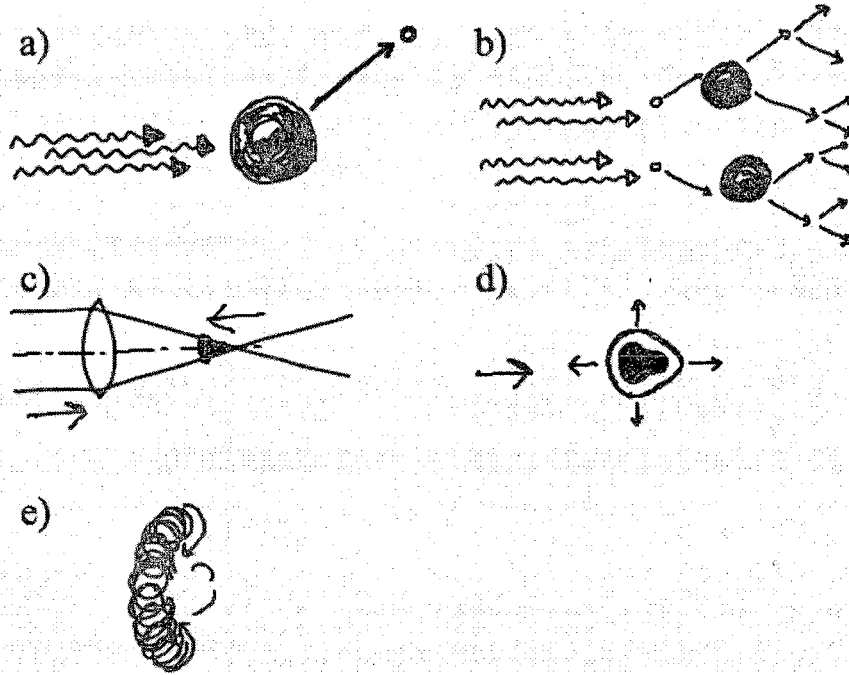


Figure 2-3
Simplified visual depiction of steps of laser ignition.

2.2 Parametric Dependencies for Electron Cascade Spark Formation

The required initiating conditions and properties of a breakdown spark vary based on laser and optical conditions (pulse duration, laser wavelength, beam quality, pulse energy, focusing optics), as well as gas conditions (composition, temperature, pressure). In this section, the parametric dependencies of key properties are discussed.

Breakdown Intensity

For the conditions of our interest, i.e. nanosecond pulses and ignition of lean fuel/air mixtures at elevated pressures, breakdown of the gas requires that the optical intensities in the spark formation region exceed a threshold value. The spatially-averaged intensity can be estimated as:

$$I = P / \pi r^2$$

Equation 2-3

where I is intensity, P is power (pulse energy divided by pulse duration), and r is the radius of the spark. Thus, to accurately report the intensity, a calculation or direct measurement of the beam dimension is required. This idea is discussed in the following chapters and plays an important role in the use of fiber optics to deliver optical pulses. Most breakdown thresholds in the literature are based on open-path optics and high spatial quality lasers, corresponding to radially symmetric Gaussian beam profiles. If this is the case and if a collimated beam is focused with a lens, then (neglecting aberrations) the beam waist (approximately equal to the radius) is given as:

$$w = \left(\frac{2\lambda}{\pi} \right) \left(\frac{f}{d} \right)$$

Equation 2-4

where λ is the laser wavelength, f is the focal length of the focusing lens, and d is the beam diameter. Typical values for an Nd:YAG laser operating at the fundamental wavelength of 1.064 μm , with a beam diameter of 5 mm, pulse length of 8 ns and pulse energy of 40 mJ, are a beam waist of 7 μm and an intensity of $\sim 3.4 \times 10^{12}$ W/cm². In practice, lens aberrations may increase the focal spot size and lower the intensity. While the required irradiance is dependent of pressure and mixture composition (discussed below), typical threshold values for spark formation in air at atmospheric pressures are on the order of 10^{11} - 10^{12} W/cm² [9]. As will be discussed, achieving the needed high intensities with fiber delivered beams is significantly more difficult than for open path beams.

Pressure and Wavelength

Multiphoton ionization is the prominent mechanism for spark formation at low pressures and short wavelengths [10]. For example, for a CO₂ laser with a wavelength of 10.6 μm , each photon has an energy of 0.1 eV, so that ~ 120 photons are required to reach the ionization potential of oxygen (12 eV). On the other hand, for an Nd:YAG laser with a wavelength of 1064 nm each photon has an energy of ~ 1 eV, so that only 12 photons would need to be absorbed. Thus, the multiphoton ionization mechanism is far more likely to occur at shorter laser wavelengths.

At the elevated pressures (> 1 atm) of interest, the electron cascade mechanism is dominant [3, 10]. This is largely because the process relies on collisions between free electrons and neutral atoms or molecules, and as the mean free path decreases (due to higher pressures) collision frequencies increase. However, the multiphoton ionization process remains important because of the need for initial electrons for the electron cascade mechanism to occur, these electrons most likely being created by multiphoton ionization.

There is a strong correlation between breakdown thresholds and pressure for the electron cascade mechanism. As the pressure is increased, collision rates are increased, promoting the cascade spark formation and causing reduction in the breakdown intensity threshold. For example, Phouc measured breakdown thresholds of combustion gases experimentally using a pulsed Nd:YAG laser operating at both the fundamental (1.064 μm) and the second harmonic (532 nm) [10]. The breakdown thresholds were measured for a range of pressures from 0.2 – 4 bar. Intensities in the range of 10^{12} - 10^{13} W/cm^2 were required for breakdown.

Figure 2-5 shows the results of Phouc's measurements of breakdown thresholds in multiple gases [3]. A pressure dependence of breakdown threshold is proportional to p^{-n} with values of n ranging from 0.4 to 0.78. The pressure dependence is stronger at shorter wavelengths, which is postulated to be due to diffusion losses out of the focal volume being greater at these wavelengths.

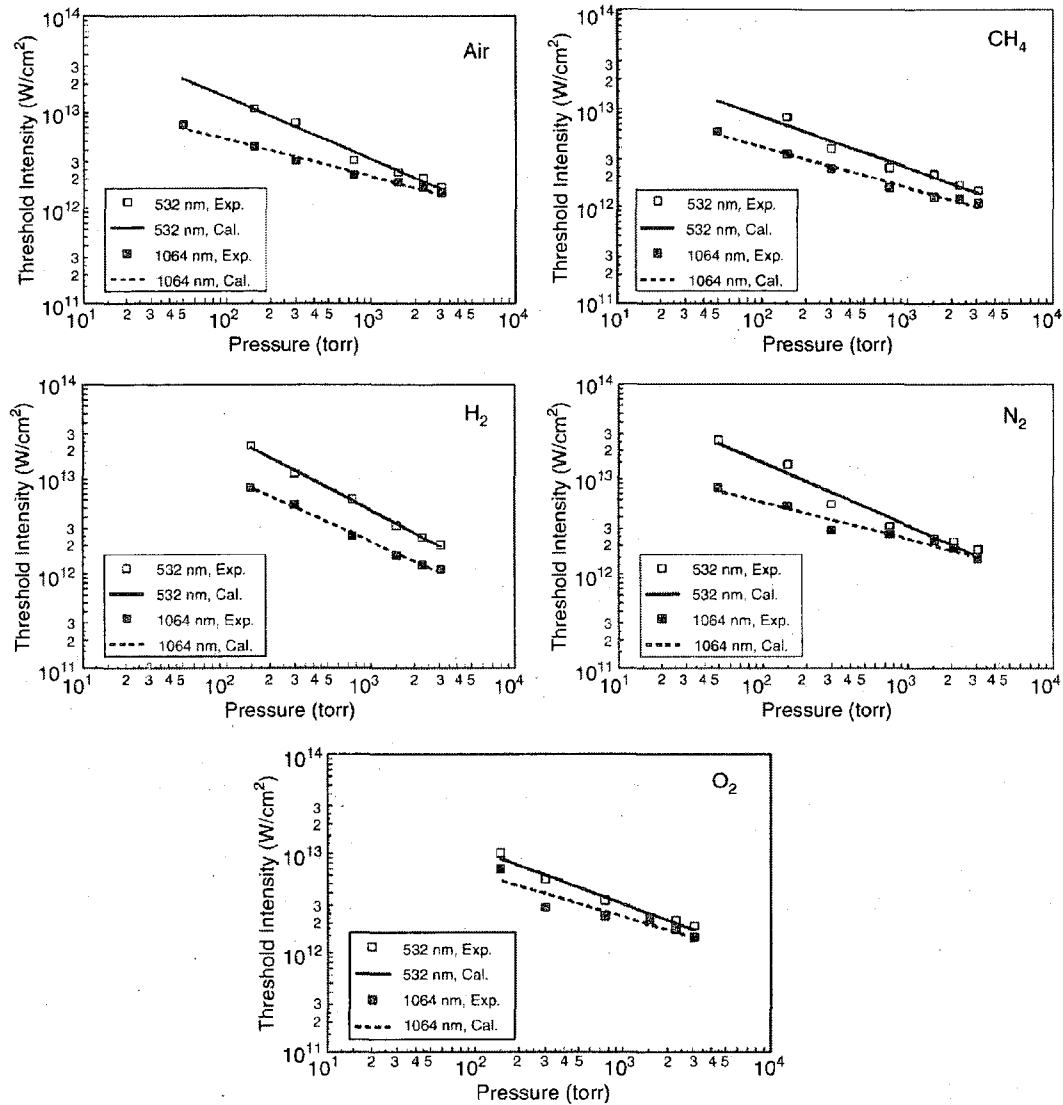


Figure 2-5
Breakdown thresholds in air, CH₄, H₂, N₂, and O₂ as a function of pressure and wavelength; (Nd:YAG laser at 532 and 1064 nm, and 5.5 ns pulse) [3].

Similar results have been found by other researchers, Chytek [11] measured the breakdown threshold for helium, argon, xenon, and clean air using a Nd:YAG laser operating at 532 nm. A pressure dependence was found similar to that of Phouc. Values of n ranged from 0.62 to 1.30. Chytek also concluded that at high pressures (greater than 0.5 bar) the electron cascade mechanism was dominant.

Composition (Air/Fuel Ratio)

Creation of a laser spark (breakdown) does not guarantee ignition of a mixture. Indeed, it is observed that a minimum energy must be delivered to the mixture for that spark to initiate combustion. The minimum ignition energy (MIE) requirement depends (in addition to pressure) on the air to fuel ratio and the flammability range of the combustible mixture. Because natural gas engines are central to this work, and methane is the primary component of natural gas, previous research into the MIE of methane/air mixtures is of primary interest.

Figure 2-6 is a plot of MIE for several experiments in the literature tabulated by Kopecek et al [7,8]. Tests vary in laser wavelength and pulse duration for different percentages of methane (or equivalence ratios).

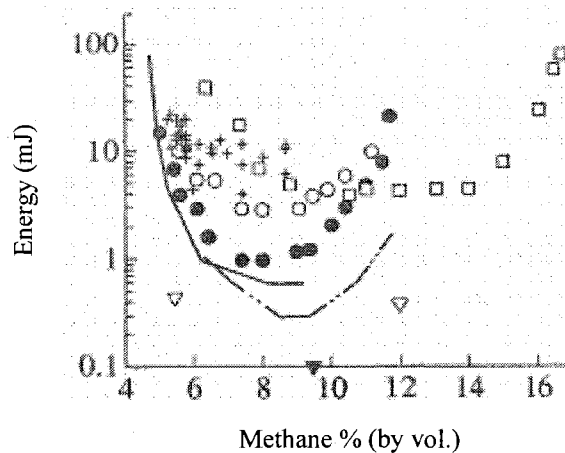


Figure 2-6

Results for minimum laser pulse energy needed for ignition, vertical axis is energy in mJ, and horizontal axis is methane % by volume [7]. See discussion in text.

Kopecek's data (+) used an Nd:YAG laser operating at 1.064 μm , with a pulse duration of about 8 ns and a multimode beam. Phouc data (\square) is also an Nd:YAG laser at 1.064

μm with a pulse duration of 5.5 ns [12]. Minimum ignition energy of 4 mJ is found for stoichiometric air/fuel ratios at atmospheric pressure. Lewis and von Elbe [13] data (dashed line) give minimum ignition energies for traditional electric spark. Data from Ronney [14] is also plotted both at ns pulse widths (\odot) and ps pulse widths (\circ). Data points from Sloane [15] (∇) at first appear low but are explained by the fact that they are ignited using photochemical ignition.

The data shows that the required energy for ignition is highly dependent on the air/fuel ratio of the mixture, with stoichiometric mixtures having the lowest energy requirement by approximately two orders of magnitude.

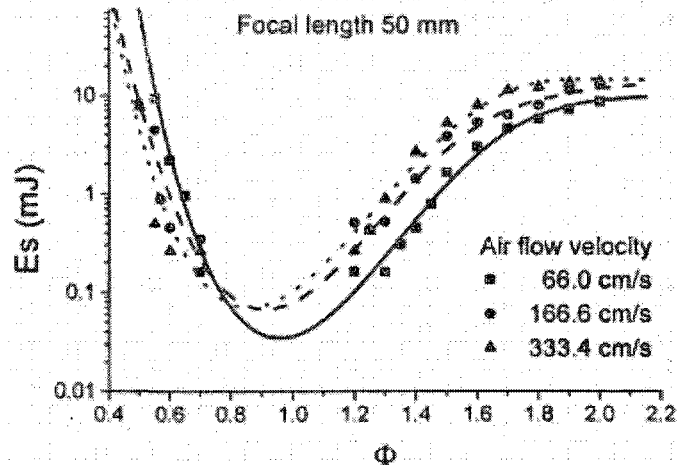


Figure 2-7
Minimum ignition energy as a function of equivalence ratio.

Beduneau performed a parametric study to characterize the effects of air fuel ratio on minimum ignition energy [16]. A premixed burner was ignited at atmospheric pressure while the equivalence ratio was varied. Figure 2-7 plots MIE against equivalence ratio at various air flow velocities in a methane air mixture. Typical mean velocities in an engine during the ignition process are on the order of 5 cm/s [17].

2.3 Key Differences of Laser versus Conventional Ignition

Neglecting the hardware configuration, the difference in timescale is the most dramatic difference between laser ignition and conventional ignition. A typical laser spark might last 8 ns and deliver 40 mJ of energy, while a conventional spark ignition system might deliver >100 mJ of energy to the spark over a period of milliseconds [18]. As a result, the laser ignition event will have a peak power ~150,000 times higher for the same energy [18]. In Figure 2-8 the timescales of the ignition process are shown. Along with OH graphics of a flame kernel during formation, and a typical pressure trace for combustion in a reciprocating engine.

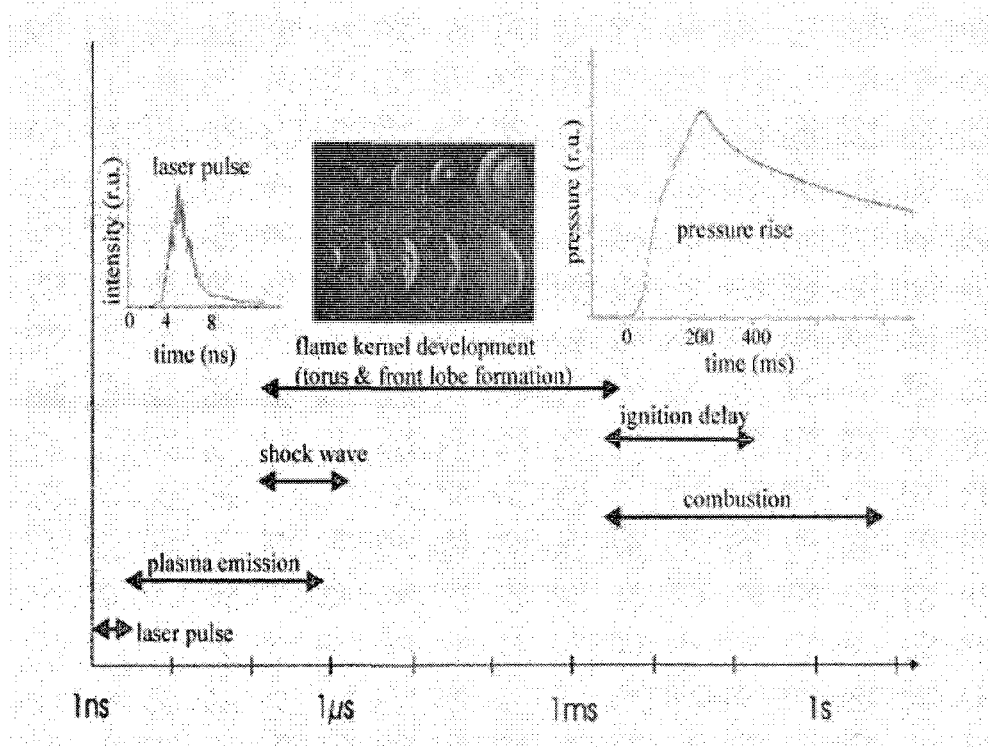


Figure 2-8
Timescales for laser ignition and subsequent combustion [16].

As discussed in section 2.1.3, the laser spark provides overdriven (elevated) early flame speeds which can aid in early ignition. These overdriven flame speeds are caused by high plasma energies of the laser spark and subsequent gasdynamic effects of the plasma expansion [7]. Flame speeds in the kernel, initially 5-20 times greater than those of laminar flames, reduce to those of normalized laminar flames over a period of 1.0 –1.5 ms, duration a sufficient duration for the ignition kernel to significantly expand thereby greatly decreasing the chance of extinction.

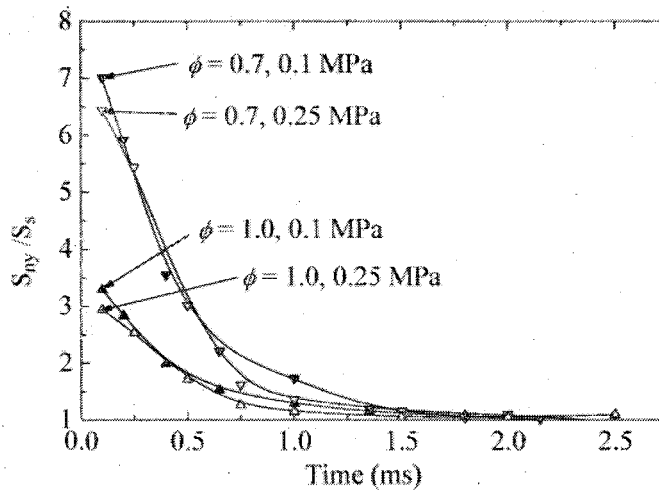


Figure 2-9
Ratio of measured flame speeds (S_{0y}) to unstretched laminar flame speeds (S_s) vs. time.

In addition to the differences in plasma properties, the differing hardware configurations lead to differences between laser and conventional ignition. Most importantly, there are no heat losses to electrodes in the laser ignition process, whereas for conventional ignition systems heat losses to the electrodes may account for 50-70% of the energy originally delivered to the spark plug [17]. Thus the laser ignition process delivers energy more efficiently to the mixture. Note that the total energy required for ignition is irrelevant to the overall efficiency of the engine, but is important in the sense

that heat losses to the electrodes contributes to their failure. Replacement of those electrodes is expensive in terms of both material costs and downtime for operators of industrial natural gas engines.

The pressure dependence between the physical processes of spark and laser ignition are also opposite (as previously discussed). Therefore, as engine technology drives in-cylinder pressures higher and higher, laser ignition systems become increasingly favorable (in terms of creating a spark) while conventional systems require higher voltages to achieve breakdown, resulting in increased electrode erosion.

Finally, due to shorter induction times and elevated early flame speeds, laser ignition has a shorter ignition delay and early burn duration compared to conventional ignition systems, allowing for decreased cycle-to-cycle variations in combustion parameters. This fact will be discussed in greater detail in Chapter 5.

2.4 Engine Combustion Benefits of Laser Ignition

Laser ignition is one of several advanced ignition systems capable of improving the quality of combustion in an engine. High energy ignition systems are of particular interest in natural gas engines because of the inherent difficulty in igniting methane mixtures previously discussed. These systems are capable of extending the lean operating limit, decreasing specific fuel consumption, and increasing indicated power [19]. The extent to which any of these effects will occur is highly dependent on the operating conditions of the engine. In this section, we discuss quantifiable benefits provided by laser ignition for engine operation.

Ochel et al. [19] showed that with increasing ignition energy, even with a standard spark plug, NO_x emissions decreased, especially at air fuel ratios near stoichiometric. Herdin et al. [20] also showed significantly decreased NO_x emissions from laser as compared to pre-chamber and diesel pilot ignition systems (Figure 2-10).

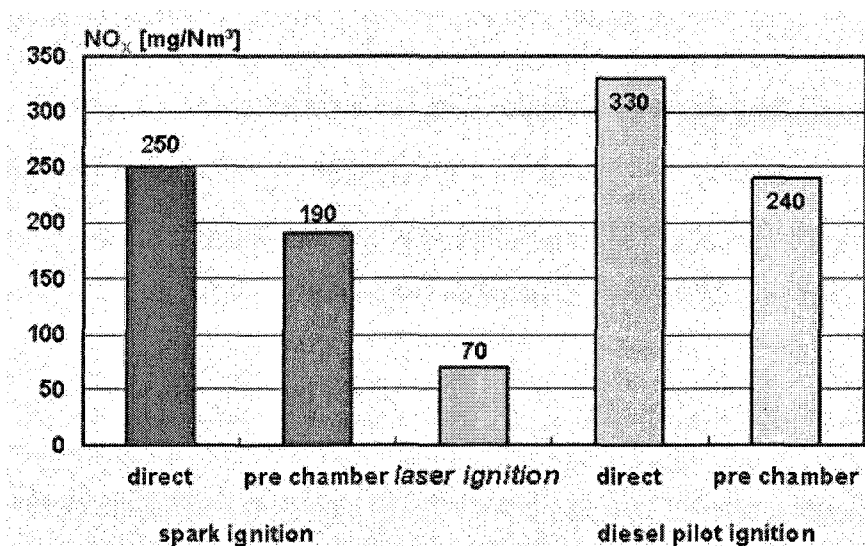


Figure 2-10
 NO_x emissions of various ignition sources.

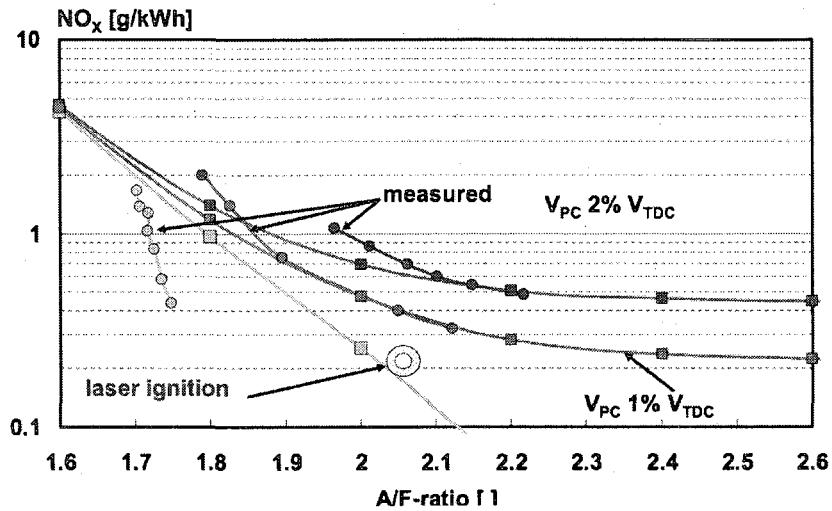


Figure 2-11
NO_x emissions of laser ignition vs. conventional ignition vs. air/fuel ratio.

This improvement in NO_x emissions (Figure 2-11) is not due to a fundamental change in combustion, but the ability of the ignition system to maintain stable combustion at leaner air fuel ratios. The decrease in NO_x emissions and increase in efficiency are thereby achieved indirectly through the ability to run an engine stably at higher air/fuel ratios. This increase in the lean limit is due to the previously described flame kernel formed by through laser ignition, which is capable of delivering a greater amount of energy to the gas in a shorter duration.

There is a strong correlation between early flame growth and peak pressure, and that variations in the local (near spark plug) velocity field around the time of ignition result in significant cycle-to-cycle variations in flame kernel growth [21]. It is not desirable to decrease the flow velocities or turbulence in the engine as this would further exacerbate the problem of low flame speeds found in methane mixtures. Therefore it is more attractive to create a spark which is capable of withstanding turbulence (as would

be achieved with laser ignition), leading to a more reliable ignition event and a higher flame speed during the combustion process.

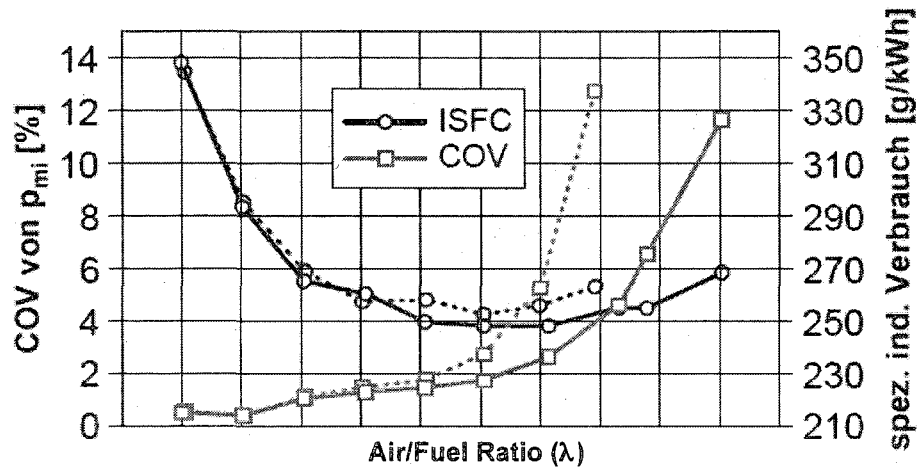


Figure 2-12
Decreased fuel consumption and COV of laser ignition (solid line is laser ignition) [20].

Once again, due to the overdriven nature of the flame kernel, the laser spark more frequently survives the expansion process even in lean or turbulent environments, resulting in a decreased COV (coefficient of variation) of peak pressure and decreased ISFC (indicated specific fuel consumption) as shown in Figure 2-12.

A final point of critical importance is that as advanced gas engine move to higher BMEP (> 15 bar) to increase efficiency, the erosion (and use) of conventional spark plugs becomes increasingly problematic (section 1.3.3).

-
- ¹ DeMichelis. (1969). "Laser Induced Gas Breakdown: A Bibliographic Review". *IEEE Journal of Quantum Electronics*. QE-5,188-202.
- ² Kandala, Candler. (2002). "Computational Modeling of Localized Laser Energy Deposition in Quiescent Air". *American Institute of Aeronautics and Astronautics*. 2002-2160.
- ³ Phouc. (2006). "Laser-induced Spark Ignition Fundamentals and Applications". *Optics and Engineering*. 44,51-397.
- ⁴ Rosen, Weyl. (1987). "Laser-Induced Breakdown in Nitrogen and the Rare Gases at 0.53 and 0.35 Micrometers". *Journal of Applied Physics D*. 20,1264-1276.
- ⁵ Spiglin. (1995). "Time-Resolved Imaging of Flame Kernels: Laser Spark Ignition of H₂/O₂/Ar mixtures". *Combustion and Flame*. 102,310-328.
- ⁶ Chen (2001). "Visualization of laser-induced breakdown and ignition". *Optics Express*. 9,499-503.
- ⁷ Bradley, Sheppard, Suardjaja, Woolley. (2004). "Fundamentals of high-energy spark ignition with lasers". *Combustion and Flame*. 138,55-77.
- ⁸ Lackner, Charareh. (2004). "Investigation of the early stages in laser-induced ignition by Schlieren photography and laser-induced fluorescence spectroscopy". *Optics Express*. 12(19).
- ⁹ Phouc, White. (2000). "Optical Characterization of the Laser-Induced Spark in Air" Web site: <http://www.igrant.demon.co.uk/PAPERS/Tran2.pdf>
- ¹⁰ Phouc. (2000). "Laser spark ignition: experimental determination of laser-induced breakdown thresholds of combustion gases". *Optics Communications*. 175(4-6),419-423.
- ¹¹ Chytek, Jarzembski. (1990). "Pressure Dependence of the Laser-induced breakdown thresholds of gases and droplets". *Applied Optics*. 29(15).
- ¹² Phuoc, White. (1999). "Single-point versus multi-point laser ignition: experimental measurements of combustion times and pressures". *Combustion and Flame*, 119, 203.
- ¹³ Lewis, von Elbe. (1987). *Combustion, Flames and Explosion of Gases*. Hartcourt Press. New York.
- ¹⁴ Lim, McIlroy, Ronney, Syage. (1996). "Detailed Characterization of Minimum Ignition Energies of Combustible Gases Using Laser Ignition Sources". *Transport Phenomena in Combustion*. 176-184.
- ¹⁵ Sloane. (1990). "Energy Requirements for Spherical Ignitions in Methane-Air Mixtures at Different Equivalence Ratios". *Combustion Science and Technology*. 73(1),351-365.
- ¹⁶ Beduneau. (2003). "Measurements of minimum ignition energy in premixed laminar methane/air flow by using laser induced spark". *Combustion and Flame*. 132,653-665.
- ¹⁷ Heywood. (1988). *Internal Combustion Engine Fundamentals*. McGraw-Hill.
- ¹⁸ Ma, Alexander, Poulain. (1998). "Laser Spark Ignition and Combustion Characteristics of Methane Air Mixtures". *Combustion and Flame*. 112,492-506.
- ¹⁹ Ochel, Hoad, Kornhauser, Vandsburger. (1995). "High Energy Ignition for NO_x Reduction in Natural Gas Engines" *American Society of Mechanical Engineers*. 95-ICE-3.
- ²⁰ Herdin, Klausner. (2005). "Laser Ignition - a New Concept to Use and Increase the Potentials of Gas Engines". *Proceedings of ICEF2005 ASME Internal Combustion Engine Division 2005 Fall Technical Conference, September 11-14, 2005, Ottawa, Canada*. ICEF2005-1352.
- ²¹ Olsen. (1998). "Lean-Burn Gas Engine Ignition Processes". Gas Research Institute Annual Report.

3 Chapter Three - Laser Ignition via Fiber Optic Delivery

3.1 Challenges of Fiber Optic Delivery

There are two key challenges associated with the use of high power fiber optic delivery; first is the difficulty in focusing fiber optically delivered light (particularly for multimode fibers) and second is the intensity damage threshold of the fiber optic material.

3.1.1 Delivering light via fiber optics

Conventional fiber optic cables are capable of transmitting light due to the phenomenon of total internal reflection. Total internal reflection is a consequence of Snell's Law which relates the refraction angles to the indices of refraction of the materials at the interface:

$$n_1 \sin \theta_1 = n_2 \sin \theta_2$$

Equation 3-1

Where n_1 and n_2 are the indices of refraction, and θ_1 and θ_2 are the refraction angles relative to the surface normal. When incident from higher index of refraction to a lower index, for a sufficiently large incident angle (relative to the surface normal), the angle of refraction will reach 90° , the point known as the critical angle. At this point the ray will glance along the surface of the boundary. At larger incidence angles all the light will be

internally reflected. The process is termed “total internal reflection”, and is shown schematically in Figure 3-1.

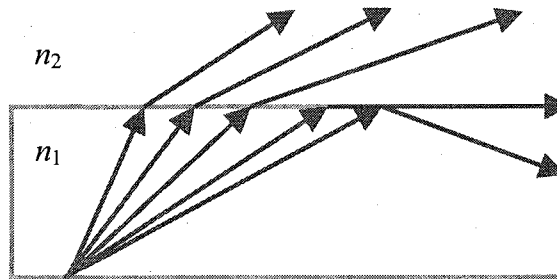


Figure 3-1
Rays of light exiting the material are totally internally reflected at the critical angle (n_1 is greater than n_2).

A conventional fiber optic cable takes advantage of the critical angle to allow transmission of light with little loss. The most common solid core fiber optic is comprised of a step-index core: a light transmitting core surrounded by a cladding with an index of refraction lower than that of the core, as seen in Figure 3-2. Typical silica fibers might have an index of refraction of 1.62 and the cladding an index of 1.52 [1] and use a fluorine or rare earth element as a doping material [2].

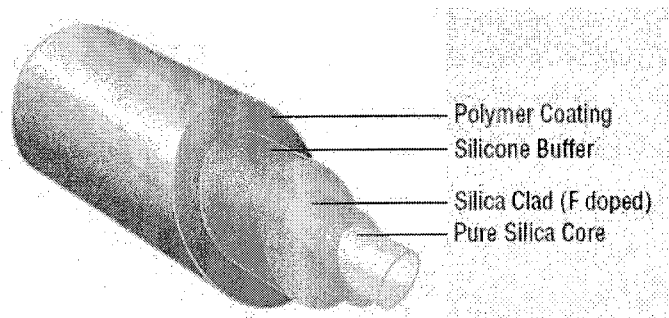


Figure 3-2
Diagram showing light entering a fiber optic cable [2].

The ratio between the index of the core and the index of the cladding defines a critical angle which represents the maximum angle (relative to the fiber axis) at which an incoming ray will be efficiently transmitted instead of absorbed into the jacket of the fiber. The maximum angle that can be transmitted is found using geometry and Snell's Law, yielding:

$$\sin \theta_{\max} = \frac{1}{n_i} (n_f^2 - n_c^2)^{1/2}$$

Equation 3-2

where n_f , n_c , and n_i are the indices of the fiber core, cladding, and surrounding medium respectively. The quantity $n_i \sin \theta_{\max}$ is defined as the numerical aperture (NA) of the fiber. Thus the above equation may be re-written in terms of NA as:

$$NA = (n_f^2 - n_c^2)^{1/2}$$

Equation 3-3

The numerical aperture defines the maximum angle (relative to the fiber axis) at which a ray of light can be launched into a fiber and effectively guided. More importantly, for the purposes of this work, it defines the maximum angle (divergence) at which light exits the fiber.

For relatively long fibers (> 10 m), and for fibers with a large number of bends, light exits the fiber in approximately a cone shape with the cone half-angle equal to the fiber numerical aperture, regardless of how the light is coupled at the fiber input (launch). For single-mode fibers (defined below), the light is transmitted and exits as the lowest order mode. In multi-mode fibers (defined below) the light exits in this manner because

light rays which are near parallel to fiber axis (low order modes) will gradually be converted into higher order modes. This concept is shown schematically in Figure 3-3.

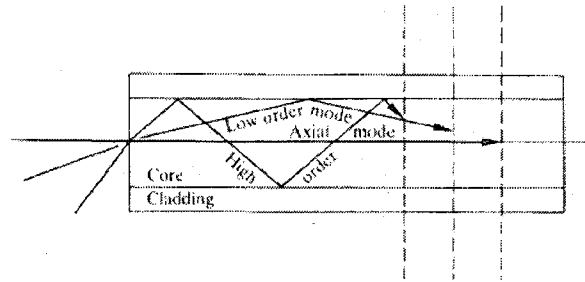


Figure 3-3
Mode propagation in a multi-mode fiber optic [1].

Fibers with relatively large core diameters ($> \sim 10 \mu\text{m}$) are termed “multi-mode” because they allow dispersion of the input light beam and propagate multiple spatial modes. Small diameter fibers ($< \sim 10 \mu\text{m}$) do not allow this modal dispersion and are referred to as “single mode” fibers [3]. As will be further discussed in Section 3.2, the presence of high order (divergent) modes make it difficult to focus the light exiting the fiber to small diameters (needed to achieve high intensity at the focal region and breakdown).

The initial beam produced by a laser will have a certain spatial profile (quality) determined by details of the optical cavity including the resonator mirrors curvatures and positions. The highest quality beam is defined by a pure Gaussian solution to the propagation equation of a particular resonant cavity with a waist w_0 located at an axial position z_0 for such a beam, the spot size $w(z)$ of this Gaussian at any position outside or inside the resonator can be determined by the Gaussian spot size formula [4]:

$$w^2(z) = w_0^2 \times \left[1 + \left(\frac{z - z_0}{z_r} \right)^2 \right]$$

Equation 3-4

where $z_r \equiv \pi w_0^2 / \lambda$ is referred to as the Rayleigh range of the Gaussian mode. However, in a true laser beam, other solutions (modes) to the propagation equation (besides the Gaussian) will generally exist. These modes can be expressed as Hermite-Gaussian (rectangular) solutions to the propagation equation. Transverse intensity profiles of these solutions are shown in Figure 3-4.

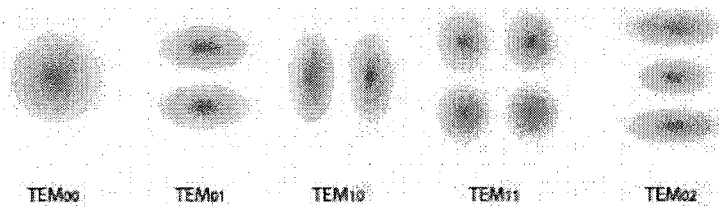


Figure 3-4
Examples of low-order Hermite-gaussian modes [5].

These transverse intensity profiles of eigenmodes are given the notation TEM_{nm} where subscripts n and m correspond to the number of nodes in the x and y directions and TEM is an acronym for “Transverse Electro-Magnetic”. The pure Gaussian mode described above corresponds to the TEM_{00} solution. Alternatively, the propagation equation can be written in cylindrical form in terms of radius and angle yielding axisymmetric modes described by Laguerre-Gaussian functions as shown in Figure 3-5.

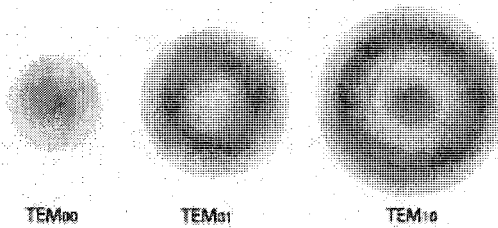


Figure 3-5
Examples of low-order axisymmetric modes [5].

The transverse intensity profile of a beam exiting a multi-mode fiber will be a superposition of modes as determined by the input beam and mode characteristics of the fiber system. Thus a difficulty is created in determining the beam width (at the waist or any other point) of such a beam. For example, simple application of Equation 3-4 is insufficient, and beam sizes often need experimental measurement. Many definitions of beam width have been used including half- or full- width at half-maximum intensity, width at $1/e$ or $1/e^2$ intensity points, width of a rectangular profile having the same peak intensity and same total power, width of a Gaussian fitted to a measured profile, etc [6]. To reduce the discrepancies caused by the use of these various methods an ISO standard (11146) has been developed utilizing the M^2 method. The M^2 method is based on the variances, σ_x and σ_y , of the transverse intensity profile. The formulation evaluates the second moment of the beam intensity profile $I(x,y)$ at a given Z plane :

$$\sigma_x^2 = \frac{\int_{-\infty}^{\infty} (x - x_0)^2 I(x, y) dx dy}{\int_{-\infty}^{\infty} I(x, y) dx dy}$$

$$\sigma_y^2 = \frac{\int_{-\infty}^{\infty} (y - y_0)^2 I(x, y) dx dy}{\int_{-\infty}^{\infty} I(x, y) dx dy}$$

Equation 3-5

where (x_0, y_0) is the center of gravity of the beam. It is convenient to use the definitions that $W_x(z) \equiv 2\sigma_x(z)$ and $W_y(z) \equiv 2\sigma_y(z)$ where $W_x(z)$ and $W_y(z)$ are the real-beam analogs of the Gaussian spot sizes $w_x(z)$ and $w_y(z)$ for an ideal Gaussian beam. The quadratic variations of these real-beam spot sizes squared with distance z can then be written for an arbitrary beam profile in the form [7]:

$$\begin{aligned} W_x^2(z) &= W_{0x}^2 + \left(\frac{M_x^2 \lambda}{\pi W_{0x}} \right)^2 (z - z_0)^2 \\ &= W_{0x}^2 \times \left[1 + \left(\frac{(z - z_{0x})}{z_r} \right)^2 \right] \end{aligned}$$

and

$$\begin{aligned} W_y^2(z) &= W_{0y}^2 + \left(\frac{M_y^2 \lambda}{\pi W_{0y}} \right)^2 (z - z_0)^2 \\ &= W_{0y}^2 \times \left[1 + \left(\frac{(z - z_{0y})}{z_r} \right)^2 \right] \end{aligned}$$

Equation 3-6

where W_{0x} and W_{0y} are the Rayleigh ranges for the real-beam case in the x and y directions, and are given by $z_{r(x,y)} \equiv \pi w_{0(x,y)}^2 / M_{(x,y)}^2 \lambda$. The M^2 factor describes the ratio of actual beam waist to that of the diffraction limited a beam waist. Note that Equation 3-6 reduces to the Gaussian spot size formula given in Equation 3-4 with the M^2 value set to 1 (as it would be in a TEM₀₀ beam). Thus the divergence of a real beam can be calculated from its the M^2 parameter and waist:

$$\theta = M^2 \frac{\lambda}{\pi W_0}$$

Equation 3-7

Conversely, by measuring the divergence of a real beam by plotting beam diameters through the waist, the M^2 parameter may be determined experimentally (essentially the protocol defined by ISO 11146).

While the quality of the initial beam exiting the laser is determined by the laser resonator, the final M^2 of the beam will be affected by the optical system the beam passes through. Optical fibers generally cause an increase in M^2 through the previously described modal dispersion and thus contribute to making focusing difficult. For single-mode fibers this degradation is minimal; however, such fibers cannot transmit a large amount of power and are not generally useful for laser ignition.

3.1.2 Intensity Damage Threshold

The second challenge of fiber optic delivery relates to material properties of fiber material (typically silica) which has a damage threshold of 10-20 J/cm² for nanosecond pulses [8], thereby limiting the amount of power that can be transmitted through the fiber. The mechanism by which optical materials are damaged varies with laser wavelength, power density, pulse duration, surface quality, and imperfections in the material [9]. Generally an electron avalanche ionization process is thought to cause the damage, however non-linear processes including multi-photon ionization and self-focusing also play a role [10,11]. Self-focusing refers to the change in index of refraction of the medium at high power, causing lensing effects. The damage threshold for an unpolished cleaved fiber surface is generally 2-5 times lower than the damage threshold of the bulk material, which may be due to electrostatic forces at the interface caused by surface imperfections created during the cleaving process [12]. The effects of these imperfections can be mitigated through surface polishing. Surfaces prepared using an Al₂O₃ polish show damage thresholds at 50% - 100% of the bulk damage threshold. Silica treated with an Al₂O₃ polish followed by a SiO₂ polish consistently reached bulk damage thresholds [11].

Several bulk damage mechanisms related to refocusing have been postulated for multi-mode fibers. One such mechanism occurs at the first reflection of a misaligned beam. A simplified ray trace and cross sectional intensity profile of this scenario is shown in Figure 3-6 [9]. At the reflection point, the intensity reaches a peak that can be greater than the intensity at the launch.

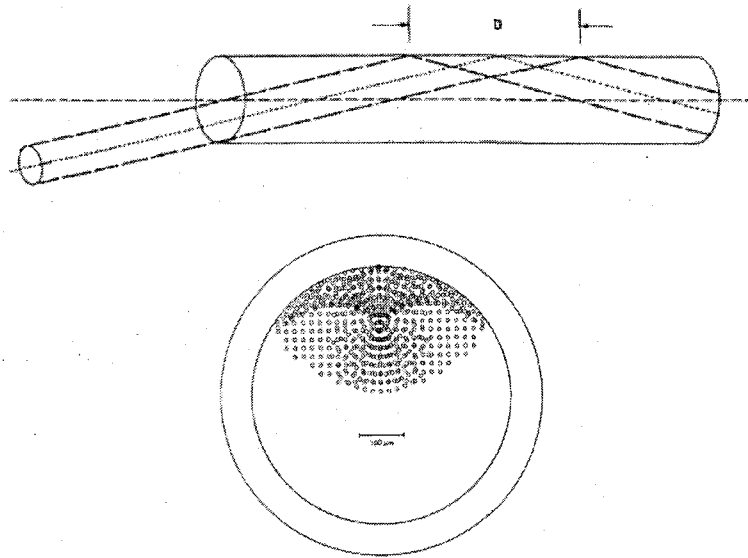


Figure 3-6
Unintentional focusing of a misaligned beam [8].

Another way in which self focusing can occur is shown in Figure 3-7. In the work of Richou et al. the beam launch was contained in a vacuum such that a plasma cannot form at the launch, allowing the maximum achievable power to be delivered to the fiber. However, as meridional rays reflected inside the fiber, they could potentially refocus some distance into the fiber. This damage mechanism is of particular interest because it was found experimentally while using laser wavelengths, pulse durations, and energy similar to those of this work [12].

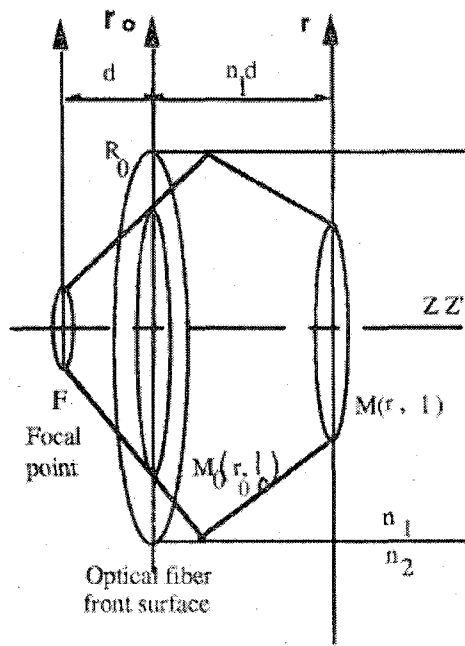


Figure 3-7
Meridional ray reflection leading to optical damage [12].

3.2 Figure of Merit Development for Fiber Selection

Given the interrelated challenges of fiber delivery and focusing intense light pulses, a “Figure of Merit” was developed for fiber assessment and comparison. Based on the exit parameters of a laser beam from a fiber, the Figure of Merit allows an approximate evaluation of maximum achievable intensities [13].

Consider light exiting a fiber shown in Figure 3-8. The exit light is focused by a lens, creating a spark at the focal point (for simplicity we use a single lens, though multiple lenses could be similarly treated). I_{exit} represents the optical intensity at the exit of the fiber, while I_{spark} represents the optical intensity at the focused spot (desired spark location). Similarly, d_{exit} and d_{spark} represent the diameter at the fiber exit and spark location respectively, and θ_{exit} and θ_{spark} represent the angles (of the widest light rays) at the fiber exit and spark location.

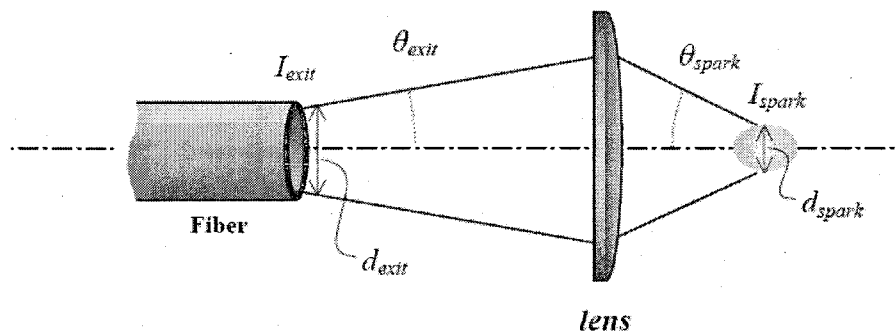


Figure 3-8

Schematic diagram of focusing light at exit of optical fiber.

The Figure of Merit can be derived from paraxial ray-tracing (geometric optics) or from M^2 considerations. Both analyses are equivalent under certain simplifying

assumptions. The first assumption is that the light at the fiber exit uniformly fills the fiber diameter. In such a case, ray tracing (Lagrange invariant) allows the following expression for demagnification (*Demag*):

$$Demag \equiv \frac{d_{exit}}{d_{spark}} = \frac{\theta_{spark}}{\theta_{exit}}$$

Equation 3-8

The demagnification is defined as the ratio of object size to image size, where the fiber face is the object and the spark location is the image. We desire the Figure of Merit to be proportional to the intensity at the spark location, but independent of the focusing optics. Therefore, we define it as the intensity at the spark location divided by the square of the final focusing angle at the spark location:

$$FOM_{Source} \equiv \frac{I_{spark}}{\theta_{spark}^2} = \frac{I_{exit} Demag^2}{\theta_{spark}^2} = \frac{I_{exit}}{\theta_{exit}^2}$$

Equation 3-9

For a relatively collimated beam exiting the fiber, θ_{spark} is about $\frac{1}{2}$ the inverse of the *f#* of the focusing lens. If one assumes that the light at exiting the fiber has a waist at the fiber exit (and equal to the fiber radius) and a far-field divergence angle equal to the fiber exit, then an analysis based on embedded Gaussian (M^2) concepts yields the same expression for the Figure or Merit [14,15]. This treatment is more appropriate for fiber delivered systems than the (often used) diffraction limited expression:

$$D_{focus} = \left(\frac{2}{\pi}\right)\lambda \left(\frac{f}{D}\right)$$

Equation 3-10

where D_{focus} is the diameter of the beam at the focal point, and D is the diameter of the beam incident on the lens. Equation 3-10 predicts smaller diameters (and hence larger intensities) than the FOM analysis. The discrepancy is because Equation 3-10 applies only for a collimated beam and for a diffraction-limited ($M^2=1$) beam – neither applies at the fiber exit and thus this formula is wholly inappropriate. The formula does apply for focusing of a high quality laser beam with no fiber, and thus shows why it is relatively easy to form sparks with such a beam. The Figure of Merit clearly shows that in order to achieve a high intensity at the intended spark location, one requires a high intensity at the fiber exit, I_{exit} , as well as a low divergence (θ_{exit}) at the fiber exit. The fact that the divergence angle is squared emphasizes its importance.

We now consider the minimum FOM_{min} required to achieve optical breakdown and form sparks. As discussed above, we conservatively assume that one requires an intensity at the spark location of approximately 2×10^{11} W/cm², and that (owing to aberrations) the best one can do for imaging is an effective value of $\theta_{exit}=0.17-0.25$ (which corresponds to $f\#=2-3$) then the required figure or merit is:

$$FOM_{min} \geq 3200 - 6900 \frac{GW}{cm^2 rad^2}$$

Equation 3-11

The required FOM scales linearly with the required I_{spark} (so uncertainty in required I_{spark} gives corresponding uncertainty in required FOM_{Source}). The FOM has been developed for atmospheric conditions, but as pressure increases the required spark intensity decreases, thus the FOM can be adjusted for use at different pressures.

3.3 FOM Evaluation of Fiber Candidates

There are many types of optical fibers that can be considered for delivery of high energy pulses required for laser ignition. In the following sections the relative metrics of the following fibers are compared based primarily on the Figure of Merit: solid core fibers, rigid hollow core fibers, flexible hollow core fibers, fiber lasers, and photonic crystal fibers. As a means to prioritize the appropriateness of each of these fiber types for our application, an estimated Figure of Merit for each fiber type is calculated according to the methodology previously described.

Source	I_{exit} (GW/cm ²)	θ_{exit} (Rad)	FOM_{Source} (GW/cm ² /rad)
Solid Fiber (base NA)	~3	~0.11	~250
Solid Fiber (lower NA)	~3	~0.03	~3300
Coated Hollow Fiber	~2	~0.015	~8900

Table 3-1
Calculated Figure of Merit for various fibers.

3.3.1 Solid Core Fibers

Solid core step-index fibers, as described in Section 3.1.1, are the most common type of fiber optic and are used extensively in industry for communication, remote

sensing/illumination, pressure sensing, tissue ablation, UV curing, ophthalmology, etc. [16]. Typical solid core fibers have a numerical aperture of 0.22, though lower NA's are achievable for short distances. This relatively large NA leads to a concurrently large exit divergence, and when combined with a damage threshold of $\sim 1\text{-}3 \text{ GW/cm}^2$ [17,18,19,20], results in a FOM of $250\text{-}3300 \text{ GW/cm}^2\text{rad}^2$, indicating that it is difficult to achieve spark formation with such fibers. To date no published reports of spark formation at atmospheric conditions have been reported; however, as described below, it is possible to use solid core fibers for spark formation at elevated pressures.

Rabii and Gaborel [21] have demonstrated spark formation at pressures of 6 bar using solid core silica fibers. Their demonstration utilized a step index silica fiber with a diameter of 940 microns and a length of 150 cm. This fiber was bent at 90° with a 50 cm radius of curvature. A 1064 nm, Q-Switched Nd:YAG laser was used to generate laser pulses. The maximum pulse energy transmitted by the fiber was 45 mJ which corresponds to fiber exit intensity of 0.9 GW/cm^2 . To achieve low fiber exit angles to allow for high intensity at the spark location, the fibers were operated below their base NA by employing a low launch angle; a fiber output NA of 0.034 was achieved, whereas the fiber has base NA of 0.22. Relatively strong focusing optics consisting of a 75 mm focal length collimating lens followed by an 8 mm focal length aspheric lens were used to achieve an intensity of approximately 60 GW/cm^2 at the focal spot. While this intensity is insufficient for consistent spark formation at atmospheric pressure, at a pressure of 6 bars, sparking was achieved 90% of time. Though the beam quality of the laser was high, the launch NA low, and the fiber length short, the beam exiting the fiber was very multimode. An estimation for the tests described above yields an M^2 of approximately

47 if assume a beam waist equal to half the fiber diameter (470 microns) and angle of 0.034 rad. In a modern industrial natural gas engine, the in-cylinder pressure before spark is on the order of 20-30 bar, potentially allowing the use of solid core fibers, though to be an improvement over current systems sparking must occur > 99.5% of the time.

3.3.2 Hollow Core Fibers

Hollow core fibers have been primarily developed for delivery of light from CO₂ lasers (10.6 microns) and can be either rigid or flexible. They were originally developed for medical and industrial applications of CO₂ lasers, but have recently been used to transmit incoherent light for broadband spectroscopic and radiometric applications [21,22,23]. The first hollow core waveguides were rigid and similar to microwave guides: Garmire et al. made a simple rectangular waveguide for a CO₂ laser using polished aluminum strips placed 0.5 mm apart [24]. Today, hollow core fibers are more commonly made from plastic or glass tubing, allowing them to be bent in multiple directions.

Hollow core fibers are attractive because their air core results in higher damage thresholds, low insertion losses, an absence of end reflections, and relatively small beam divergence. However, hollow core fibers typically have higher bending losses than solid core silica fibers. These losses generally vary as $1/R$ where R is the bend radius. In addition, transmission losses will scale as $1/a^3$ where a is the diameter of the fiber [25].

For the application of laser ignition, optical frequencies closer to the visible range are of more interest than the IR light of CO₂ lasers. For example, commercially available diode-pumped Nd:YAG lasers (1064nm) represent a possible practical laser ignition

source. The Q-switched output of such lasers provides short, intense optical pulses. The desired wavelength eliminates many of hollow core fibers from being practical to this application; however, a few research groups have developed hollow core fibers that are optimized for Nd:YAG frequencies.

Using glass, quartz, plastic metallic and plastic tubing as substrates for a hollow core fiber, Miyagi and Matsuura in Japan have utilized sputtering methods to deposit silver and polymer layers into sections of tubing resulting in low-loss fibers appropriate for Nd:YAG frequencies [25]. In addition, Croitoru and his group at Tel Aviv University applied Ag followed by AgI coating on the inside of Teflon tubing to manufacture a flexible waveguide [26]. The fibers developed by Matsuura are explored in greater detail in Chapter 5. Using low NA launches, these fibers have exhibited a FOM of $\sim 8,900$ GW/cm²rad².

3.3.3 Photonic Crystal Fibers

Photonic Crystal Fibers (PCFs) are a rapidly emerging area of optical fiber technology. PCF's are based on the properties of photonic crystals, in which periodic nanostructures in the silica fiber modify the refractive index and provide efficient light-guides. A sub-category of PCFs include Photonic Bandgap Fibers (PBFs) which confine light using band gap effects. The optical effect produced by PBF's and PCF's allows for a larger diameter fiber to exhibit the properties of a single mode fiber, allowing a high quality beam to be transmitted with little loss, which enables that beam to be focused to a small intense spot post fiber.

Currently several research efforts are underway to demonstrate the delivery of high power pulses through PCF's. A PBG fiber based on a PCF fiber with a 19 cell

defect in the center was used to transmit ~ 0.5 mJ Nd:YAG pulses with a duration of 65 ns through a 2-m length fiber [27]. Michaille et al. examined the transmission of high power pulses through both PBG and PCF fibers [28]. Using a PBG fiber with a core of 8- μm , the damage threshold was 4 times larger than that of an equivalent solid-core silica PCF.

Tests conducted at Colorado State University [29] using 2 m Large Mode Area fibers with core diameter of 25 μm showed that fiber transmission decreased with increasing input energy. Peak output energy of 0.55 mJ was achieved with a transmission efficiency of $\sim 45\%$.

Other researchers [30] have conducted ignition experiments with PBG fibers, using pulse energies of 0.15 mJ transmitted through a hollow core PBG fiber to show the possibility of ignition of methane-air mixtures, though these experiments were conducted under conditions (pressure, air/fuel ratio) that were extremely favorable for ignition, and therefore not of direct practical use in actual reciprocating engines.

3.3.4 Fiber Laser

Fiber lasers are a promising technology that has seen major advances in recent years. A fiber laser combines the laser source with the fiber delivery medium. This is achieved by doping the fiber core with a laser gain material and using the (first) cladding of the (double-clad) fiber to pump light into that gain medium. Often a seed laser external to the fiber will be injected into one end of the fiber. On the opposite end of the fiber single or multiple laser sources (not necessarily at the same frequency) are spliced into the cladding, providing the pump light, effectively amplifying the original seed laser.

Fiber lasers show a technology trajectory that could make them suitable candidates for laser ignition. A collaboration between Colorado State University and the University of Michigan recently demonstrated for the first time the creation of a post fiber spark at atmospheric conditions using a fiber laser [29]. This technology is currently under investigation and is beyond the scope of this thesis.

-
- ¹ Hecht. (1998). *Optics*. Addison Wesley Publishing, Reading Massachusetts.
- ² Web site. (n.d.). www.fiberguide.com
- ³ Goff. (1996). *Fiber Optic Reference Guide*. Focal Press.
- ⁴ Siegman. (1993). "Output Beam Propagation and Beam Quality from a Multimode Stable-Cavity Laser". *IEEE Journal of Quantum Electronics*. 29(4).
- ⁵ Web site. (n.d.). www.mellesgriot.com
- ⁶ Siegman. (1997). "How to (Maybe) Measure Laser Beam Quality". *Optical Society of American Annual Meeting*. Long Beach, CA.
- ⁷ Siegman. (1990). "New Developments in Laser Resonators", *Proceedings SPIE, Optical Resonators*. 1224, 2-14.
- ⁸ Kuzuu, Yoshida. (1999). "Laser-Induced bulk damage in various types of vitreous silica at 1064, 532, 355, and 266 nm: evidence of different damage mechanisms between 266-nm and longer wavelengths". *Applied Optics*. 38(12).
- ⁹ Allison, Gillies. (1985). "Pulsed laser damage to optical fibers". *Applied Optics*. 24(19).
- ¹⁰ Bennett, Glass. (1981). "Laser Induced Damage in Optical Materials," *Applied Optics*. 20, 3003.
- ¹¹ Smith, Do, Schuster, Collier. (1999). "Rate equation model of bulk optical damage of silica, and the influence of polishing on surface optical damage of silica". *Proceedings SPIE*. 6873(29).
- ¹² Richou, Schertz. (1997). "Delivery of 10-MW Nd:YAG laser pulses by large-core optical fibers: dependence of the laser-intensity profile on beam propagation". *Applied Optics*, 36(7).
- ¹³ Azer paper that talks about FOM
- ¹⁴ Yalin, DeFoort, Willson, Matsuura, Miyagi. (2005). "Use of Hollow Core Fibers to Deliver Nano-second Nd:YAG Laser Pulses for Spark Formation". *Optics Letters*. 30, 2083
- ¹⁵ Yalin, Reynolds, Joshi, DeFoort, Willson, Matsuura, Miyagi. (2006). "Development of a Fiber Delivered Laser Ignition System for Natural Gas Engines". *ASME ICED 2006 Spring Technical Conference*. ICES2006-1370.
- ¹⁶ Web site: (n.d.). www.fiberguide.com
- ¹⁷ Sturm, Sattmann, Noll. (1996). "Optical fiber transmission of multiple-switch Nd:YAG laser pulses with microsecond interpulse separations". *Applied Physics B*. 63, 363-370.
- ¹⁸ Allison, Gillies, Magnuson, Pagano. (1985). "Pulsed laser damage to optical fibers". *Applied Optics*. 24, 3140-3145.
- ¹⁹ Stakhiv, Gilber, Kopecek, Zheltikov, Wintner. (2004). "Laser ignition of engines via optical fibers?". *Laser Physics*. 14, 738-747.
- ²⁰ El-Rabii, Gaborel. (2007). "Laser ignition of flammable mixtures via a solid core optical fiber". *Applied Physics B*. 87, 139-144.
- ²¹ Saggese, Harrington, Sigel. (1991). "Attenuation of incoherent infrared radiation in hollow sapphire and silica waveguides". *Optics Letters*. 16, 27-29.
- ²² Saito, Matsuura, Kawamura, Miyagi. (1990). "Bending losses of incoherent light in circular hollow waveguides". *Journal of the Optical Society of America A*. 7, 2063-2068.
- ²³ Saito, Kikuchi. (1997). "Infrared optical fiber sensors," *Optical Review*. 4, 527-538.
- ²⁴ Garmire, McMahon, Bass. (1980). "Flexible infrared waveguides for high-power transmission". *Journal of Quantum Electronics*. 16, 23-32.
- ²⁵ Matsuura, Takada, Yamamoto, Shi, Miyagi. (2002). "Hollow fibers for delivery of harmonic pulses of Q-switched Nd:YAG lasers". *Applied Optics*. 41(3).
- ²⁶ Morhaim, Mendlovic, Gannot, Dror, Croitoru, (1991). "Ray model for transmission of infrared radiation through multibent cylindrical waveguides". *Journal of Optical Engineering*. , 30, 1886-1891.
- ²⁷ Shephard, Couny, Russell, Jones. (2005). "Improved hollow-core photonic crystal fiber design for delivery of nanosecond pulses in laser micromachining applications". *Applied Optics*. 44, 4582-4588.
- ²⁸ Michaille, Taylor, Bennett, Shephard, Jacobsen, Hansen. (2004). "Damage threshold and bending properties of photonic crystal and photonic band-gap optical fibres". *Proceedings – SPIE*. 5618, 30-38.
- ²⁹ Joshi, Yalin, Galvanauskas. (2007). "On the Use of Hollow Core Fibers, Fiber Lasers, and Photonic Crystal Fibers for Spark Delivery and Laser Ignition in Gases". *Applied Optics*. 46(19).
- ³⁰ Al-Janabi. (2005). "Transportation of nanosecond laser pulses by hollow core photonic crystal fiber for laser ignition". *Laser Physics*. 2.

4 Chapter Four - Development of Focusing Optics

In Chapter 3, the difficulty of delivering high power optical pulses while maintaining beam quality was discussed, with the implication that low quality (high M^2) light is difficult to refocus. In this chapter we discuss the development of focusing optics to be used in conjunction with fiber optics to deliver optical sparks. Two approaches were taken in the development of the focusing optics. Several simple optical arrangements were explored in bench top experiments to indicate what beam waist and profile could be expected in practice. This information was then used to develop reasonable initial conditions which, through a partnership with Oak Ridge National Lab (ORNL), were used with the optical modeling program Zemax. ORNL used Zemax to perform a simple optimization routine to suggest a focusing optical train capable of focusing the light from the fiber exit to a sufficiently small spot such that breakdown (ignition) would occur.

The first lens configuration modeled in Zemax is shown in Figure 4-1. The configuration uses a pair of 9 mm diameter, 9 mm focal length lenses. This is the same configuration as used in "Plug C" detailed in Chapter 6. In this design, a 1 mm diameter solid core fiber was used to deliver the beam.

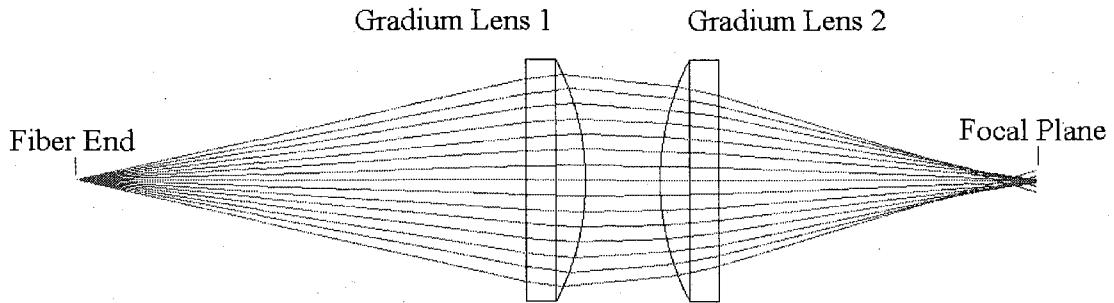


Figure 4-1
Modeled Optical Layout

From the literature previous cited, it can be concluded that the system must reach a peak optical intensity of approximately 10^{11} Watts/cm² to achieve breakdown. For the purposes of the model it was assumed that a 40 mJ, 8 ns pulse exited the 1 mm diameter fiber face in a uniform manner, resulting in intensity at the fiber exit of about 6×10^8 Watts/cm². The results of the Zemax model are shown in Figure 4-2 and Figure 4-3.

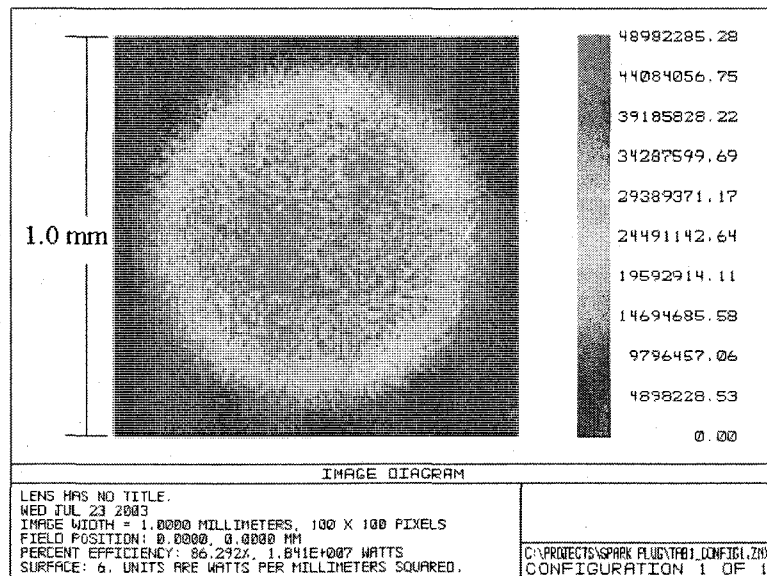


Figure 4-2
Zemax intensity plot of the focal spot (W/mm²).

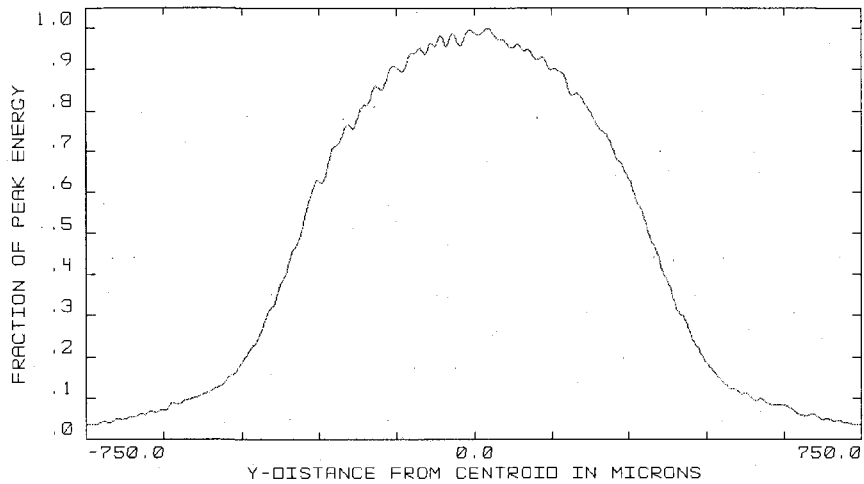


Figure 4-3
Focal Spot Intensity Profile.

The model concludes that with an average fiber output intensity of around 10^9 W/cm², this design (also Plug C) is unlikely to result in breakdown. Also note that the peak intensity at the focal point is not much greater than the average intensity. Thus the model suggests that the focal point can be characterized as being more of a de-magnified image of the fiber face rather than a true Gaussian focal spot. Table 4-1 outlines quantitative results from the simulation. The “efficiency” is a measure of how efficient the system is at focusing light into a 50 micron diameter area in the focal plane, and efficiency greater than 1 indicates that the light is focused to a spot smaller than 50 microns. This metric is used by ZEMAX to provide an indirect measurement of the peak central intensity of the focal spot. Two lens types were used in all of the Zemax models, “COTS” refers to “commercial off the shelf” or lenses which could be purchased by major optics suppliers. “Custom” refers to lenses which would need to be custom made.

Configuration Number	Lens Types	Efficiency (%)	Focal Spot Diameter (μm) - FWHM	Focal Spot Diameter (μm) - 50% Encircled Energy	Peak Focused Energy (W/cm^2) at Focal Center
<i>Double Lens System with Gradium Lens (Plug C)</i>					
1	COTS*	0.343	670	631	3.7×10^9

Table 4-1
Analysis of Plug C. *Commercial-of-the-shelf (COTS)

Zemax was also used to evaluate several different optical designs using conventional lenses to determine if an improvement in the peak focused energy could be obtained. Designs were constrained as follows:

- Fiber Diameter = 1 mm
- Fiber NA = .22
- Wavelength = 1064 nm
- Pulse Energy Emitted from Fiber: 40 mJ @ 8 ns, distributed uniformly over fiber face.
- Maximum system length = 1000 mm
- Focal spot must be between 9 mm and 23 mm from last lens surface

These constraints were determined by the geometry of the engine, the capabilities of the Big Sky laser system (an Nd:YAG laser with a small, robust housing selected for on-engine testing), and expected fiber output conditions. Two lens diameters of 12.5 mm and 75 mm were evaluated. The smaller diameter lens represents the maximum diameter feasible for engine use without modifying the cylinder head of the engine. The larger diameter was included in the event that the small diameter would be overly constrained.

If the larger diameter model showed good results, modifications could be made to the engine to accept a larger diameter spark plug. The results are shown in Table 4-2 and Table 4-3.

Configuration Number	Lens Types	Efficiency (%)	Focal Spot Diameter (μm) - FWHM	Focal Spot Diameter (μm) - 50% Encircled Energy	Peak Focused Energy (W/cm^2) at Focal Center
Single Lens Design					
1	COTS	0.386	434	662	4.2E9
2	Custom	0.646	431	540	7.0E9
Double Lens Design					
3	COTS	0.654	500	500	7.1E9
4	Custom	0.915	428	402	1.0E10
Triple Lens Design					
5	COTS	0.653	447	489	7.1E9
6	Custom	0.994	103	105	1.1E10

Table 4-2
Optimized designs for 12.5mm maximum diameter lenses.

Configuration Number	Lens Types	Efficiency (%)	Focal Spot Diameter (μm) - FWHM	Focal Spot Diameter (μm) - 50% Encircled Energy	Peak Focused Energy (W/cm^2) at Focal Center
Single Lens Design					
1	COTS	0.307	208	788	3.3E9
2	Custom	0.828	233	331	9.0E9
Double Lens Design					
3	COTS	0.652	488	485	7.1E9
4	Custom	0.924	292	578	1.0E10
Triple Lens Design					
5	COTS	.650	489	492	7.1E9
6	Custom	No Convergence	No Convergence	No Convergence	No Convergence

Table 4-3
Optimized designs for 75 mm maximum diameter lenses.

The Zemax output indicated that none of the optimized designs would achieve the target intensity of 10^{11} Watts/cm². The model was also exercised for a smaller fiber diameter to examine the effect on maximum achievable intensities. It was assumed that the smaller fiber diameter (0.5 mm) would be achieved through either a 0.5 mm traditional fiber or a tapered fiber. A negatively-tapered fiber will theoretically have a larger NA than a constant area fiber with the same exit diameter. However, larger exit intensities can be achieved with a negatively-tapered fiber vs. a constant area fiber with the same exit diameter. This is because a negatively-tapered fiber will have a larger diameter at the fiber launch (a limiting factor in the case of the straight fiber). Tapered fibers are described in greater detail in section 5.1. The model yielded the results shown in **Table 4-4**.

Configuration Number	Lens Types	Efficiency (%)**	Focal Spot Diameter (μm) - FWHM	Focal Spot Diameter (μm) - 50% Encircled Energy	Peak Focused Energy (W/cm ²) at Focal Center
<i>Double Lens System with Gradium Lens</i>					
1	COTS	1.035	364	384	1.1×10^{10}

Table 4-4
Analysis of Plug C with a fiber diameter of 0.5 mm.

Configuration Number	Lens Types	Efficiency (%)	Focal Spot Diameter (μm) - FWHM	Focal Spot Diameter (μm) - 50% Encircled Energy	Peak Focused Energy (W/cm^2) at Focal Center
Single Lens Design					
1	COTS	0.507	358	545	5.5×10^9
2	Custom	0.988	313	438	1.1×10^{10}
Double Lens Design					
3	COTS	1.077	355	390	1.2×10^{10}
4	Custom	1.859	281	267	2.0×10^{10}
Triple Lens Design					
5	COTS	0.846	357	380	9.2×10^9
6	Custom	2.297	63	75	2.5×10^{10}

Table 4-5
Optimized designs for 12.5mm maximum diameter lenses using a fiber diameter of 0.5 mm.

Configuration Number	Lens Types	Efficiency (%)	Focal Spot Diameter (μm) - FWHM	Focal Spot Diameter (μm) - 50% Encircled Energy	Peak Focused Energy (W/cm^2) at Focal Center
Single Lens Design					
1	COTS	0.452	165	780	4.9×10^9
2	Custom	1.338	158	274	1.5×10^{10}
Double Lens Design					
3	COTS	0.988	405	415	1.1×10^{10}
4	Custom	1.586	214	552	1.7×10^{10}
Triple Lens Design					
5	COTS	0.985	406	421	1.1×10^{10}
6	Custom	No Convergence	No Convergence	No Convergence	No Convergence

Table 4-6
Optimized designs for 75 mm maximum diameter lenses using a fiber diameter of 0.5 mm.

The modeling results for the smaller diameter fiber modeling were encouraging. Due to the pressure dependence of laser ignition previously discussed, the intensity threshold at high pressures drops slightly, such that these designs may be acceptable for initiating breakdown in an engine environment. It was decided that the tapered fiber

should be explored in greater detail. The results of this exploration are presented in section 5.1.

From the Zemax designs, the most attractive COTS design was selected, and designated "Design D". (The Zemax design that was selected is found in Table 4-2, configuration number 3. A 2D ray-trace diagram of the design is shown in Figure 4-4.) This design was used to compare the results of the Zemax model with actual beam profile data. If intensities of approximately the 10^{11} Watts/cm² goal seemed achievable, the design would be tested on the engine.

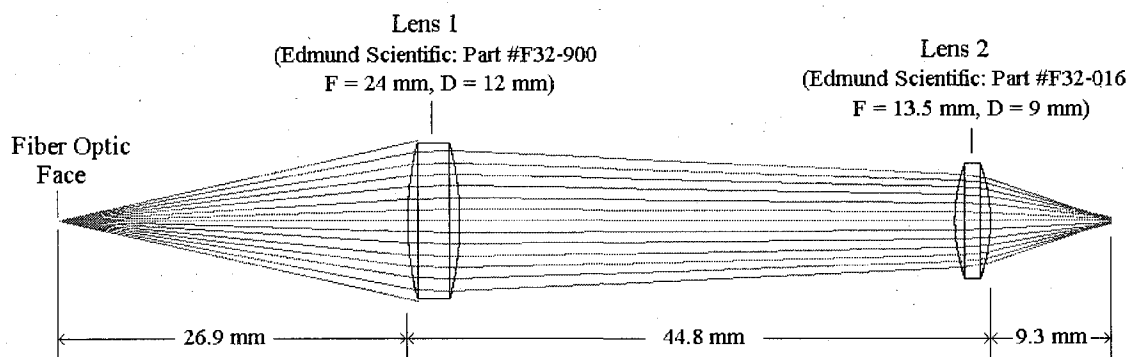


Figure 4-4
Optical layout of "Design D"

A profiling experiment was conducted to directly measure the beam profile exiting Design D. The actual beam profile would be used to compare to the modeled profile and provide insight into the reliability of the Zemax model. To this end, a Spiricon laser beam profiling system was used (Figure 4-5). The system consists of a charge coupled device (CCD) camera, frame grabber, and software that converts the beam images to quantitative spatial intensity maps. CCD cameras are sensitive devices so that a

combination of beam splitters and neutral density filters must be used to image high power lasers. In this instance, a combination of filters is used in conjunction with a HeNe laser.

There are several reasons for using the HeNe laser: it has a high quality collimated beam (thus the profiles represent best case scenarios), it is a continuous laser so manipulation of the camera is easier, and its intensities are lower so that it requires less attenuation when being profiled.

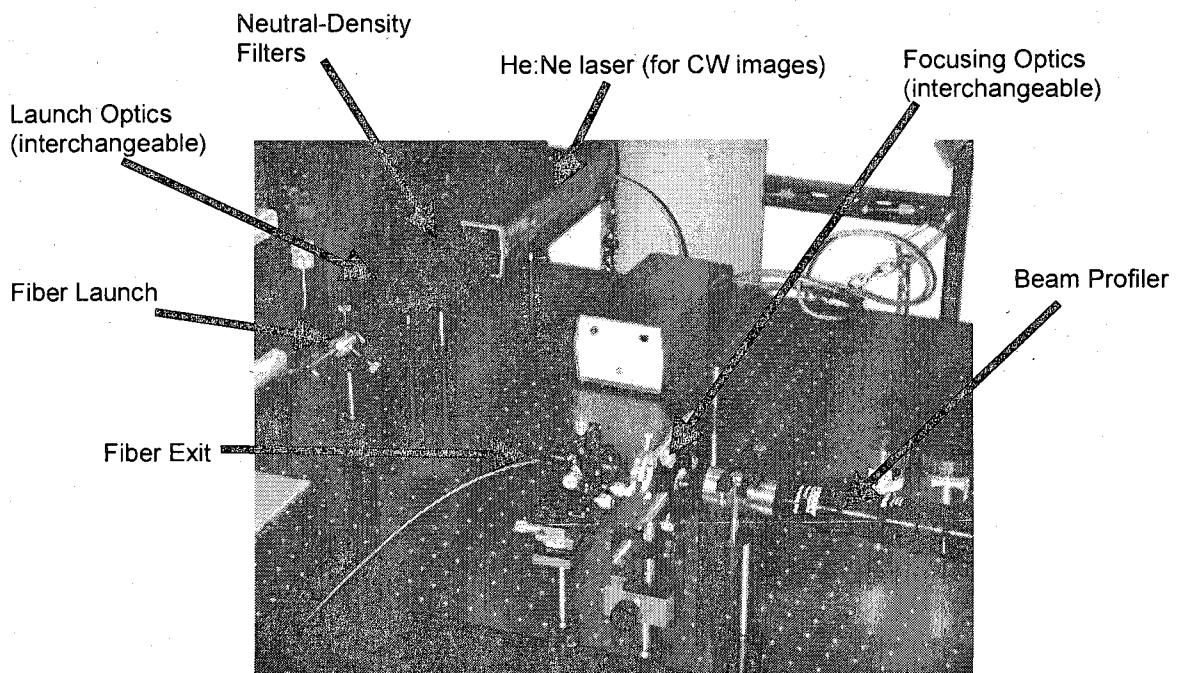


Figure 4-5
Profiling set-up used to characterize fiber delivery systems.

As shown in Figure 4-6, two alignment mirrors were used to direct the beam into the launch optics. The launch optics were originally internal to the Big Sky Nd:YAG laser. The CCD camera could then be translated back and forth along the fiber axis to generate a profile of the focal region.

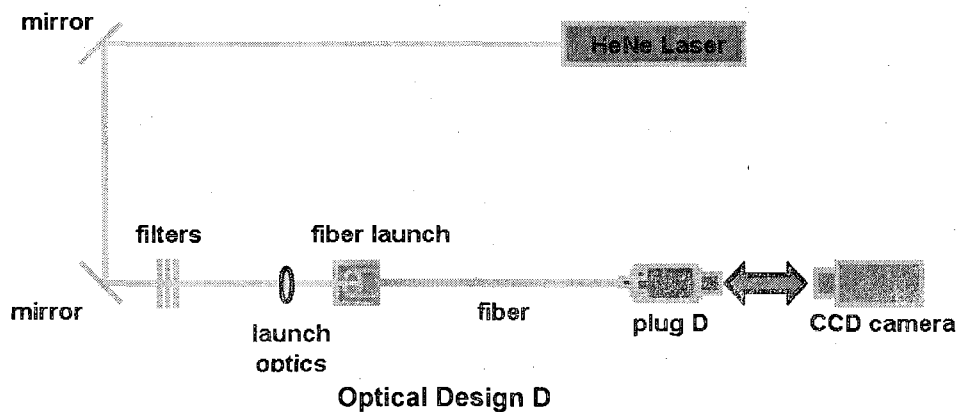


Figure 4-6
Optical train for beam profiling experiments.

The beam waist profile for Design D is shown in Figure 4-7. For the positions shown, measured beam waist diameters (from left to right) are 860 μm , 780 μm , 640 μm , 840 μm , and 1480 μm .

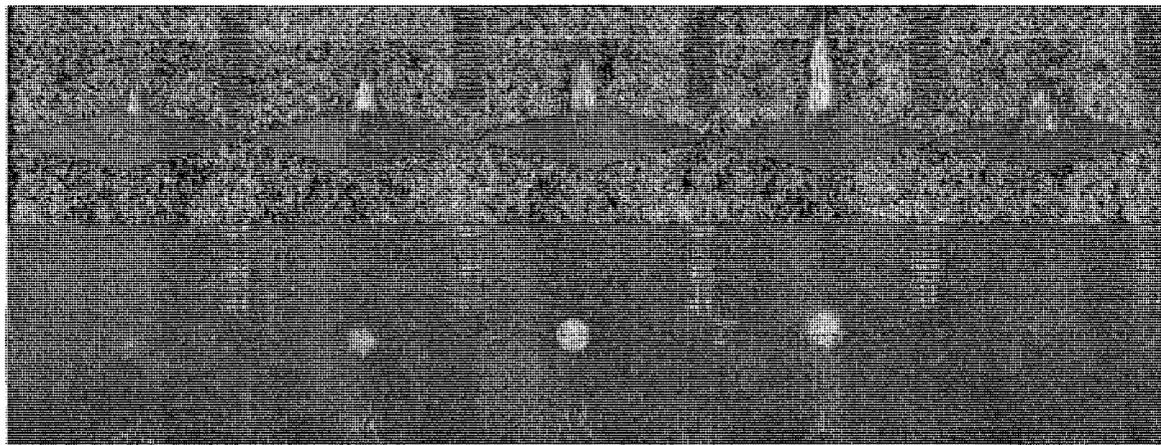


Figure 4-7
Beam waist profile slices exiting a straight fiber (beam travels left to right).

Therefore, the resulting beam diameter is slightly higher in practice than the model suggests (640 μm vs. 500 μm). Though further optimization appeared possible, it was decided to commence testing and characterization of various fiber optics using Design D as a baseline.

5 Chapter Five - Fiber Optic Testing and Characterization

A solid core silica fiber with a diameter of 1mm, in conjunction with the optical layout described as Design D, was used as the baseline case for the comparison of various fiber types. The results of this baseline experiment are described previously (Section 4). Two alternatives to solid core fibers were examined; tapered solid core fibers and hollow core fibers. As in the baseline condition, both high power and lower power testing was conducted. Low power CW lasers were used to obtain profiles of the beam, high power testing was used to evaluate transmission efficiency and the ability to create sparks.

5.1 Experimental Evaluation of Tapered Solid Core Fibers

Tapered fibers change in diameter from input to output. Some tapered fibers are a “continuous taper” where the diameter slowly changes throughout the length of the fiber. Other fibers use short end-cap sections which are tapered with a constant area fiber between them. Tapered fibers were explored to understand potential trade-offs between fiber diameter and numerical aperture. When used as a positive taper (input diameter > output diameter) the reduction in diameter along the beam tends to cause the numerical aperture to increase. The converse is true for a negative taper. This relationship is a geometrical one and is illustrated by simple ray tracing in Figure 5-1.

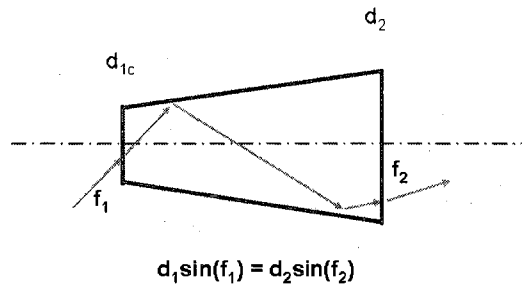


Figure 5-1
Numerical aperture conversion by a tapered fiber.

While geometrically it could be argued that any benefit in numerical aperture (or divergence) would be offset by a decrease in the totally energy delivered, it is difficult to make this determination. Therefore, beam profile measurements were taken to explore what effect a taper fiber might have on the focal spot diameter.

A collimated beam from a helium-neon (He-Ne) laser was used as an input beam to attempt to achieve a low input divergence angle (NA). Thus the measurement of the tapered fibers could be compared to those taken with a straight fiber. Two tapered fibers were employed, tapered fiber "A" had end diameters of 200 and 1000 micrometers and a length of 3 m. Tapered fiber "B" had end diameters of 250 and 1400 micrometers and a length of 1 m. Fiber "B" had discrete tapers, consisting of cone shaped sections at either end which were several cm in length, while the remainder of the fiber had a uniform diameter of 1000 μm . Conversely, fiber "A" was a continuous taper, starting with a 1000 μm fiber which is drawn and cleaved so as to achieve the appropriate output diameter. The tapered fibers were tested in both orientations (beam input at small diameter end and beam input at large diameter end). Divergence angles (θ_{exit}) were found by using a caliper to measure the beam size downstream of the fiber exit. By plotting the beam diameter versus downstream distance, a straight line could be fit to the data, the slope of which

yields the exit divergence angle (θ_{exit}). Results of the fiber divergence tests are provided in Table 5-1 below.

	θ_{exit}
Straight Fiber (1000 μm diameter, 1m length)	0.11
Taper Fiber "A" (200 μm diameter at output, 3m length)	0.29
Taper Fiber "A" (1000 μm diameter at output, 3m length)	0.02
Taper Fiber "B" (250 μm diameter at output, 1m length)	0.32
Taper Fiber "B" (1400 μm diameter at output, 1m length)	0.11

Table 5-1
Fiber divergence (exit angle) measurements

Table 5-1 shows that small fiber exit divergences can be achieved for tapered fibers when used as a negative taper (the large diameter is placed at the output end). It is found that the lowest exit divergence occurs in the continuous tapered fiber (or fiber "A") with its large diameter at the output end. Comparing tapered fibers "A" and "B", it is found that "A" (continuous taper) yields a lower exit divergence than "B" (discrete end tapers). It is also found that when the fibers are used as a positive taper the NA increases significantly. The divergence measurements show that tapered fibers can yield small divergences (which are desirable) when operated with the large diameter at the output. For the two fibers tested, it is also determined that the continuously tapered fiber is more effective at reducing the NA than the end cap taper when both are used as a negative taper.

To determine to what extent the reduction in NA would reduce the size of the beam waist at the focal point, a series of beam profile measurements were made using the

tapered fibers and Design D optical layout. For both tapered fibers, the beam waist was characterized by taking profiles at several locations, starting at the exit of the optical plug and continuing through the beam waist (i.e. minimum diameter of the focused beam), spanning a distance of approximately 30 mm (with care taken to seek the minimum beam waist) as shown in Figure 5-3 and Figure 5-4. The beam profile from the straight fiber is also included in Figure 5-2 for comparison. The beam enters from the left side of the page. A 3 dimensional representation of intensity is plotted in the upper photos while a cross sectional plot of intensity is plotted in the lower photos.

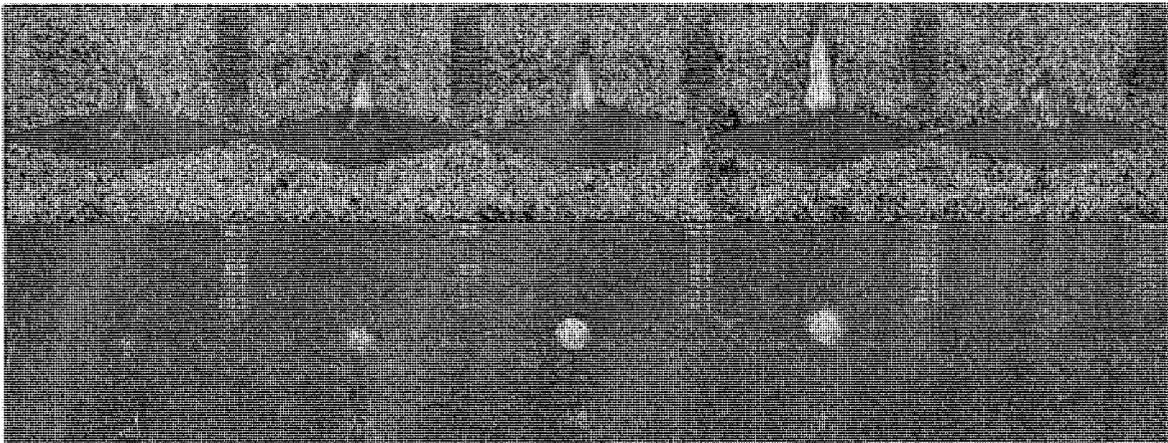


Figure 5-2

Beam waist profile slices for light after exiting the straight fiber (beam traveling from left to right). For the positions shown, measured beam waist diameters (from left to right, ~7mm spacing) are 860 μm , 780 μm , 640 μm , 840 μm , and 1480 μm .

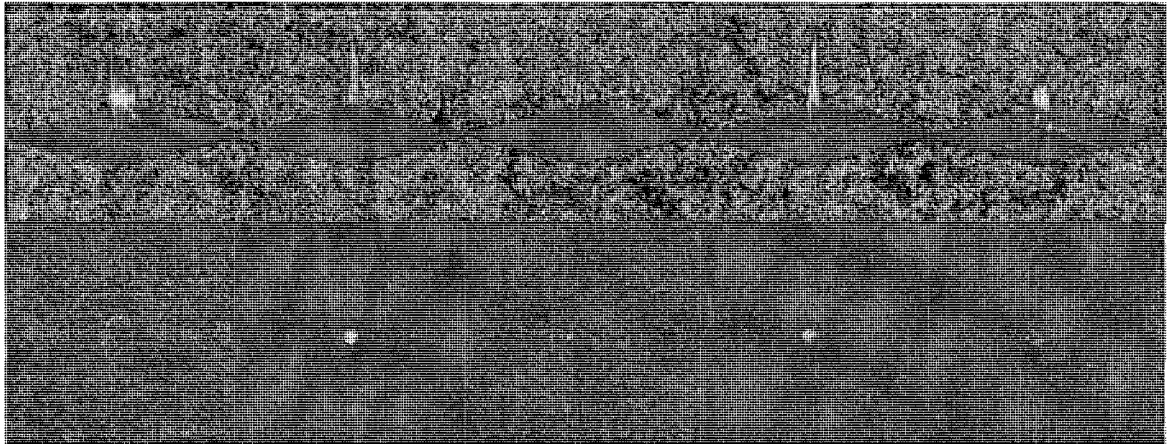


Figure 5-3

Beam waist profile slices for light after exiting tapered Fiber "A" (beam traveling from left to right). For the positions shown, measured beam waist diameters (from left to right, ~ 7 mm spacing) are $1050\mu\text{m}$, $340\mu\text{m}$, $130\mu\text{m}$, $370\mu\text{m}$, and $840\mu\text{m}$.

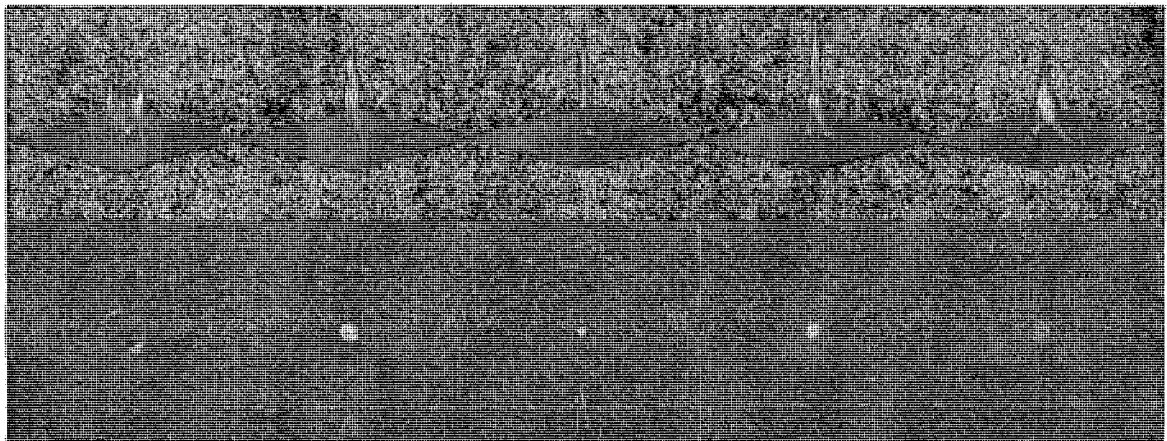


Figure 5-4

Beam waist profile slices for light after exiting tapered Fiber "B" (beam traveling from left to right). For the positions shown, measured beam waist diameters (from left to right, ~ 7 mm spacing) are $1064\mu\text{m}$, $430\mu\text{m}$, $205\mu\text{m}$, $330\mu\text{m}$, and $650\mu\text{m}$.

In each profile the middle image corresponds to the minimum beam waist (or the smallest diameter achieved). Thus, using identical focusing optics, laser sources, and fiber launches in each case, minimum waist diameters of $640\mu\text{m}$, $130\mu\text{m}$, and $205\mu\text{m}$ are

found for the straight fiber, tapered fiber “A”, and tapered fiber “B” respectively. Assuming constant damage intensity thresholds the maximum optical power that can be coupled into each fiber scales as its minimum diameter squared (since this is where the peak intensity would be located, and therefore where damage would occur). Thus, the maximum intensity at the spot size location is proportional to the squared ratio of the minimum fiber diameter to the waist (minimum spot size). For the three fibers, the ratios are: $2.4(=1000/640)^2$ for the straight fiber, $1.5(=200/130)^2$ for fiber “A” and $2.2(=250/205)^2$ for fiber “B”. Thus, in these experiments we do not see any advantage to operating with tapered fibers because the resulting focal spot intensities will be similar or slightly lower to those of straight fibers.

5.2 Experimental Evaluation of Rigid Hollow Core Fibers

Hollow core fibers have a hollow bore (no material) surrounded by a wall material. Such a configuration has a higher index in the wall than the core, in contrast to traditional fiber optic cables which have a lower index in the cladding than the core. Nonetheless, this difference in index of refraction allows the fiber to act as a waveguide albeit with relatively low transmission and high bending loss. Despite these drawbacks, rigid hollow core fibers have the potential to transmit high intensity beams because they possess an air core rather than a silica core. To explore the possibility of creating a spark after transmission through a hollow core fiber, a bench-top experiment was conducted. As shown in Figure 5-5, sparking was achieved in atmospheric pressure air with the focused output of the rigid hollow fiber.

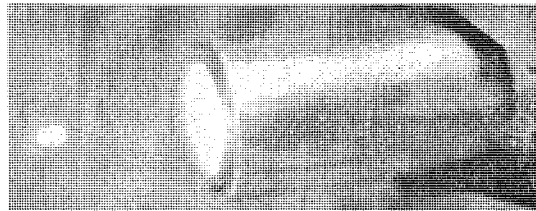
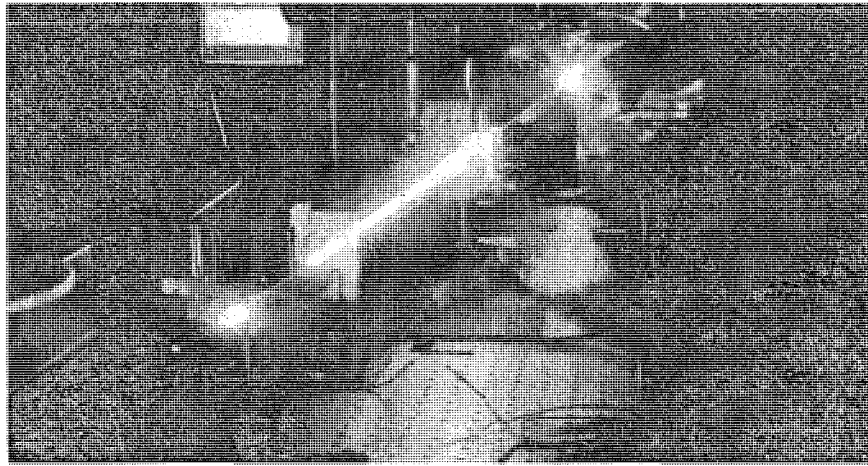


Figure 5-5
Bench-top experiment using a solid core wave-guide

Though the rigid hollow core fiber is obviously not practical for engine use, the experiment was useful in demonstrating that spark formation was possible using a hollow core fiber. In the next section, the next step is explored, the use of flexible hollow core fibers.

5.3 Experimental Evaluation of Coated Hollow Core Fibers

The FOM analysis of Chapter 4 suggested the utility of hollow core fibers. By applying certain coatings to the inner wall of hollow fibers, the efficiency of light guiding can be increased even in bent configurations. Applying these coatings to a glass capillary tube results in the creation of a flexible hollow core fiber. To test the ability of flexible

hollow core fibers to transmit high energy laser pulses for spark delivery, a partnership was formed with Yuji Matsuura, a professor in the Department of Electrical Communications at Tohoku University in Sendai Japan. Dr. Matsuura's group is one of the first to develop flexible hollow core fibers for industrial applications such as laser welding, and medical applications (dentistry, surgery) [2].

5.3.1 Fiber design and manufacturing

Flexible hollow core fibers (Figure 5-6) consist of a glass capillary tubing with a cyclic olefin polymer (COP)/silver coating on the interior surface. This construction results in a waveguide based on the same principles of traditional solid core fibers with the exception that these fibers have a lower index in the core rather than a higher index.

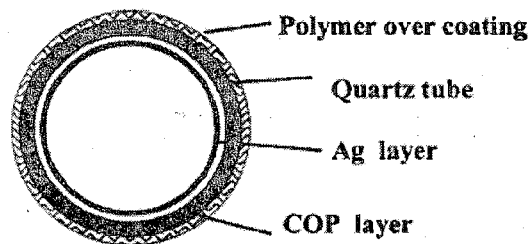


Figure 5-6
Schematic diagram of the hollow core fiber.

The polymer layer at the core/wall interface is tuned for various frequencies of transmission by varying the thickness of the layer. Matsuura¹ finds that the thickness of this layer is optimized according to Equation 5-1 where d is the thickness of the layer, n is the index of refraction of the layer, and n_0 is the index of refraction of air [2]. In addition, the polymer layer protects the reflective Ag layer from oxidation and damage.

$$d = \frac{\lambda}{2\pi n_0 \sqrt{n^2 - 1}} \tan^{-1} \left[\frac{n}{(n^2 - 1)^{1/4}} \right]$$

Equation 5-1

Figure 5-7 shows the theoretical losses associated with various polymer layers at different wavelengths. All of the high-power tests in this work were conducted at the Nd:YAG fundamental wavelength (1064 nm).

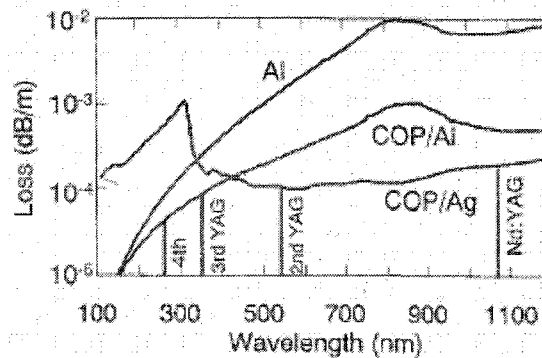


Figure 5-7
Losses of the hollow fiber with a diameter of 1 mm [2].

The hollow core fiber is manufactured by silver plating the inside of the glass capillary tubing. Following the plating process, a mixture of silver nitrate and glucose solution is injected into tubing [2]. The mixture facilitates additional silver deposition. Next, a polymer solution diluted with cyclohexane is injected into the fiber via a peristaltic pump. The mixture is gradually heated until the polymer layer is dried and cured.

5.3.2 Power Transmission and Limits

A bench top experiment was set up to test the transmission characteristics of the flexible hollow core fibers. The light source used for this experiment was a Continuum 8050 Q-switched Nd:YAG laser. The laser has a pulse width of 8 ns and a repetition rate of 5 Hz and was operated at the fundamental wavelength of 1064 nm. The spatial quality of the beam is high, with an M^2 of < 2 as given by the manufacturer.

The beam was aligned using a pair of 2 axis mirror mounts. The mirrors were designed for high intensity operation at the Nd:YAG fundamental wavelength. A series of neutral density filters were used to control the pulse energy of the laser. To avoid spark formation at the launch a helium purge was used [3]. Helium is an inert gas, with a breakdown threshold significantly higher than air. The helium purge is built into the fiber alignment chuck and is shown in Figure 5-8. The helium is supplied through a Teflon tube in the lower right-hand corner. The fiber can be seen to the left of the fiber chuck.

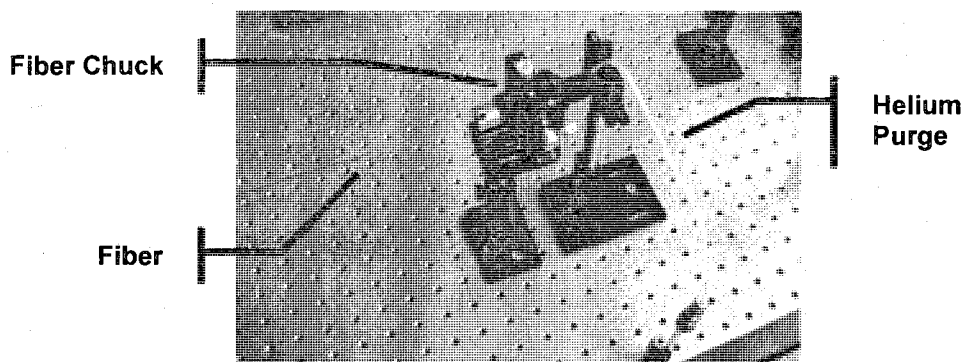


Figure 5-8
Fiber alignment chuck with helium purge.

Precise alignment of the initial 10 cm of fiber length is critical to high transmission [2]. To maintain alignment, a rigid jacket was used to house the initial fiber section. A 5-axis mount was used to align the fiber with the launch beam. A beam profiler was used to optimize the fiber launch by monitoring the beam profile at the fiber exit.

Energy transmission data was recorded with an Ophir PE25 Pyroelectric detector. Several launch lenses and bend radii were used to evaluate energy transmission under various conditions. For the straight configuration, the average input energy was 64.3 mJ, the average output energy was 46.8 mJ. There was little to no variation in output energy for launch lenses with focal lengths between 15 cm and 50 cm. Thus the average transmission efficiency was ~73%. Energy transmission data was also recorded for various bend radii. The three radii tested were 1.37 m, 0.99 m, and 0.78 m (with the initial 10 cm still held straight). The resulting transmission efficiencies are plotted in Figure 5-9.

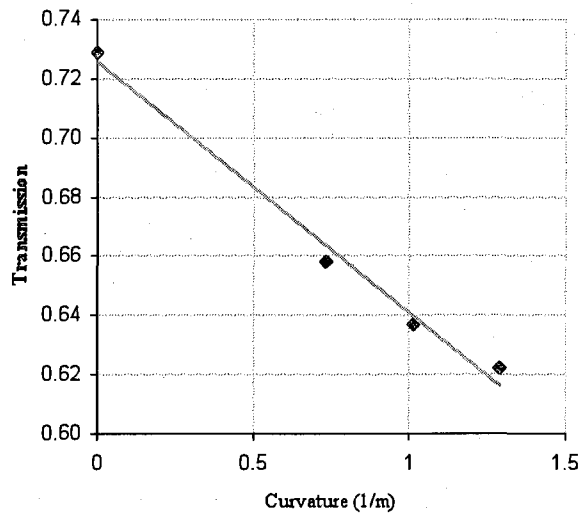


Figure 5-9
Transmission efficiency as a function of bending radius.

5.3.3 Output Beam Quality & Effect of Launch NA

The effect of launch geometry on the fiber exit parameters was also examined. As outlined in Chapter 3, launch exit conditions have a dramatic effect on the fiber's potential to achieve breakdown. Lenses of various focal lengths were used to launch the laser light into hollow core fibers. Three simple plano-convex lenses of 15 cm, 30 cm, and 50 cm were used. The experimental set-up is shown in Figure 5-10.

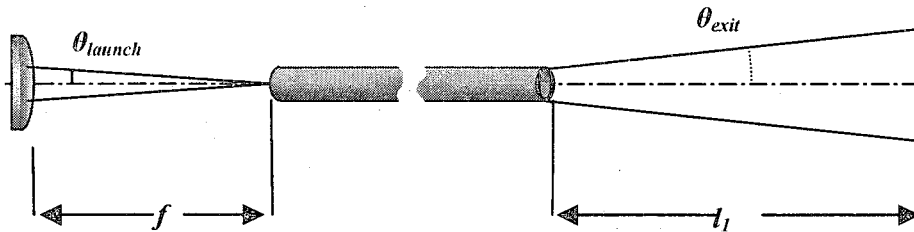


Figure 5-10.
Experimental set-up.

The same launch chuck (5-axis) and helium purge were again employed at the fiber launch. For both straight and bent fiber configurations the beam waist and divergence were measured at the launch, exit, and focal point using a Spiricon LBA710 optical profiler. The beam divergence was measured using the procedure shown in Figure 4-6 (Chapter 4). For intensity calculations, it was assumed that the beam was of uniform intensity (top-hat vs. Gaussian) with a radius equal to the beam waist. Figure 5-11 shows typical intensity profiles at the fiber launch face and at the focal point captured with the beam profiler, which indeed are very close to uniform intensity.

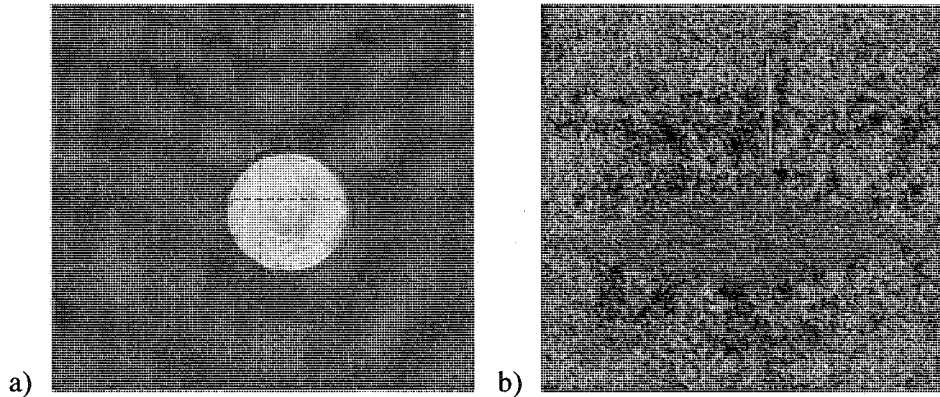


Figure 5-11.
Fiber intensity profiles for the exit face (a) and focal point (b).

Measurements of the beams M^2 value followed the previously described procedure (Equation 3-7) and have an uncertainty of $\pm 15\%$. The Table 5-2 outlines the results of the optical profiling tests, where f_{launch} is the focal length of the launch lens, θ_{launch} is the resulting launch angle, W_{launch} is the waist of the beam at the launch, θ_{exit} is the exit angle, and I_{exit} is the calculated intensity at the fiber exit face.

f_{launch} (cm)	θ_{launch} (rad)	W_{launch} (μm)	θ_{exit} (rad)	M^2_{exit}	I_{exit} (GW/cm^2)
15	0.023	47	0.026	26	1.6
30	0.012	65	0.017	17	1.6
50	0.007	77	0.011	11	1.8

Table 5-2
Effect of launch geometry on fiber output.

5.3.4 Sparking Demonstration

Following the characterization of the output beam (post fiber), focusing optics were used to test the ability of the fiber system to successfully create sparks in air. A pair of double convex lenses were used as focusing lenses to reduce spherical aberration (which would increase the beam waist and decrease intensity). The lenses were placed

approximately 30 cm downstream from the exit face of the fiber, such that ~ 70% of the lens area was filled by the beam. The first lens (upstream) had a focal length of 35 mm while the second lens (downstream) had a focal length of 9 mm. The second lens was located approximately 25 mm behind the first lens. The intensity at the focal point was estimated by calculating the beam waist from profile measurements made at low laser power levels (fitting multiple points to a polynomial curve). Energy data was obtained by redirecting the beam into the energy power meter. No filters were used in the energy measurements as the meter was capable of measuring the power directly.

High power tests were conducted using multiple focal length launch lenses. Each lens reduced the input divergence angle, and hence it was expected that a decrease the exit divergence angle would result. The results are shown in

Table 5-3 where f_{launch} is the focal length of the launch lens, and I_{focus} is the intensity at the focal point. Spark Formation represents the percentage of successful spark events compared to the number of pulses exiting the laser. There are several reasons why spark formation is not 100%, such as slight variations in laser energy, spark formation at the inlet due to dust or other particles, and variations in beam divergence based on actual path through the fiber.

f_{launch} (cm)	I_{focus} (GW/cm ²)	Spark Formation (%)
15	130	<1
30	260	90
50	300	97

Table 5-3
Results of high power tests.

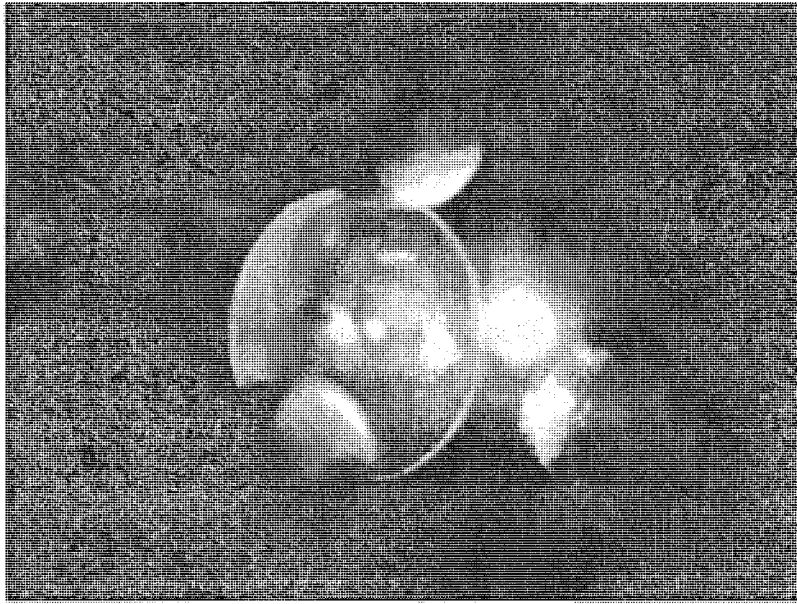


Figure 5-12
Spark formation with a hollow core fiber.

Using the 50 cm launch configuration, the fiber system was again tested at high powers while bending the delivery fiber. For this test the first 40 cm of the fiber was held straight while the remaining 60 cm was bent into arcs of various radii (as in the tests described in Section 5.3.3). The beam profiling system was used to characterize the divergence at the fiber exit which then allowed M^2 to be calculated. Intensity measurements were calculated by measuring the beam waist at the spark location using the procedure previously discussed (polynomial fit). Spark formation was measured using the Ophir energy meter placed behind the spark location. Any laser pulse which failed to produce a spark would register on the energy meter (successful sparks are opaque, and thus block the pulse from the meter). The results of the tests are shown in Table 5-4.

$1/R$ (m^{-1})	θ_{exit}	M^2_{exit}	I_{exit} (GW/cm^2)	E_{peak} (mJ)	I_{focus} (GW/cm^2)	Spark Formation (%)
0	0.011	11	1.8	47	300	97
0.73	0.020	20	1.6	42	190	85
1.01	0.021	21	1.5	41	140	50
1.29	0.024	23	1.5	40	120	< 1

Table 5-4
Results of bent fiber tests.

Where $1/R$ is the radius of curvature, θ_{exit} is the beam exit angle at the fiber face, M^2_{exit} is the M^2 value at the exit of the fiber, I_{exit} is the beam intensity at the exit of the fiber, E_{peak} is the beam energy post fiber, and I_{focus} is the intensity at the focal point (spark location).

Following the successful demonstration of spark formation at the benchtop level, it was decided that the hollow core fiber system should be packaged into a robust housing suitable for trials on-engine. The next chapter describes these efforts.

¹ Saito, Matsuura, Kawamura, Miyagi. (1990). "Bending losses of incoherent light in circular hollow waveguides". *Journal of the Optical Society of America A*. 7, 2063-2068.

² Matsuura, Takada, Yamamoto, Shi, Miyagi. (2002). "Hollow fibers for delivery of harmonic pulses of Q-switched Nd:YAG lasers" *Applied Optics*. 41(3).

³ Sato, Ashida, Shi, Matsuura, Miyagi. (1999). "Hollow-waveguide-based transmission of Q-switched Nd:YAG laser beam for biological tissue ablation". *SPIE Conference on Specialty Fiber Optics for Medical Applications, San Jose, CA*. 3596.

6 Chapter Six - Development of an Optical Spark Plug

Tests utilized laser spark plugs that were designed to be interchangeable with the electric spark plugs used on the Waukesha engine (the engine is described in detail in Chapter 7). This approach allowed for a successful design to immediately be transferred to on-engine testing. It also allowed the plug designs to be tested in a combustion test chamber, which mimicked the geometry of the Waukesha engine. Optical spark plug development occurred in parallel with fiber characterization, and optimization of focusing optics, thus early designs were developed primarily to understand the difficulties of developing a plug which could withstand the temperature, pressure, and vibration of engine operation. In some cases, initial tests used fiber and lens configurations that were later shown to be insufficient. Nonetheless, these tests gave valuable information on practical plug design (sealing, pressure, temperature) and therefore are summarized below.

The first optical plug that was developed consisted of a single focusing lens used in conjunction with a commercially available collimating lens. A meter long solid core fiber was used to deliver light from a Big Sky Ultra laser. The laser and fiber had a launch numerical aperture of 0.22. The coupling between the laser and fiber was achieved through a launch housing that was incorporated into the laser body. This was a commercially available system (other than the laser plug) and was not modified. The fiber was 1 mm in diameter and 1 meter long. The system could safely deliver laser pulses up to 40 mJ with an 8 ns pulse width. The collimating lens coupled to the fiber through a standard SMA type fiber connector. The collimating lens adapter was

adjustable, allowing several mm of travel between the exit face of the fiber and the collimating lens. This travel allowed one to properly fill the collimating lens for various fiber numerical apertures. A photo and schematic of “Plug A” is shown in Figure 6-2.

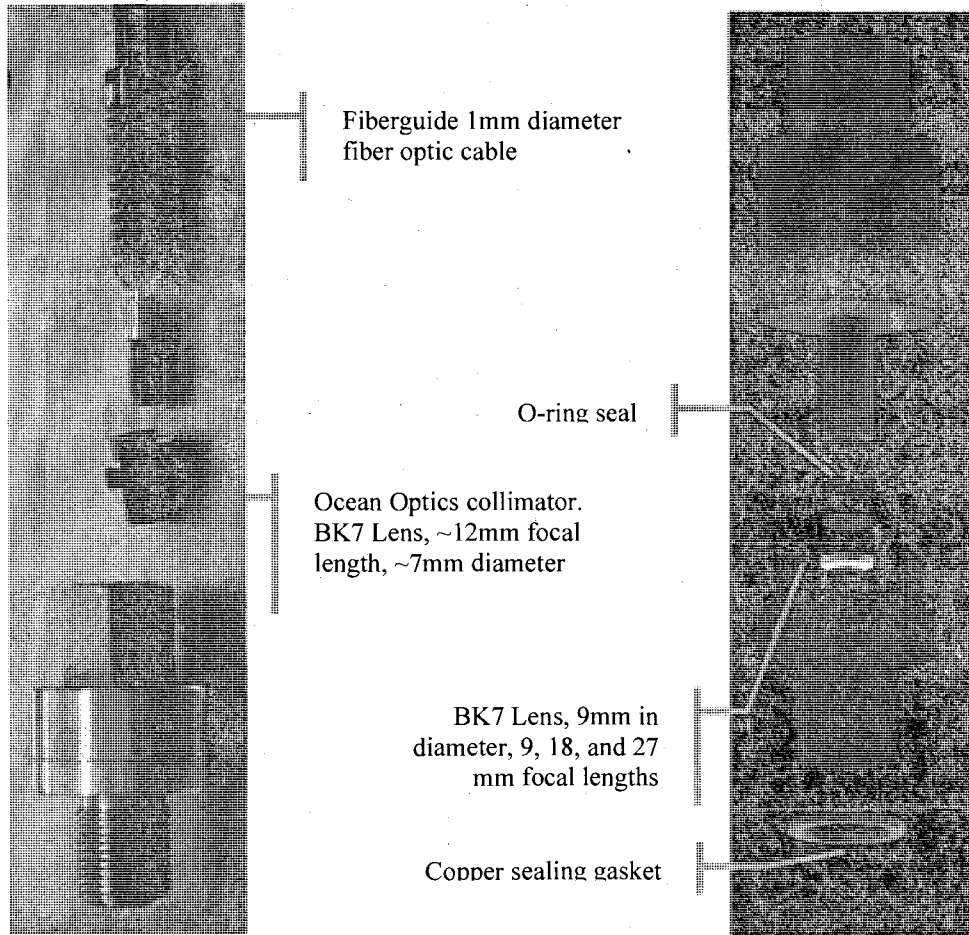


Figure 6-2
“Plug A” Laser Spark Plug.

Plug A was tested with the Big Sky laser system up to 40 mJ (8 ns pulse duration) at both atmospheric conditions and 80 psi. Three different focusing lenses were used

with Plug A; 9, 18, and 27 mm focal length. The lenses were held in place with a Viton[®] a fluorelastomer o-ring which was designed to perform well at high temperatures (200°C). The plug maintained alignment and did not leak up to 5.5 bar, however, the fiber/plug combination did not focus light well enough to achieve breakdown.

A second plug was designed. "Plug B" had several improvements upon the design of Plug A; an achromatic focusing lens replaced the simple focusing lens of Plug A to decrease spherical aberration. The lens had an effective focal length of 9 mm. The design was also changed to ensure that no part of the beam impinged upon the seals. (In Plug A some of the beam was blocked by the o-ring seal, decreasing the effective area of the focusing lens) A drawing of Optoplug B is shown in Figure 6-3.

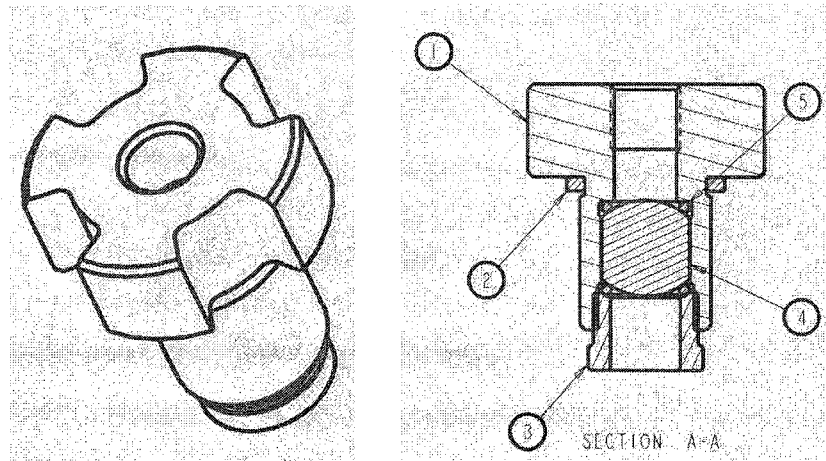


Figure 6-3
"Plug B" Laser Spark Plug

The next design configuration was designated Plug C. The primary change relative to Plug B was the removal of the collimating lens and its replacement with a pair of Gradium[®] lenses. Gradium[®] lenses are manufactured in such a way as to vary the index of refraction from the front surface of the lens to the back surface. This change in

index allows for the correction of system aberrations resulting in smaller spot sizes (at the focal point) than traditional lenses. A drawing of Optoplug C is shown in Figure 6-4.

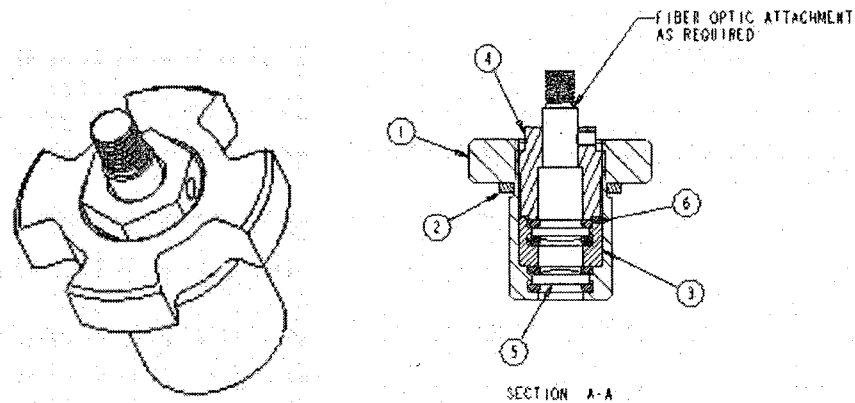


Figure 6-4
"Plug C" Laser Spark Plug

Plug C also failed to achieve breakdown, however this is largely due to combining it with an inappropriate solid fiber. Designs A-C (which utilized both single and multiple lens configurations) all performed well in regards to withstanding the temperatures and pressures of the engine environment while maintaining lens alignment. Therefore, it was determined that the plug design was sufficient until an optimized optical layout could be developed.

The process of designing an optimized optical layout is described in Chapter 4. This optical layout was designated "Design D" and integrated into a stainless steel housing to create "Plug D". The housing has three interior sections that are sandwiched together to hold the optics in place. In addition, a sapphire window was added to the plug to provide an additional seal from combustion gases. The interior of the plug was designed using the ray trace information from Zemax model, to ensure that the beam

did not impinge on the interior walls or seals of the plug. Similar to previous designs, a copper gasket was used to seal the body of the plug to the piston head. Drawings of Plug D are show in Figure 6-5, Figure 6-6, and Figure 6-7.

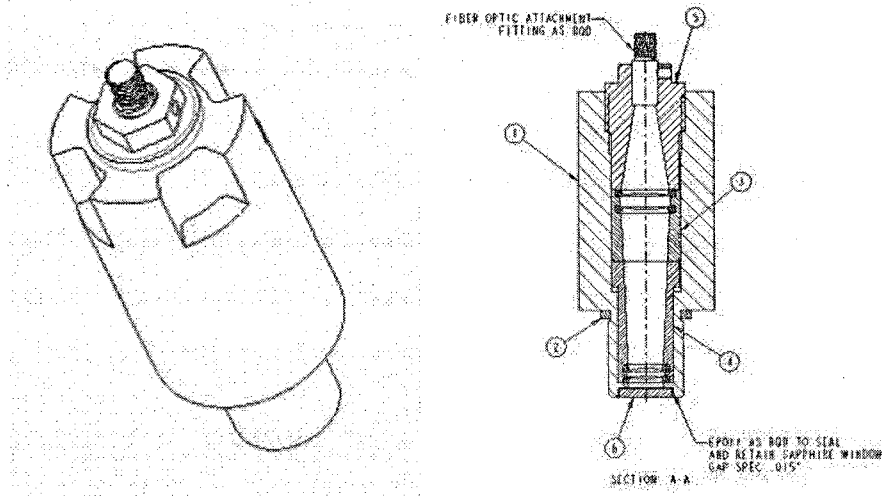


Figure 6-5
Optoplug D

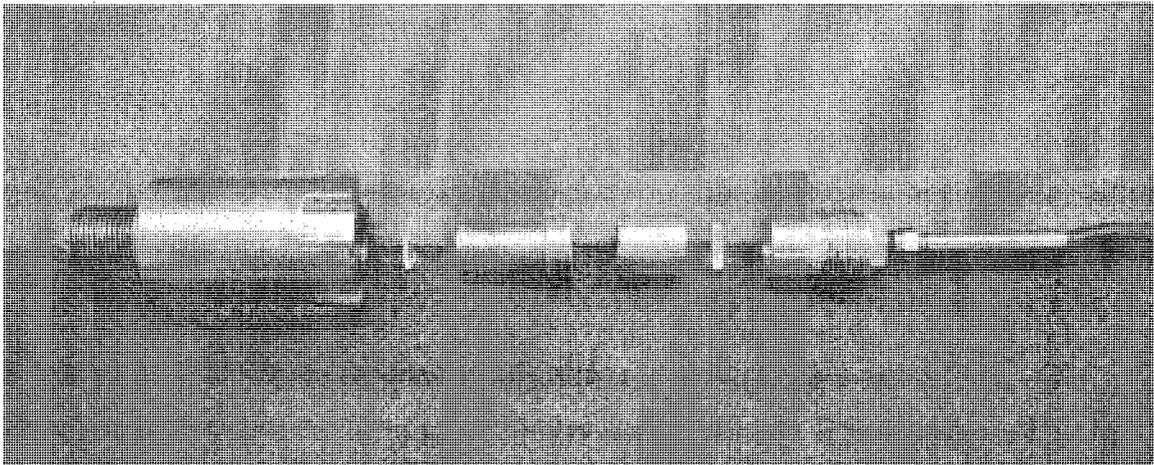


Figure 6-6
Photograph of Plug D including lenses and fiber

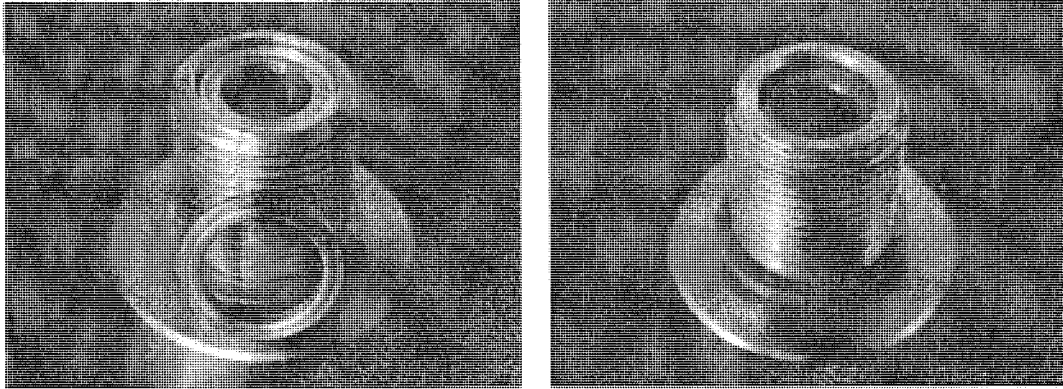


Figure 6-7
Mounting the sapphire window of Optoplug D. A retainer ring is welded on to the end of the plug to cap the window.

Plug D was pressure tested to ensure that it could withstand the combustion pressures of the Waukesha engine. Passing the pressure test, Plug D was used for on-engine testing of the laser ignition system, which is outlined in the next chapter.

7 Chapter Seven - Engine Testing

7.1 Introduction

Following the successful demonstration of spark formation on a bench-top apparatus, an on-engine test was needed to demonstrate the system on an actual engine. The engine environment presents many operational challenges, vibration being the most obvious, thus from the start, the design of the on-engine ignition system focused on rigid components that could be precisely assembled. The geometry of the engine itself also was a challenge; the vertical arrangement of the cylinders on the test engine forced the laser to hang directly above the engine and point down into the cylinder if an unbent fiber was to be tested. Therefore, a method of hanging the laser from above was required. The on-engine system had to maintain precise alignment between the laser, launch optics, fiber, and focusing optics. Finally, the system had to allow for a vacuum to be drawn around the fiber launch, so as to avoid unwanted breakdown (spark formation) at the fiber launch.

7.2 Optical Design

Given the aforementioned constraints on the location of the laser relative to the engine, the large bench-top laser used in the experiments described in the previous chapter was not appropriate. A New Wave "Gemini" Nd:YAG laser (120 mJ peak energy, 7 ns pulse width) was implemented with similar results to those described in Chapter 5. The required energy needed to form sparks decreased from 39 mJ to 13 mJ

due to a decrease in the number of optical components (absorptive filters, mirrors, lenses, etc.) in the beam path. Reducing the components reduced loss while also improving the beams spatial quality. The results of these bench-top lab tests guided the approach to on-engine implementation. The first consideration was to improve or eliminate the helium purge used to suppress sparking at the fiber input face. Previous work by Matsuura [1] showed that operating at vacuum pressures is more effective at suppressing sparks than a helium purge. Therefore, the housing design for the fiber and associated optics is based on providing a vacuum environment for the fiber (by connecting a compact vacuum pump to a sealed fiber system).

7.2.1 Optical Train

The components of the optical train are shown schematically in Figure 7-1. The system consists of two “vacuum fiber chucks”, a “launch lens tube”, and an “optical spark plug”. The vacuum fiber chucks hold the hollow core fiber in place and allow for a vacuum to exist throughout the assembly. The launch lens tube aligns the launch lens with the first vacuum fiber chuck. The optical spark plug focuses the light exiting the hollow core fiber and is compatible with the existing spark plug well on the engine cylinder. Lenses (not shown in the figure) are used to launch the beam into the fiber, and to re-focus the light exiting the fiber in the same manner as the previous bench-top experiments.

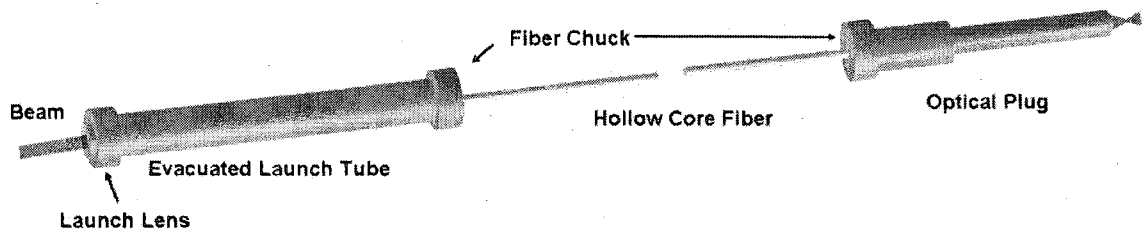


Figure 7-1.
Schematic diagram of the on-engine laser ignition system.

Alignment of the beam into the apparatus is critical. The original mounting plate housing the second harmonic generator (used to create the $0.532 \mu\text{m}$ beam) of the Gemini laser was removed and replaced with a mounting plate holding two mirrors to control beam alignment as shown in Figure 7-2. The plate is kinematically mounted using three steel ball bearings on the underside to ensure accurate and repeatable placement. The two mirrors are adjustable on three axis, with lock down screws and high tension spring mounts to ensure that the beam position does not drift, even in a high vibration environment. Four stainless steel pegs are used in conjunction with two right angle mounts to rigidly mount the launch lens tube to the laser.

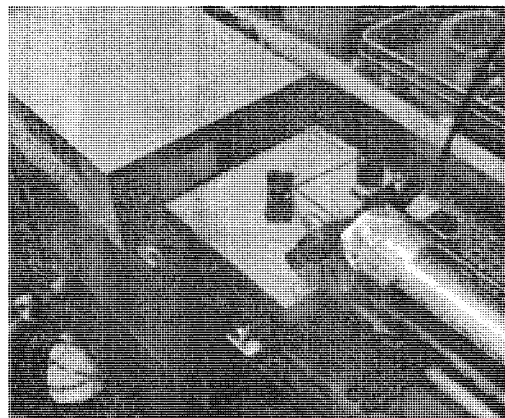


Figure 7-2.
Beam alignment plate.

A flange housing around the launch lens is used to seal the end of the launch lens tube shown in Figure 7-3. Press fit pins on the flange are used to align the launch lens with the tube body. The tube's purpose is two-fold; it must allow for a rough vacuum throughout the system, and must also hold the launch lens perpendicular to the fiber chuck at the appropriate distance. The launch lens is sealed in the flange with an o-ring. The vacuum inside the tube pulls the lens against the o-ring achieving an air-tight seal.

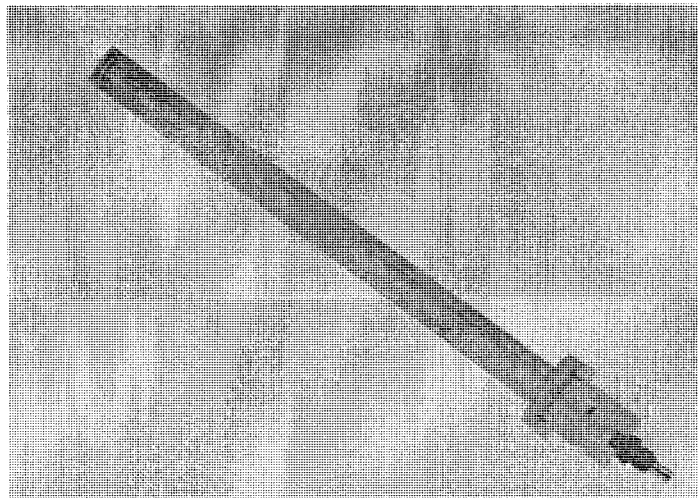


Figure 7-3.
Launch tube. Beam enters from left.

The fiber chuck holds the hollow core fiber in alignment with the launch tube. To accomplish this, the fiber is first held by a much smaller brass fiber chuck, which can be seen in rightmost drawing of Figure 7-4. This brass chuck is commercially available, and uses a plastic collet to gently squeeze the fiber. This brass chuck is held by the larger aluminum vacuum fiber chuck, using a small set screw to fix its location.

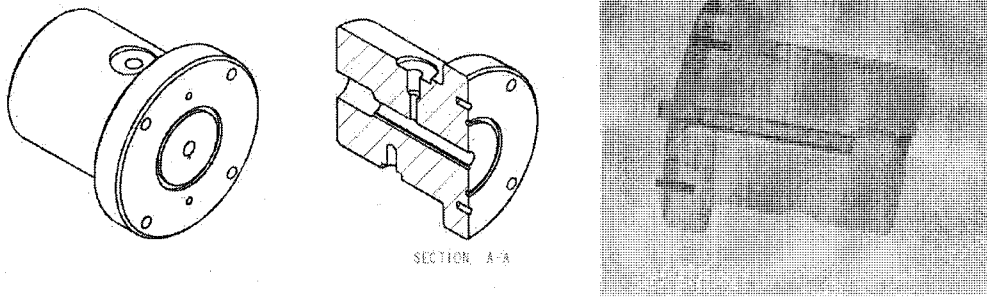


Figure 7-4.
Three views of the vacuum fiber chuck.

On the input side of the chuck, a o-ring seal mates with the launch lens tube. Once again, press fit pins are used to align the two pieces. A small channel below the brass chuck is drilled to allow the vacuum to pass into downstream components. NPT treads on the outlet side of the chuck are used to connect the vacuum fiber chuck to a length of 1/8" stainless steel tubing (Swagelok). A second vacuum fiber chuck on the other end of the tubing is used in a reverse fashion to couple the outlet of the hollow core fiber to the optical spark plug. The optical spark plug houses two lenses used to focus the light pulse into a spark after the fiber exit as shown in Figure 7-5. A sapphire window, sealed with aluminum washers, protects the assembly from combustion pressures. The entire system is evacuated to ~ 1 torr using a Welch Duo Seal vacuum pump. The low pressure aids in reducing inadvertent sparking at the fiber input and improves the energy transmission.

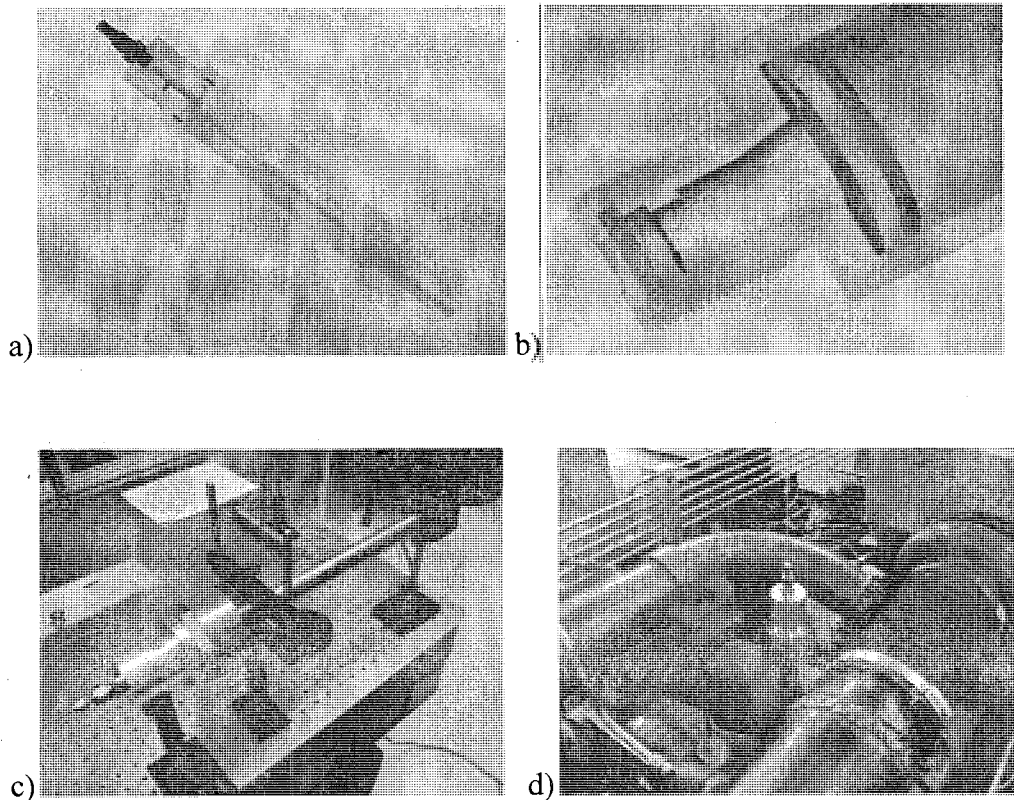


Figure 7-5.

Solid models and photos of the on-engine testing components: a) solid model of the fiber chuck and optical launch b) detail of the optical spark plug showing lens pair and sapphire window c) bench testing of optical spark plug (energy meter is positioned to the right of the plug) d) optical spark plug mounted on a single cylinder of the engine.

The engine mounting assembly secures all the components of the ignition system in a manner that allows for precise positioning of the laser relative to the fiber launch, and allows us to test multiple fiber bend radii. Photos of the laser ignition system mounted to the engine are shown in Figure 7-5. Guide wires help stabilize the mounting assembly from excessive vibration. Heat shields are applied to the laser, exhaust, and turbocharger to direct radiation away from the laser. The fiber and optical spark plug are not shielded, as they both are capable of withstanding temperatures in excess of 500° C.

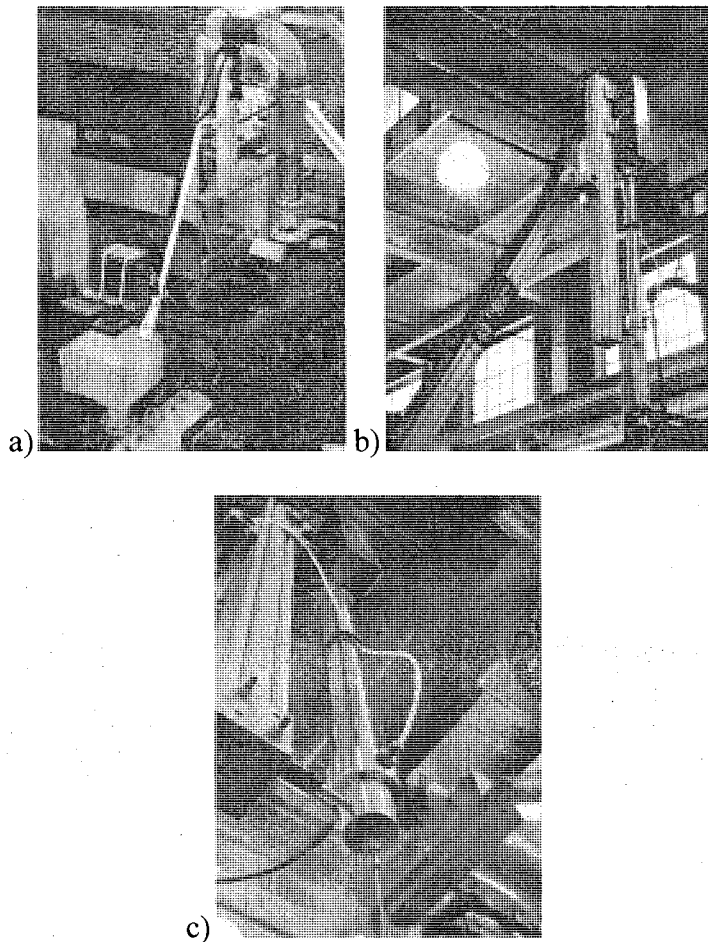


Figure 7-6.
 Photos of the on-engine mounting assembly: a) view from above showing entire assembly, note laser power supply in lower left corner (exhaust head shield not shown); b) view of adjustable arm allowing multiple fiber bend radii; c) detail of fiber launch, laser in upper left of photo is directed through launch tube into fiber. Teflon vacuum line (white) is also visible.

7.2.2 Vibration Isolation

While the on-engine mounting shown in Figure 7-6 allowed for multiple bend radii (by angling the laser assembly), it was too rigidly mounted to the engine, and as a result, during the preliminary engine testing, only intermittent ignition was observed. Pressure traces from igniting cycles as well as misfire cycles are shown in Figure 7-7. The misfire cycles simply show the engine motored pressure. In the traces showing combustion, the combustion occurs late in the cycle is late, i.e. delayed relative to the

appropriate time. This delay is due to operating the engine at conditions of no load and low speed. Note that this delay was not associated with problems of the timing and engine control hardware (which worked as designed). Analysis of the data and optical system indicated that misfires were likely due to vibration of the system (caused by the engine), which led to misalignment of the beam position at the fiber launch. Owing to the small spatial tolerances required to properly launch the laser beam into the entrance of the hollow fiber (on the order of 100 μm), even relatively small vibrations can cause sufficient beam deflection and prevent proper fiber launch and laser light delivery. (This assertion was also validated by the finding that the spark delivery system worked correctly both before and after the engine test, when tested on the non-vibrating bench-top.) The vibrations did not affect the performance of the laser itself, but did prevent proper coupling of the laser light into the fiber.

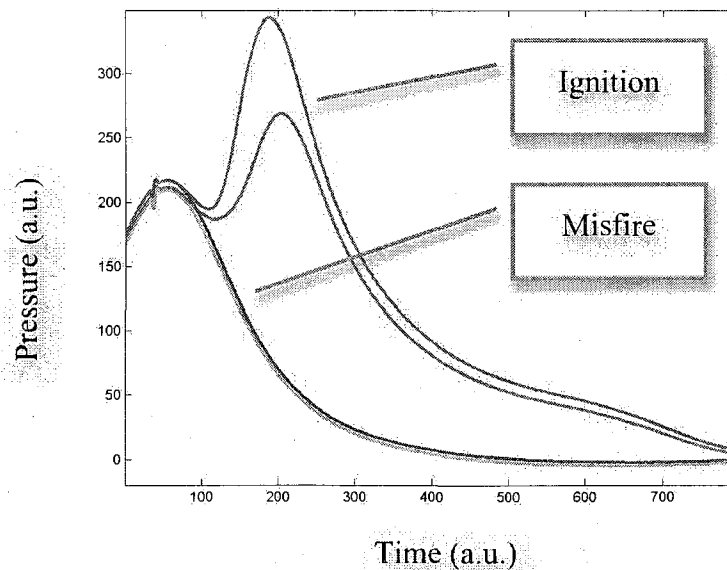


Figure 7-7.

Four pressure traces from preliminary engine testing (arbitrary units). The vertical axis is pressure, and the horizontal axis is time, both in arbitrary units.

A vibration isolation mount was designed to decouple the system from the vibrations of the engine, and thus eliminate the aforementioned problems. The relatively large mass of the on-engine laser system, combined with the high frequency vibrations from the engine made solution very simple. Four springs with resonance well below 1kHz were used to suspend the system. A pair of rubber ring dampers were added to further reduce the likelihood of a resonant frequency being excited. The damping system is shown in Figure 7-8.

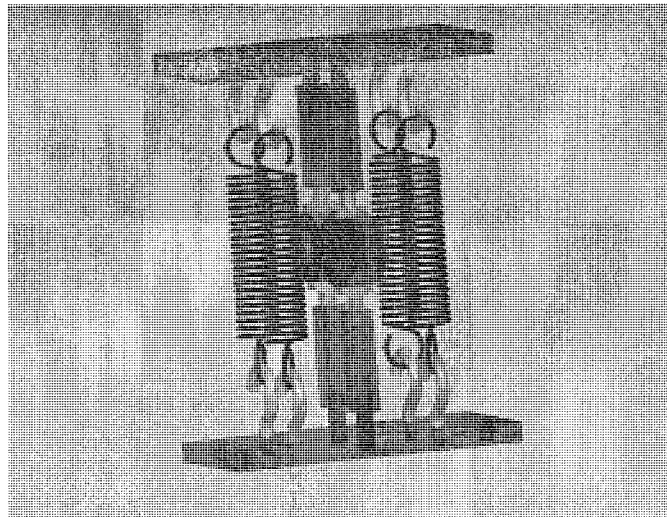


Figure 7-8.
Spring and damper vibration isolation mount.

The damping system was integrated into the on-engine mounting assembly as shown in Figure 7-9. A pair of alignment brackets can be seen near the bottom of the laser system, these brackets were not hard mounted to the laser system. The entire system was in fact coupled only through the vibration isolation mount.

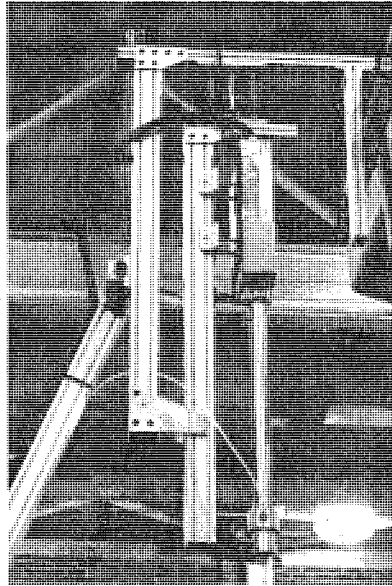


Figure 7-9.
On-engine mounting system integrated with vibration isolation mount.

Test Results

The equipment used to control the ignition timing and data acquisition is shown in Figure 7-10. An oscilloscope provides real-time confirmation of ignition and verifies triggering alignment with TDC (top dead center). A high-speed data acquisition system (Hi-Techniques Win600) combustion analysis system records pressure data from the cylinder and sends a trigger to the pulse generator, which is nominally 20-40 degrees BTDC (before top dead center). The pulse generator sends an output signal to trigger the laser firing (and thus the spark formation and cylinder ignition) by adding an appropriate delay to achieve the desired ignition timing.

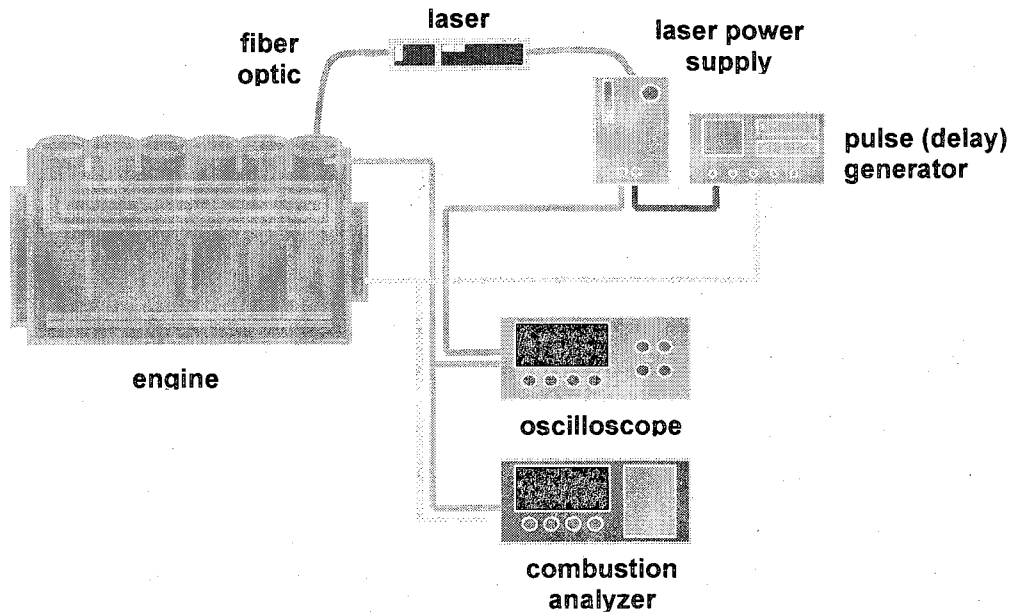


Figure 7-10.
Schematic of the ignition timing control and data acquisition set-up.

A single cylinder of an inline 6-cylinder Waukesha VGF turbocharged natural-gas engine was used to test the laser ignition system (the remaining cylinders (# 1-4, 6) were not altered and ran with conventional spark ignition). The engine has a nominal rating of 400 bhp continuous at 1800 rpm. The engine displacement is 18 liters, with a cylinder bore of 5.98 inches and a stroke of 6.5 inches. Engine loading was achieved using a 1,200 hp Midwest eddy current dynamometer. For functional testing the engine speed was limited to 1500 rpm and load was limited to 35% of rated. Lower loads are more challenging for laser ignition because of lower pressure and high-energy input for sparking and consequent ignition.

The laser ignition system was coupled to cylinder number five. The timing of the remaining cylinders was kept at the original setting, nominally 14° BTDC. The timing of the laser-ignited cylinder (#5) was controlled independently, and retarded to 8° BTDC to match the location of peak pressure.

7.2.3 Ignition Reliability

The previous system (without vibration isolation) ignited the mixture only sporadically. However, with the vibration isolation system in place, during a 1000 cycle datapoint no misfires are found. While this is a good indicator that ignition is reliable, additional testing would be required to report a statistically valid measurement of misfire.

7.2.4 Rate of Pressure Rise

Figure 7-11 shows the pressure traces of all cylinders, where each trace is an average of 1000 cycles. It was observed that even with the timing delayed on the laser-ignited cylinder, peak pressure was reached before all other cylinders, indicating an increased rate of heat release.

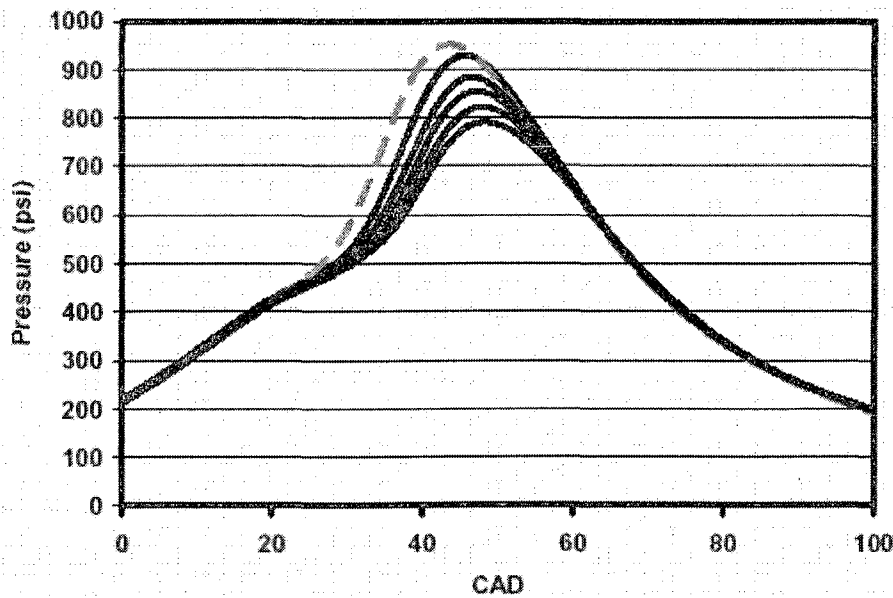


Figure 7-11.

Pressure curves for laser and electrical spark ignition. Laser ignition is used on cylinder #5 only (indicated by dotted curve).

7.2.5 Mass Fraction Burned

The mass fraction burned as a function of crank angle was calculated for all cylinders using an averaged polytropic coefficient as determined by the Hi-Techniques combustion analyzer using a single zone heat release model. Results are shown in Figure 7-12 and Table 7-1. The spark timing for the laser ignition cylinder was controlled independently of the other cylinders. The timing was adjusted such that the peak pressure of cylinder 5 (laser ignition) would occur at roughly the same crank angle as the other 5 cylinders. To achieve this alignment of peak pressures, the spark timing had to be retarded from the nominal 14° before top dead center ($^\circ$ BTDC) to 8° BTDC. This change is solely the result of improved flame kernel formation during the initial phase of combustion. The burn duration from 0-10% is between 8° and 10° shorter for laser ignition, while the burn duration from 10% to 90% is similar for all cylinders. This is anticipated, as the primary influence of laser ignition is decreased induction time and increased rate of flame kernel growth early in combustion. Once the flame kernel is established, the flame propagation rates through the cylinder should be similar. The data obtained during this round of engine testing supports this assumption.

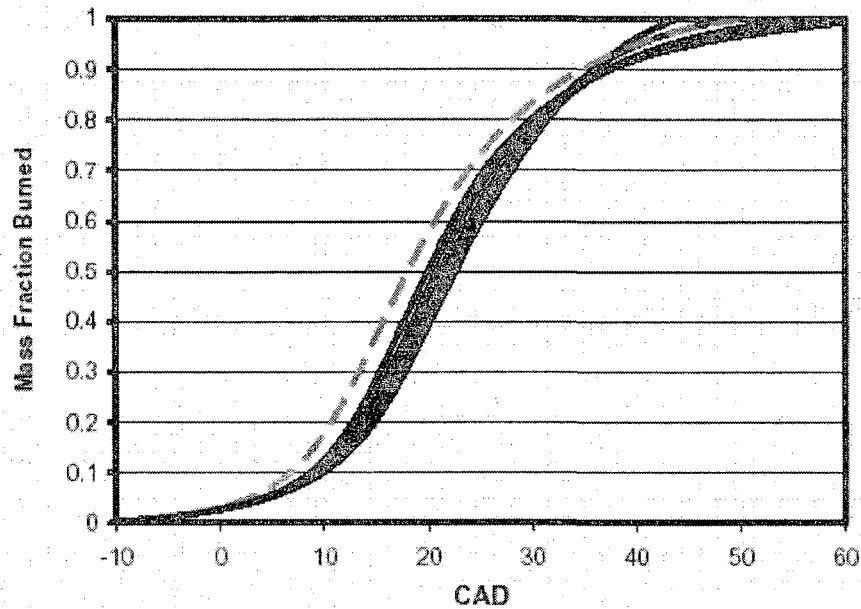


Figure 7-12.
Mass fraction burned as a function of crank angle. The dashed line is laser ignition.

Cylinder #	Spark Timing (°BTDC)	0-10% Burn (CAD)	10-50% Burn (CAD)	10-90% Burn (CAD)	Average Peak Pressure (psi)	COV of Peak Pressure (%)
1	14	22.8	11.5	29.0	935	5.26
2	14	24	12.3	26.3	827	6.84
3	14	23.8	12.0	27.8	861	7.36
4	14	24	12.8	26.3	796	7.27
5*	8	15	11.8	28.0	957	5.65
6	14	23.3	11.8	28.3	890	6.05

Table 7-1
A comparison of combustion characteristics between laser ignition and conventional ignition. *cylinder 5 is the laser ignition system.

7.3 Combustion Stability

As discussed previously, combustion instability limits lean operation in an internal combustion engine, and concurrently bounds the efficiency and emissions performance of lean-burn engines. By improving combustion stability it is possible to expand these boundaries.

From Table 7-1, it can be seen that the laser ignition system (cylinder 5) had one of the lowest coefficients of variation (COV) of peak pressure of any of the cylinders. The coefficient of variation is simply the standard deviation of the peak pressures for the sample data. In this case, over 1000 pressure traces were analyzed to determine the COV of peak pressure numbers reported.

Note that while the COV of peak pressure for laser ignition is much lower than that of most of the other cylinders, it is not the lowest. Cylinder 1 has the lowest COV of peak pressure. This point was raised with the engine manufacturer as it has been noted in other engine testing programs that Cylinder 1 generally has different combustion characteristics than the other cylinders. It is hypothesized that the air/fuel mixing in the intake manifold results in a slightly richer mixture in cylinder 1, thereby reducing its COV of peak pressure relative to the other cylinders.

¹Matsuura, Hanamoto, Sato, Miyagi. (1998). "Hollow-fiber delivery of high-power pulsed Nd:YAG laser light". *Optics Letters*. 23(23), 1858-1860.

8 Chapter Eight – Conclusion

Industrial natural gas engines will likely continue to play an important role in power generation applications. Their advantages in terms of capital cost and efficiency make them ideal candidates for distributed power generation and combined heat and power applications, two technologies that are likely to be widely adopted as the demand for energy rises and concerns of global climate change grow.

Improved ignition systems are one of the few remaining in-cylinder paths to future reduce emissions and improve the efficiency of industrial natural gas engines. Laser ignition was first demonstrated (Dale et al.) over 30 years ago, however, the technology has only recently been considered plausible. A key barrier to the implementation of laser based ignition systems is the need to safely and reliably contain the laser beam. While fiber optic cables are an obvious choice, prior to this work, there existed no demonstration of successfully delivering high power laser pulses (suitable for engine ignition). Therefore, the aim of this work was to address many of the practical impediments to laser based ignition systems.

Demonstrating fiber optic delivery of high power laser pulses was the primary optical challenge faced in this work. There are several competing fiber delivery systems being explored by various researchers around the world today. To our knowledge this work represents the first (at the time) demonstration of delivering high power, nanosecond pulses to form sparks in atmospheric pressure air, both on a bench top and on

engine. Work at CSU continues to build on the system described in this dissertation with the development of a multiplexing system compatible with hollow core fibers, as well as optical diagnostic techniques which will use the fiber system to retrieve spectral information from the laser spark and subsequent flame which will yield air/fuel ratio and temperature information. Photonic Crystal Fibers (PCF's) are also under exploration at CSU, a technology in which a periodic hole-silica structure in the fiber modifies the refractive index of the cladding allowing for single mode operation at fiber diameters roughly 1.5-2 times greater than traditional single mode fibers.

Outside of CSU, researchers at GE Jenbacher and the Technical University of Vienna as well as the National Energy Technology Laboratory (in the United States) are working on alternative configurations of laser based ignition systems [1,2]. Their approach is to deliver laser pump light (via diode sources) to small passively Q-switched, end pumped lasers housed on each cylinder of the engine.

Ultimately, between the approaches developed at CSU and elsewhere, the trajectory of the technology is encouraging. If and when the issue of fiber optic delivery is "solved" there will be several remaining mechanical issues to implementation, many of which this work begins to address. Optical spark plugs must survive a high temperature, high vibration environment. In addition, there are lifetime, reliability, and cost issues that must be addressed in a commercial application. Here we have shown that optical spark plugs can operate on engine while maintaining alignment, sealing combustion pressure,

etc. We have also shown that low misfire rates are possible, as well as demonstrated that laser ignition has a reduced induction rate, which corresponds to improved combustion.

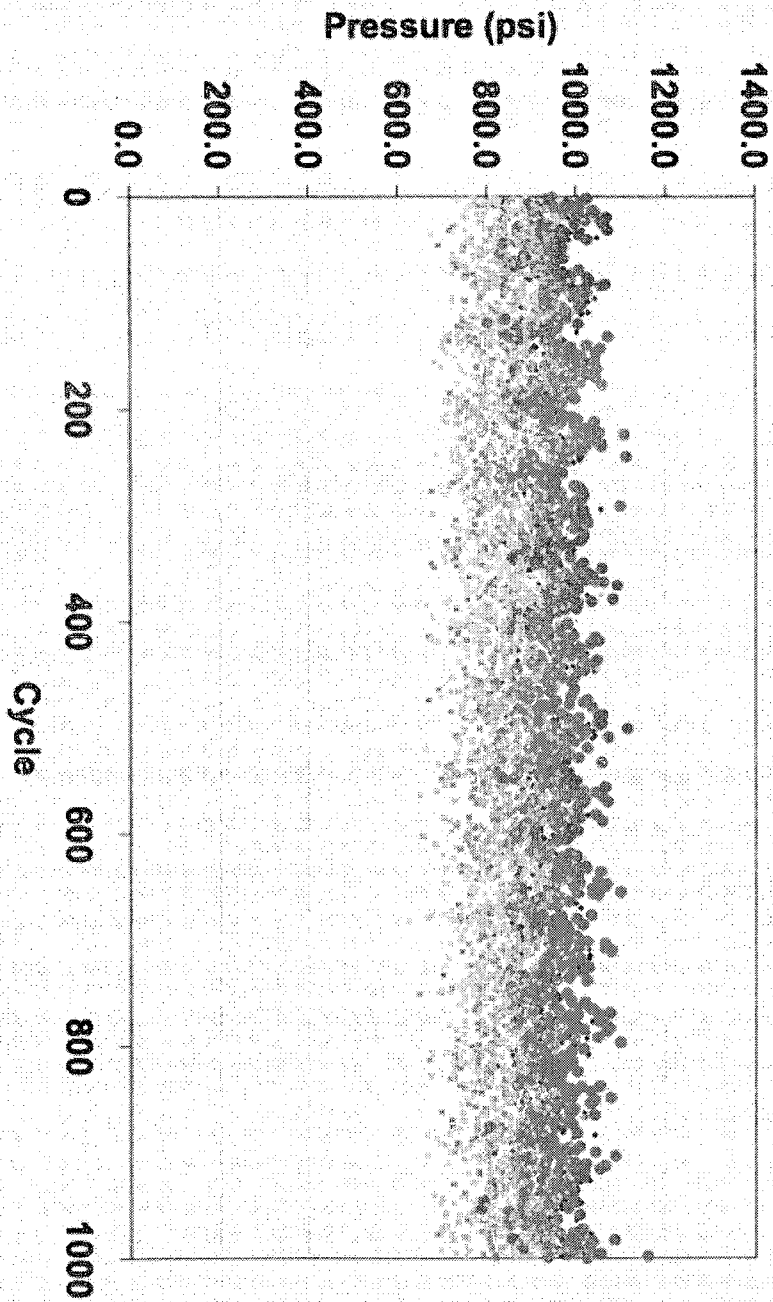
Taken together, these findings indicate the potential value and practicality of laser based ignition systems for industrial natural gas engines. While many technical challenges remain, this work has provided a groundwork for future efforts, which should lead to the commercialization of the technology.

¹ McMillian, Woodruff, Richardson, McIntyre. (2004). "Laser Spark Ignition: Laser Development and Engine Testing". *Proceedings of ICEF2004, ASME Internal Combustion Engine Division 2004 Fall Technical Conference*. ICEF 2004-917.

² Kofler, Tauer, Tartar, Iskra, Klausner, Herdin, Wintner. (2007). "An innovative solid-state laser for engine ignition". *Laser Physics Letters*. 4,322-327.

9 Appendix A: Peak Pressure Plot

Peak Pressure (Cylinder #5 Laser Ignition in Bold)



10 Appendix B: Engine Data

Date of Engine Test	8-Jun-05
Engine	Waukesha VGF
Cylinders	6
Speed	1500 rpm
Load	500 ft-lbs

Engine Geometry

Bore	5.98	inch
Crank Radius	3.25	inch
Con Rod Length	12.2	inch

Spark Timing

Cylinder 1	14.0	degrees BTDC	spark plug
Cylinder 2	14.0	degrees BTDC	spark plug
Cylinder 3	14.0	degrees BTDC	spark plug
Cylinder 4	14.0	degrees BTDC	spark plug
Cylinder 5	7.7	degrees BTDC	laser ignition
Cylinder 6	14.0	degrees BTDC	spark plug

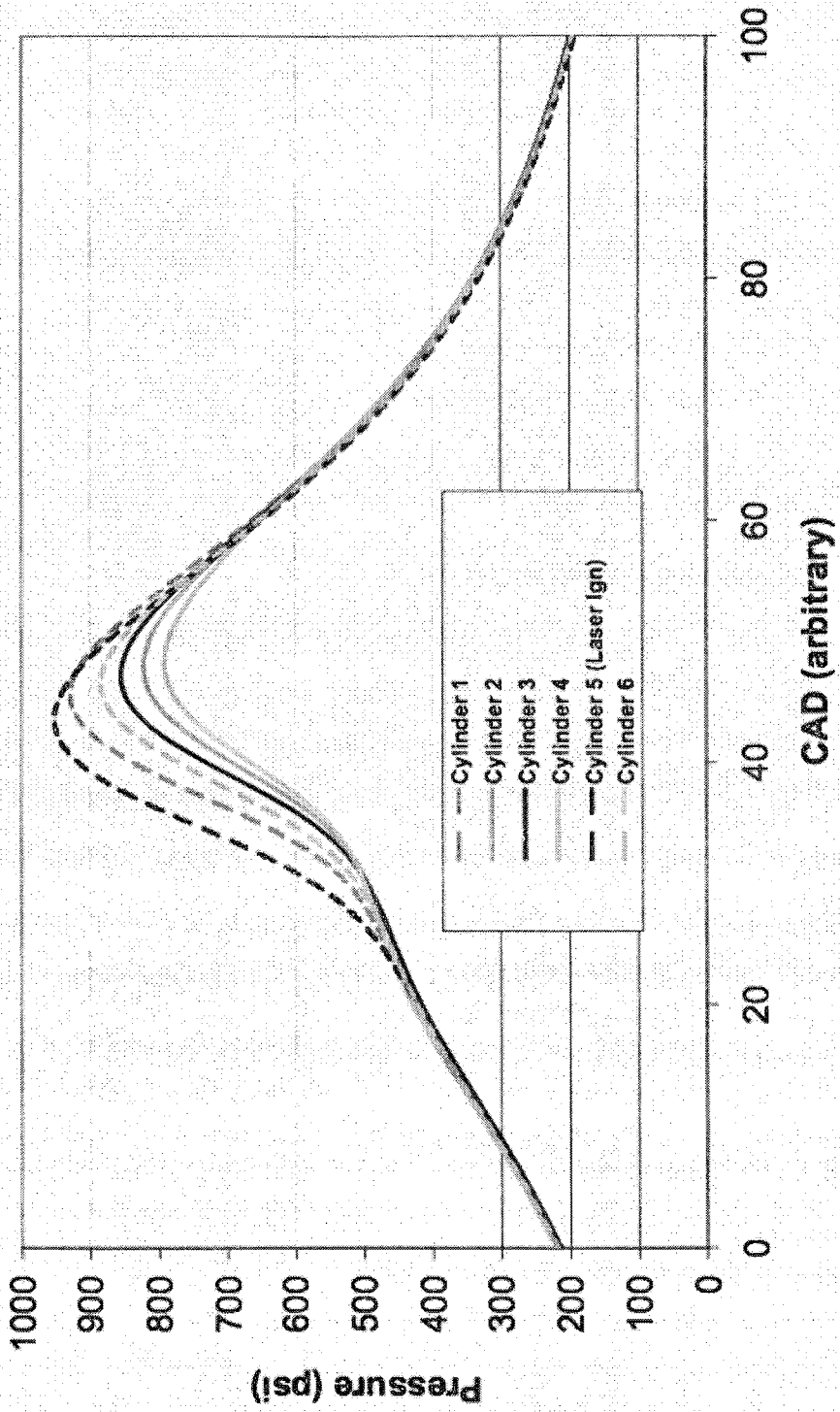
Pressure Correction Info.

<i>Multipliers (pC/psi)</i>	<i>used for original data</i>	<i>should have used</i>
Cylinder 1	0.965	1.81
Cylinder 2	0.965	1.79
Cylinder 3	1.81	1.81
Cylinder 4	1.81	1.81
Cylinder 5	1.79	1.78
Cylinder 6	1.81	1.79

11 Appendix C: U.S. Patent # 7340129

12 Appendix D: Cylinder Pressure Trace

Laser Ignition Test Results (1000 cycle average)



13 Appendix E: Engine Data

Laser Ignition Data from June 8, 2005						
Laser Ignition on Cylinder #5						
Average Peak Pressure						
Cylinder 1	Cylinder 2	Cylinder 3	Cylinder 4	Cylinder 5	Cylinder 6	
934.8	827.2	861.4	795.9	956.8	890.0	
Standard Deviation of Peak Pressure						
Cylinder 1	Cylinder 2	Cylinder 3	Cylinder 4	Cylinder 5	Cylinder 6	
49.15	56.59	63.37	57.88	54.06	53.80	
COV of Peak Pressure						
Cylinder 1	Cylinder 2	Cylinder 3	Cylinder 4	Cylinder 5	Cylinder 6	
0.0526	0.0684	0.0736	0.0727	0.0565	0.0605	
cycle	Cylinder 1	Cylinder 2	Cylinder 3	Cylinder 4	Cylinder 5	Cylinder 6
1	933.2	888.8	887.9	765.6	946.1	818.7
2	914.2	843.1	811.2	774.1	1024.2	859.0
3	979.5	804.8	811.2	737.7	929.7	915.7
4	944.0	858.9	878.1	830.0	1012.4	922.9
5	834.4	886.8	809.5	803.4	922.3	877.7
6	915.4	852.5	822.9	792.7	936.8	813.0
7	815.0	772.6	859.1	772.2	892.3	903.1
8	812.7	795.2	928.4	761.2	988.6	904.6
9	941.3	782.6	921.6	885.2	974.1	881.9
10	1007.4	818.4	874.2	765.3	952.0	931.8
11	954.3	833.9	863.7	805.4	1007.5	845.6
12	950.5	874.0	872.3	850.3	969.9	911.0
13	882.3	930.1	784.9	753.6	1036.9	935.2
14	913.8	838.6	890.1	865.2	976.8	885.9
15	1043.1	838.0	857.1	791.2	903.4	900.9
16	947.8	910.0	831.7	855.2	1043.3	795.3
17	1027.3	865.9	894.0	776.8	968.0	947.6
18	920.6	836.7	880.3	846.4	1002.8	843.2
19	893.9	845.7	913.0	745.3	1005.5	948.3
20	896.6	843.6	917.7	754.1	1068.4	957.2
21	983.2	892.5	841.0	886.7	1017.1	898.7
22	848.5	828.8	911.1	790.7	1053.6	1017.4
23	902.7	833.5	978.0	822.9	1022.2	932.8
24	901.2	788.2	848.8	874.0	1056.3	959.2
25	1023.0	839.4	950.1	780.0	922.8	840.4
26	941.0	902.6	786.3	915.5	997.2	876.7
27	962.1	870.5	947.7	730.9	1062.0	893.5
28	926.4	723.7	923.8	880.6	940.5	950.3
29	970.0	821.0	863.5	822.7	869.7	947.1
30	955.7	808.9	853.7	795.6	949.8	825.4
31	913.5	838.1	919.4	814.4	952.2	896.2
32	1015.1	716.1	831.0	751.7	1071.1	880.2
33	931.9	872.6	796.3	722.4	972.4	863.9
34	987.9	892.2	918.2	904.7	921.1	842.7
35	906.1	863.6	873.2	912.8	945.6	928.3
36	846.6	812.1	819.3	674.3	1006.0	946.3
37	938.5	821.0	853.2	831.0	955.4	900.2
38	956.9	871.1	754.3	879.8	973.1	827.1

cycle	Cylinder 1	Cylinder 2	Cylinder 3	Cylinder 4	Cylinder 5	Cylinder 6
39	1047.6	875.2	1003.6	759.2	958.6	882.7
40	978.4	765.9	925.2	842.2	947.8	936.7
41	985.3	844.4	892.8	865.4	1025.4	905.6
42	1017.8	797.4	814.4	808.5	961.6	914.5
43	960.8	851.9	947.9	765.6	917.1	820.7
44	958.5	861.7	839.3	753.9	834.9	847.8
45	928.4	825.2	870.8	845.6	889.6	900.9
46	863.7	690.8	939.4	769.0	935.3	871.1
47	890.0	748.3	769.0	842.7	935.3	875.7
48	887.1	837.7	770.9	819.0	970.9	920.4
49	923.3	785.9	798.5	887.6	914.4	899.4
50	914.6	794.8	880.8	780.5	911.5	911.8
51	955.5	746.4	820.7	786.8	954.4	838.5
52	918.6	804.7	853.7	924.3	924.3	832.5
53	916.3	824.6	790.0	822.2	957.4	921.7
54	945.0	832.8	811.5	794.9	829.5	846.1
55	939.2	792.0	768.3	723.6	882.3	848.1
56	947.4	782.8	815.1	771.2	934.6	913.0
57	893.8	848.4	810.7	774.1	930.6	880.7
58	926.0	825.1	750.2	734.3	971.4	933.5
59	893.6	845.6	876.7	787.1	955.2	881.4
60	930.5	845.0	908.9	721.6	942.4	819.0
61	879.6	831.5	768.7	806.8	862.4	820.9
62	959.1	856.9	882.8	893.0	953.2	858.0
63	889.9	726.1	864.7	828.8	877.8	882.9
64	839.1	740.1	930.6	739.7	913.2	836.5
65	934.1	856.5	785.3	721.6	908.3	859.0
66	845.0	750.6	746.3	779.7	862.6	917.2
67	935.9	731.6	800.5	752.6	933.3	928.1
68	971.5	850.2	852.5	791.9	909.5	800.9
69	950.0	862.9	813.4	833.4	1007.5	908.3
70	908.9	837.1	887.4	756.5	935.3	842.7
71	970.2	813.1	820.0	799.3	957.6	908.3
72	883.7	853.6	830.5	812.0	938.0	852.8
73	898.6	769.5	891.3	721.4	990.0	871.3
74	979.4	749.5	859.1	887.9	977.5	896.5
75	903.5	755.1	812.4	820.3	960.8	901.2
76	915.4	843.1	859.3	806.6	1024.2	943.4
77	888.0	830.3	784.4	748.5	987.6	927.8
78	896.0	780.6	879.6	792.7	974.1	857.7
79	968.7	841.9	832.7	919.6	941.2	984.4
80	918.9	807.8	880.1	813.7	1030.1	922.2
81	928.4	836.5	819.3	815.6	1028.1	885.1
82	937.0	774.1	915.5	798.8	939.5	930.5
83	1018.7	835.9	908.9	804.6	1065.4	766.4
84	993.5	776.3	786.1	768.5	1054.6	821.7
85	991.1	835.9	879.3	879.1	949.5	953.8
86	992.7	804.0	870.1	776.3	974.6	942.4
87	944.1	848.1	818.5	795.8	928.2	880.4
88	949.1	835.5	927.4	838.1	1011.7	868.1
89	1007.4	841.7	885.9	873.2	998.4	843.4
90	912.5	864.0	947.5	785.3	1023.7	911.3
91	1004.5	867.2	874.9	793.4	951.7	980.4
92	1008.0	786.1	873.7	939.4	947.1	947.8
93	901.2	930.4	911.6	885.2	990.5	902.4
94	954.3	836.5	929.6	916.4	924.3	879.7
95	902.2	939.3	858.1	990.9	1011.2	952.3
96	1042.4	784.3	909.6	722.8	1001.3	865.9

cycle	Cylinder 1	Cylinder 2	Cylinder 3	Cylinder 4	Cylinder 5	Cylinder 6
97	987.6	930.2	863.0	870.8	935.8	905.1
98	864.3	750.1	829.0	721.4	946.3	906.8
99	1027.4	902.1	883.7	899.4	927.7	893.0
100	933.1	824.2	1053.2	874.9	931.4	949.3
101	963.0	860.2	814.9	782.7	1008.7	958.7
102	1007.1	848.4	934.5	799.7	1011.4	961.4
103	964.4	920.8	848.3	827.3	948.3	906.6
104	876.8	809.3	820.5	888.4	968.4	926.8
105	971.9	885.6	797.6	784.4	1005.5	959.4
106	931.9	812.4	792.4	863.5	926.5	914.0
107	917.8	915.6	949.2	749.9	961.1	958.4
108	989.7	922.2	799.3	853.2	912.0	993.5
109	1027.7	821.1	927.2	839.1	982.2	919.4
110	1013.5	793.5	872.7	829.8	970.7	946.3
111	1011.8	831.9	888.6	769.5	961.6	899.2
112	918.2	844.3	918.4	799.5	955.7	907.6
113	942.6	880.5	912.3	743.8	949.5	938.2
114	878.5	767.7	810.2	780.7	977.3	961.7
115	905.6	896.2	758.5	777.0	959.9	916.7
116	984.1	825.9	900.6	863.7	840.5	898.5
117	897.8	828.0	891.5	895.2	963.5	859.2
118	939.2	746.5	930.1	817.8	941.4	915.2
119	920.1	797.7	812.2	817.1	799.0	915.2
120	904.8	799.0	807.8	795.8	1004.0	954.2
121	927.9	759.5	993.4	752.9	900.4	878.0
122	926.6	733.2	847.6	759.7	869.7	828.8
123	901.1	760.9	817.8	767.3	958.1	881.7
124	944.8	744.3	893.7	771.7	937.5	908.8
125	853.4	877.1	805.1	783.4	874.2	833.5
126	904.8	815.3	809.3	740.4	899.2	806.6
127	851.1	871.0	853.7	745.1	916.4	883.1
128	1002.2	789.7	819.5	731.6	943.9	887.1
129	940.8	805.7	834.9	798.8	836.6	807.4
130	876.1	799.9	807.1	717.0	897.5	796.7
131	923.2	757.6	827.8	711.4	880.6	886.4
132	869.9	833.6	806.1	705.5	1070.6	965.1
133	927.0	773.0	785.8	732.9	850.8	884.9
134	929.0	804.7	789.5	782.2	877.1	861.7
135	973.9	792.4	804.4	749.7	939.0	744.9
136	934.0	714.3	789.7	700.4	930.1	931.3
137	927.7	762.3	920.4	798.8	944.6	819.5
138	959.2	799.9	898.9	735.8	939.2	882.7
139	864.1	832.5	923.5	804.6	954.0	891.8
140	904.2	779.5	860.3	758.7	1023.7	859.0
141	953.9	807.3	754.3	700.4	960.6	837.7
142	909.3	839.2	878.4	853.5	987.8	933.8
143	993.6	960.0	690.6	774.4	1052.9	944.1
144	898.8	863.5	779.0	702.1	945.1	885.6
145	846.0	900.1	772.6	744.3	962.3	967.3
146	894.3	791.9	819.8	780.2	985.9	944.9
147	954.3	847.6	867.9	705.0	1043.8	874.0
148	926.7	887.1	914.3	911.6	963.3	890.6
149	887.1	886.5	949.9	769.2	1004.3	882.4
150	972.0	824.7	823.4	801.5	1009.4	861.7
151	974.5	939.1	963.8	785.1	1001.8	861.4
152	980.2	994.3	728.5	842.7	953.2	933.5
153	968.7	815.7	937.4	858.1	967.7	963.4
154	1024.4	802.7	800.2	854.4	968.9	862.4

cycle	Cylinder 1	Cylinder 2	Cylinder 3	Cylinder 4	Cylinder 5	Cylinder 6
155	959.6	866.3	852.5	790.2	1041.1	949.8
156	878.4	836.5	824.2	682.6	967.0	889.3
157	894.4	869.7	830.3	792.2	999.6	874.8
158	1030.6	897.7	888.9	810.5	989.8	955.5
159	921.2	858.1	865.4	737.7	931.1	987.8
160	923.7	776.9	817.8	851.5	899.0	1030.0
161	870.3	776.1	1001.7	694.3	1017.3	900.7
162	953.2	901.4	852.7	801.7	1045.5	956.2
163	908.6	799.4	937.4	876.9	860.4	955.0
164	919.0	865.2	893.7	741.9	1021.2	919.9
165	852.9	862.6	853.7	873.0	1004.5	922.2
166	921.4	804.2	873.2	833.4	998.9	869.3
167	1001.7	918.7	872.5	750.7	1029.8	977.7
168	999.2	795.5	868.8	765.6	976.1	989.5
169	964.6	857.3	871.5	770.7	945.4	926.6
170	1041.2	776.4	938.4	829.5	1042.6	885.6
171	945.3	860.6	949.4	800.2	994.5	1006.3
172	900.9	826.1	817.1	779.2	968.4	781.7
173	942.6	865.9	866.6	806.3	902.4	931.3
174	846.4	796.4	898.9	783.4	1009.9	906.1
175	921.7	925.1	801.0	836.1	954.2	906.1
176	963.9	792.8	907.4	733.3	985.9	994.0
177	988.0	826.9	1002.1	843.2	1056.8	971.3
178	894.8	893.5	966.3	843.2	922.3	913.3
179	905.3	875.9	916.4	784.6	957.9	900.4
180	957.2	845.4	908.9	890.6	949.0	933.0
181	999.6	878.0	779.7	802.2	977.3	868.3
182	882.0	881.9	805.1	757.5	948.8	1001.4
183	887.1	861.0	943.1	790.0	983.9	836.7
184	919.0	796.3	901.6	812.0	914.7	896.5
185	929.7	716.2	875.7	817.3	842.5	897.5
186	893.2	773.6	827.8	789.7	958.4	889.8
187	933.3	787.7	925.0	744.8	881.3	972.8
188	927.5	863.9	895.9	787.5	902.2	882.7
189	983.1	836.9	802.2	730.4	940.9	876.0
190	953.5	832.5	920.6	909.9	997.2	966.8
191	912.8	788.9	704.0	737.7	958.9	829.8
192	862.3	831.4	793.4	707.7	880.1	918.7
193	874.9	755.2	802.9	717.0	920.8	852.5
194	975.2	753.1	786.1	713.6	965.7	830.3
195	863.3	813.1	825.6	807.8	888.9	787.4
196	849.4	853.5	833.7	743.1	938.5	963.4
197	841.3	856.0	798.8	736.5	954.0	835.3
198	937.6	750.7	886.7	767.8	896.8	840.7
199	900.4	796.4	853.0	770.0	903.6	860.7
200	880.7	779.8	843.9	845.9	864.6	903.4
201	911.3	766.2	821.2	783.4	883.3	820.0
202	849.2	739.8	818.8	813.7	910.7	897.7
203	956.9	780.6	720.9	780.2	924.7	872.0
204	859.9	831.1	875.9	708.4	907.8	880.4
205	992.7	772.6	851.3	759.0	968.0	857.5
206	838.2	732.6	948.2	732.9	942.4	855.5
207	985.1	785.7	767.0	806.6	988.1	834.5
208	994.5	841.0	932.8	763.6	973.1	884.6
209	876.6	755.3	835.4	701.1	1001.3	823.2
210	840.3	807.6	870.3	780.0	935.3	855.0
211	960.5	939.1	807.3	831.5	928.4	882.9
212	959.9	851.9	761.2	710.1	1039.6	838.7

cycle	Cylinder 1	Cylinder 2	Cylinder 3	Cylinder 4	Cylinder 5	Cylinder 6
213	941.0	796.1	843.4	739.7	964.3	792.8
214	815.4	941.8	739.7	731.1	864.3	874.0
215	1020.8	780.9	841.3	782.4	995.2	902.2
216	953.5	915.8	809.0	853.2	949.3	819.0
217	937.4	810.1	885.2	822.5	1006.0	938.7
218	940.0	936.0	863.0	870.8	1022.9	949.1
219	928.4	795.9	973.1	751.4	1039.9	945.6
220	926.0	883.7	864.9	772.4	941.9	903.1
221	893.8	922.9	961.4	761.4	936.3	890.3
222	995.9	815.7	868.8	792.2	1050.4	926.4
223	923.2	786.4	937.2	785.6	999.6	987.6
224	961.8	786.4	895.9	835.4	1106.4	955.2
225	910.6	864.0	806.6	856.9	1045.3	882.7
226	901.8	829.0	904.7	733.6	1031.8	938.4
227	970.2	746.4	871.5	911.6	1021.0	935.0
228	931.2	882.3	865.7	769.7	991.3	960.9
229	936.1	928.1	898.1	853.0	1021.0	841.9
230	977.3	768.6	811.2	812.9	987.8	1009.8
231	1061.9	886.5	966.7	846.4	995.5	985.1
232	903.7	917.0	905.7	864.7	950.8	997.2
233	988.8	805.2	902.5	756.0	1028.1	962.9
234	954.8	838.4	1001.7	837.6	1053.6	901.9
235	971.9	970.0	879.6	769.0	1055.8	960.7
236	920.1	855.6	872.5	733.6	977.3	930.8
237	953.6	885.9	960.9	811.5	1005.0	918.2
238	1010.4	764.1	814.6	791.4	1002.1	958.9
239	973.6	873.5	835.9	798.8	1013.1	979.4
240	966.4	849.2	856.6	810.2	971.1	881.7
241	991.0	830.5	828.1	723.3	975.8	932.5
242	899.1	788.6	826.4	686.7	944.4	874.8
243	962.1	821.4	755.6	738.0	897.5	880.9
244	1013.3	866.1	851.0	721.4	981.0	940.4
245	1007.5	795.2	870.3	735.8	1111.1	955.0
246	958.6	873.6	822.9	867.6	886.0	902.9
247	888.4	837.2	853.7	745.1	903.9	983.9
248	1008.0	858.6	853.0	832.5	975.1	935.0
249	968.2	773.1	849.6	724.3	976.8	887.6
250	994.2	814.0	927.2	741.6	953.7	920.4
251	886.6	800.9	874.9	803.9	895.3	946.1
252	923.6	844.0	810.5	788.5	901.7	850.1
253	932.9	845.7	880.3	748.0	881.3	906.4
254	882.8	825.2	845.6	802.2	951.0	910.3
255	921.9	836.7	889.3	755.6	920.8	797.2
256	929.4	776.6	901.8	812.9	951.7	919.2
257	847.0	780.3	885.7	795.1	928.9	847.8
258	911.6	797.0	878.6	751.2	931.9	885.6
259	893.5	786.1	1000.7	802.9	906.6	781.9
260	846.4	826.9	781.7	746.0	969.2	832.8
261	872.3	789.0	813.2	728.5	877.4	777.2
262	903.8	845.6	809.5	824.9	924.7	801.4
263	884.8	813.9	949.2	740.4	923.3	835.5
264	815.7	739.4	774.4	734.1	852.8	839.7
265	882.4	776.3	811.7	731.9	948.8	929.3
266	932.9	803.6	869.3	768.3	950.8	794.8
267	826.9	832.7	797.3	738.0	926.7	875.7
268	929.0	830.6	679.1	771.2	946.1	876.0
269	883.3	723.3	964.1	801.7	953.7	889.6
270	911.7	772.2	770.0	771.2	918.4	801.9

cycle	Cylinder 1	Cylinder 2	Cylinder 3	Cylinder 4	Cylinder 5	Cylinder 6
271	915.4	848.0	817.1	774.1	879.8	879.4
272	897.8	853.1	853.5	716.0	996.4	832.0
273	956.0	754.1	839.3	743.1	1000.1	912.0
274	934.8	850.0	868.1	748.2	1007.0	905.9
275	963.7	854.4	944.0	833.7	910.3	843.6
276	916.4	849.3	774.1	803.4	1011.9	917.2
277	948.0	675.3	786.1	791.7	949.5	855.5
278	907.0	818.2	809.0	742.4	935.1	928.3
279	882.2	837.2	963.3	784.9	965.0	930.1
280	884.3	863.5	893.0	704.8	1014.1	928.6
281	858.1	806.5	912.1	805.9	1017.1	908.3
282	963.8	903.4	765.8	813.2	930.9	794.5
283	914.3	769.8	832.7	761.2	955.9	927.1
284	929.4	816.4	830.5	862.7	919.6	827.4
285	921.7	811.8	812.0	799.0	1002.1	836.2
286	930.9	866.1	919.1	751.2	944.1	953.8
287	911.9	782.7	866.6	811.5	1009.4	823.2
288	970.2	811.7	820.0	852.2	974.1	895.7
289	896.9	839.4	810.5	893.0	974.8	886.9
290	898.3	840.5	775.3	848.1	986.9	849.3
291	981.9	852.6	875.7	871.0	1097.6	937.5
292	938.1	789.9	857.1	806.3	1003.8	857.7
293	983.6	909.2	860.3	769.7	993.7	996.5
294	1054.6	900.0	989.2	789.5	982.7	941.4
295	938.7	910.4	1023.6	761.7	1016.3	909.3
296	958.5	786.0	803.2	829.8	920.6	922.4
297	1010.6	933.9	883.2	883.5	968.4	915.0
298	947.1	779.7	912.3	677.4	1013.4	853.5
299	972.3	782.6	972.1	890.6	973.1	896.5
300	986.4	907.2	880.8	822.2	928.7	950.5
301	965.0	896.3	788.3	905.0	1020.5	919.4
302	973.6	896.9	816.1	769.5	914.2	831.8
303	911.9	855.6	814.4	760.4	961.6	886.9
304	944.5	729.5	954.8	826.6	999.4	959.4
305	962.7	915.6	1020.7	900.1	1022.5	838.7
306	932.3	857.6	928.9	859.1	998.9	952.8
307	928.0	901.3	812.7	874.7	1024.9	891.3
308	950.3	771.9	868.8	794.9	999.1	847.4
309	907.7	896.4	870.1	835.1	958.6	871.8
310	915.2	848.1	876.4	721.9	949.8	877.7
311	1000.9	821.0	833.9	763.9	947.1	933.5
312	983.8	875.9	857.9	867.6	995.0	961.9
313	1010.9	826.9	746.0	735.3	954.4	849.3
314	954.0	910.6	862.7	755.8	925.2	825.6
315	899.5	872.7	906.4	796.1	936.5	787.6
316	949.6	767.3	920.6	787.1	942.9	940.4
317	857.8	836.1	894.0	787.3	922.0	828.8
318	946.6	838.2	969.7	805.6	1016.6	937.2
319	913.0	780.1	857.6	757.3	955.7	896.7
320	922.0	811.8	799.0	886.2	880.1	883.9
321	973.2	895.6	890.8	759.2	1015.3	778.5
322	939.6	733.9	819.0	813.4	922.0	950.5
323	911.5	899.4	798.5	851.8	958.4	808.6
324	957.0	708.2	884.7	818.3	1007.0	900.4
325	897.8	830.5	926.2	898.4	919.8	816.5
326	839.7	811.8	960.4	777.8	916.6	855.0
327	935.9	866.9	847.6	731.4	949.0	899.2
328	844.6	881.4	906.9	746.0	985.1	861.7

cycle	Cylinder 1	Cylinder 2	Cylinder 3	Cylinder 4	Cylinder 5	Cylinder 6
329	951.4	794.3	903.3	706.5	967.7	852.5
330	892.2	818.1	930.6	782.4	921.6	869.8
331	867.1	733.0	885.7	729.9	884.5	861.2
332	912.5	736.0	770.0	718.4	916.4	945.6
333	993.6	800.9	807.3	714.1	917.9	734.8
334	929.6	871.3	842.0	788.3	946.3	924.4
335	949.6	784.7	848.6	731.9	913.2	961.9
336	981.2	728.5	698.9	824.2	869.3	840.4
337	912.9	812.4	901.3	785.3	945.6	897.0
338	947.3	849.8	719.4	781.9	859.7	799.2
339	945.4	857.5	906.9	701.1	922.5	871.3
340	909.8	728.2	830.3	805.9	986.4	822.7
341	852.4	774.7	774.6	776.6	854.8	825.1
342	915.0	723.2	786.3	766.5	891.8	877.2
343	952.1	852.7	744.8	726.8	953.7	874.0
344	933.2	778.9	827.1	706.7	905.3	840.2
345	859.4	673.7	882.5	760.4	1015.3	929.3
346	962.9	903.0	813.4	777.0	917.9	889.6
347	896.6	786.4	911.6	772.2	902.4	844.4
348	965.7	731.0	825.6	798.5	945.4	873.5
349	941.4	680.6	744.6	833.2	1002.8	838.2
350	942.8	879.4	742.6	796.6	1056.3	810.8
351	888.3	797.8	715.5	868.4	937.0	882.2
352	1000.2	869.3	780.5	847.8	935.5	827.4
353	894.3	878.3	850.5	742.6	1010.7	924.9
354	970.6	866.5	922.1	829.3	1023.9	847.6
355	932.9	858.6	942.8	925.2	975.8	878.0
356	942.4	958.0	896.9	861.3	1027.6	970.8
357	894.3	850.5	833.7	877.4	1034.7	924.1
358	972.4	759.3	838.1	774.6	940.7	904.1
359	1003.9	821.4	805.6	855.4	994.0	823.9
360	963.4	820.5	789.0	742.9	948.8	967.1
361	986.7	786.1	933.8	863.0	1020.0	934.7
362	971.2	811.8	870.1	746.5	1041.4	935.0
363	980.6	856.3	890.6	876.4	1060.5	938.7
364	976.2	803.6	876.4	856.6	954.9	869.3
365	913.5	846.3	851.3	754.6	945.1	971.3
366	987.7	815.2	868.4	782.7	1090.7	953.8
367	999.7	801.4	909.1	866.4	961.1	926.8
368	951.2	836.5	956.5	752.9	960.3	883.6
369	932.6	868.8	991.9	885.0	1003.1	909.1
370	999.1	833.2	834.9	843.0	966.2	959.9
371	992.3	849.8	927.2	772.9	968.7	894.0
372	851.3	794.9	885.2	812.2	929.7	941.9
373	922.5	861.5	1017.5	757.5	981.5	952.8
374	894.4	812.8	897.9	858.6	934.8	813.3
375	1024.3	814.0	860.8	838.3	994.2	1054.7
376	903.1	899.4	836.4	900.6	933.1	917.7
377	967.6	780.9	858.1	885.2	936.8	909.3
378	941.0	902.6	823.9	820.3	968.7	896.0
379	870.9	754.7	858.1	872.5	1080.4	887.3
380	957.0	829.6	899.1	886.7	948.8	844.4
381	995.3	857.7	785.8	713.3	1033.5	840.9
382	882.0	786.4	973.1	881.0	1003.1	876.5
383	1008.0	851.5	785.3	704.0	989.1	913.3
384	906.1	933.4	950.6	663.0	995.7	983.1
385	970.6	800.9	932.8	895.0	960.8	897.7
386	919.5	858.1	815.4	760.7	934.1	919.9

cycle	Cylinder 1	Cylinder 2	Cylinder 3	Cylinder 4	Cylinder 5	Cylinder 6
387	1007.5	838.9	981.6	788.0	917.6	968.8
388	888.9	729.7	812.7	859.1	999.1	880.2
389	894.2	870.1	954.3	775.8	973.1	952.8
390	910.3	874.0	839.8	772.4	960.8	911.3
391	943.5	887.5	746.3	802.4	954.9	949.6
392	943.1	767.4	930.1	795.6	861.2	853.5
393	949.0	896.9	785.6	817.6	909.3	922.9
394	883.1	791.3	930.6	775.8	903.1	896.7
395	946.7	791.3	776.1	791.4	932.4	851.8
396	941.9	848.5	771.7	676.7	931.4	869.8
397	903.8	808.8	851.8	754.8	897.0	867.8
398	912.6	797.8	858.8	819.0	912.5	867.8
399	859.0	794.9	846.6	721.1	855.0	835.5
400	865.0	810.9	813.9	760.4	918.6	814.0
401	880.9	761.0	795.4	739.4	930.6	960.7
402	961.6	739.7	782.2	727.7	979.2	878.2
403	855.4	779.8	861.5	731.6	979.5	841.4
404	965.2	753.2	764.8	829.3	964.5	865.1
405	891.4	821.8	866.2	756.5	902.6	831.6
406	886.7	716.6	779.5	732.9	865.3	913.8
407	927.3	735.1	811.2	779.2	847.2	836.2
408	825.9	798.1	829.5	722.6	920.1	869.1
409	995.4	835.9	852.0	762.4	935.5	865.1
410	941.7	859.3	772.9	777.8	961.8	777.2
411	887.3	919.8	905.7	791.0	920.1	872.3
412	835.3	731.9	864.2	777.8	914.2	780.5
413	942.8	845.7	841.5	793.2	897.7	903.1
414	907.3	667.5	790.5	881.8	993.5	831.8
415	928.0	847.6	817.1	674.3	1040.9	853.0
416	944.7	850.6	842.5	671.3	978.0	925.9
417	936.1	749.5	805.1	770.2	925.5	950.5
418	872.8	753.7	821.0	797.3	1049.2	782.9
419	956.2	719.9	827.1	689.2	934.6	870.8
420	1036.6	801.4	868.6	771.2	934.3	938.4
421	951.3	731.9	734.1	834.4	1030.1	857.7
422	1005.1	785.6	946.5	786.1	979.7	892.3
423	988.3	824.7	880.3	854.2	962.3	904.6
424	990.1	861.1	827.6	748.5	944.4	939.4
425	900.9	826.4	968.7	833.9	1007.0	959.7
426	1000.8	852.2	914.0	754.8	1005.0	860.4
427	867.9	820.1	920.1	835.4	981.5	888.6
428	1004.5	784.4	909.1	778.0	959.6	896.7
429	941.0	853.1	906.2	893.0	997.9	906.6
430	1022.4	955.3	839.8	838.1	958.6	812.8
431	943.9	814.6	882.8	778.8	954.4	905.1
432	988.9	839.0	932.3	862.5	916.9	946.8
433	984.7	839.2	898.9	756.0	985.1	883.9
434	1010.1	928.1	974.3	819.3	1014.4	907.6
435	1011.4	807.1	903.3	894.5	958.9	842.4
436	949.0	811.7	983.6	811.7	1045.8	976.5
437	867.1	813.2	884.0	838.8	906.1	973.3
438	1017.9	888.3	969.2	736.0	921.1	899.7
439	1020.9	784.8	916.2	915.0	1037.9	881.7
440	967.2	968.9	958.2	875.2	898.5	924.1
441	968.6	814.8	853.0	862.2	1013.9	1010.0
442	991.3	861.1	820.0	859.3	1015.6	957.0
443	977.2	903.1	797.1	840.8	960.6	918.5
444	924.0	747.6	968.2	859.8	942.9	921.7

cycle	Cylinder 1	Cylinder 2	Cylinder 3	Cylinder 4	Cylinder 5	Cylinder 6
445	917.5	809.8	872.3	796.3	864.6	1045.6
446	944.4	848.8	897.6	844.2	1017.1	988.1
447	1039.3	906.2	969.2	833.0	939.2	862.4
448	964.6	861.3	857.1	811.0	958.9	919.9
449	907.0	807.8	824.7	863.5	998.2	845.1
450	935.2	752.3	909.9	879.6	938.2	945.1
451	948.2	933.5	935.5	836.4	948.1	893.3
452	1004.3	852.5	963.6	722.1	966.2	918.5
453	970.4	768.6	920.8	750.2	968.0	909.1
454	857.6	877.9	975.3	716.0	923.5	831.8
455	921.5	779.1	985.1	801.9	939.0	907.1
456	959.5	855.2	796.1	812.2	935.8	903.9
457	831.0	790.5	955.3	799.3	989.6	941.7
458	986.7	789.4	884.2	767.8	818.7	889.3
459	929.2	776.8	846.6	823.2	890.4	918.2
460	921.4	767.6	903.5	761.2	940.9	902.7
461	923.7	775.3	745.1	813.9	871.0	814.0
462	906.9	752.7	832.7	782.9	890.4	862.7
463	917.5	819.8	926.2	782.4	945.6	874.5
464	948.2	690.7	802.9	867.4	994.5	883.1
465	926.8	838.0	843.4	734.3	858.0	813.3
466	809.2	733.9	785.6	789.5	940.2	718.0
467	934.1	855.0	848.8	846.9	912.5	890.6
468	907.4	801.5	749.5	794.1	872.9	906.1
469	843.0	769.9	823.2	772.4	852.3	858.2
470	944.0	836.5	820.3	762.6	882.5	835.5
471	941.0	866.7	779.2	694.8	986.6	859.9
472	986.6	772.6	918.6	784.9	890.6	749.3
473	884.7	782.3	936.0	805.1	883.3	849.1
474	895.3	667.5	843.9	785.1	1022.5	824.6
475	913.9	805.1	806.8	838.3	953.5	856.0
476	878.0	926.3	788.5	747.5	1015.3	871.8
477	825.7	891.5	825.6	811.7	950.8	878.2
478	827.8	802.0	919.4	889.6	983.2	821.7
479	918.4	781.3	752.4	742.9	927.2	817.2
480	907.8	837.6	926.5	741.9	917.9	824.6
481	943.9	792.7	880.3	839.3	1034.7	785.4
482	903.0	906.4	857.1	787.1	869.7	839.5
483	891.7	780.1	830.3	810.7	940.9	892.0
484	868.4	862.7	794.4	821.2	912.2	829.3
485	878.5	717.7	823.4	765.6	907.1	898.0
486	956.0	801.5	839.1	738.2	891.6	893.5
487	851.1	783.6	915.2	789.7	965.3	845.4
488	1046.1	791.7	814.6	819.3	1057.3	927.1
489	977.8	819.2	783.1	804.4	1049.2	900.4
490	839.1	821.0	831.7	751.7	974.1	885.4
491	968.9	749.0	768.0	771.9	1004.5	889.1
492	945.4	882.6	905.5	793.9	980.0	857.2
493	955.8	873.3	846.1	803.2	1000.1	867.3
494	968.1	860.5	966.3	763.1	912.2	929.3
495	967.2	800.9	823.2	869.8	1047.3	965.6
496	852.8	884.3	906.7	814.2	1055.6	933.5
497	1026.5	859.6	809.5	864.2	1050.9	842.4
498	954.9	911.7	971.1	838.6	949.5	984.9
499	908.1	913.8	929.9	813.4	997.9	938.4
500	958.6	893.5	933.3	862.7	1006.7	895.2
501	942.8	781.8	910.3	746.8	1113.5	890.8
502	830.0	887.9	855.2	933.3	943.6	851.1

cycle	Cylinder 1	Cylinder 2	Cylinder 3	Cylinder 4	Cylinder 5	Cylinder 6
503	1037.7	839.7	1010.0	811.2	1020.7	926.4
504	962.9	823.8	995.8	921.3	951.7	961.2
505	951.6	900.0	869.1	744.8	979.0	868.8
506	988.7	831.0	926.2	807.3	966.5	936.7
507	931.0	727.7	811.7	832.0	1011.9	940.2
508	1040.5	866.9	927.7	984.8	925.7	1001.9
509	905.9	920.5	911.1	731.4	1071.1	936.2
510	1034.6	824.7	911.3	941.4	1000.6	895.2
511	966.9	820.6	909.9	765.6	915.7	941.2
512	994.1	934.9	897.2	891.8	983.4	840.7
513	914.5	819.2	874.0	787.1	995.7	889.6
514	992.4	862.2	917.4	763.9	931.6	962.9
515	959.6	907.6	824.4	736.8	974.8	844.9
516	966.1	815.2	862.7	826.4	951.5	785.4
517	921.7	811.7	969.2	802.9	900.9	869.8
518	951.9	868.6	810.2	863.0	900.2	889.6
519	951.2	838.9	870.1	836.1	1023.4	862.4
520	925.4	796.7	769.7	835.9	892.1	837.7
521	895.1	775.3	847.6	661.1	932.8	915.5
522	932.6	822.2	862.0	801.0	914.7	848.8
523	937.5	773.0	852.2	731.1	971.6	818.5
524	908.9	815.1	934.5	802.2	969.4	867.8
525	956.4	817.6	806.3	762.9	982.9	897.2
526	934.1	826.5	907.2	843.2	978.3	896.2
527	915.2	829.3	816.4	777.5	927.9	884.4
528	894.9	867.1	761.2	792.4	1004.0	904.1
529	984.7	837.1	794.1	808.8	911.5	856.7
530	862.8	760.5	790.7	812.2	950.8	903.4
531	917.2	815.6	687.2	731.9	914.9	774.8
532	973.2	832.2	790.2	944.8	886.0	866.9
533	980.8	817.3	818.3	760.4	1055.6	854.8
534	873.6	716.8	853.0	689.6	954.2	819.7
535	892.7	820.1	821.7	815.1	910.3	814.3
536	908.1	708.2	846.9	793.9	874.7	884.4
537	937.6	886.9	892.0	711.6	926.7	903.9
538	818.8	801.4	839.1	835.4	871.2	891.8
539	907.4	799.7	899.1	721.4	969.2	860.2
540	987.7	828.2	860.8	785.8	956.9	786.6
541	900.0	760.9	749.0	829.5	925.2	885.6
542	893.9	814.9	756.5	705.0	949.5	954.7
543	926.0	726.5	865.7	730.2	918.9	958.4
544	920.4	767.8	834.4	744.6	914.4	872.0
545	872.3	731.9	784.4	781.7	928.2	809.6
546	929.0	810.1	766.8	796.1	983.4	859.4
547	909.4	838.0	930.9	712.3	830.2	917.0
548	891.0	696.2	766.3	721.1	858.2	954.0
549	843.1	768.8	767.3	795.4	988.8	944.4
550	913.8	768.0	853.5	831.7	998.4	920.4
551	991.0	790.3	876.9	798.8	969.9	868.3
552	866.8	845.4	816.4	886.4	928.4	955.7
553	927.2	814.7	813.2	912.1	922.8	911.0
554	902.5	721.2	850.0	703.1	962.1	873.5
555	913.9	789.4	837.6	889.1	954.4	802.7
556	941.4	824.8	1011.4	831.5	1063.7	977.7
557	898.3	770.7	792.2	794.6	992.5	904.9
558	876.4	826.1	809.0	830.3	949.5	950.5
559	975.0	920.2	821.7	784.4	993.2	947.1
560	978.5	951.8	897.4	685.0	1014.8	910.6

cycle	Cylinder 1	Cylinder 2	Cylinder 3	Cylinder 4	Cylinder 5	Cylinder 6
561	984.6	795.5	868.1	763.6	1042.3	880.2
562	868.5	918.0	813.9	802.2	970.9	830.3
563	975.9	844.3	883.2	648.4	995.9	929.1
564	985.4	866.7	923.3	841.5	976.8	877.5
565	1009.5	764.5	738.5	837.1	1057.3	897.5
566	990.5	951.4	932.3	905.5	976.8	948.1
567	866.2	921.7	918.2	776.6	900.4	955.0
568	901.2	816.4	792.2	781.2	1019.5	871.1
569	979.7	915.6	898.6	727.0	902.4	847.4
570	962.4	779.0	864.4	796.1	1069.3	899.2
571	850.3	776.0	900.3	782.9	895.8	930.1
572	939.3	840.5	965.8	835.9	950.5	924.6
573	1017.8	932.1	859.6	813.4	1005.0	788.4
574	944.5	895.4	851.3	813.9	1004.3	914.7
575	919.5	865.4	852.0	873.0	1003.1	844.4
576	925.4	827.1	889.3	838.6	879.6	962.6
577	964.6	817.2	964.1	853.2	944.1	983.6
578	989.4	913.4	905.2	810.0	957.2	892.0
579	857.3	877.2	893.3	835.9	994.7	847.4
580	966.1	822.7	1017.0	812.0	969.4	988.6
581	965.1	839.6	928.4	822.5	997.9	914.0
582	1024.4	854.0	883.2	830.3	1042.8	897.0
583	1043.8	848.6	859.6	890.3	905.8	808.3
584	994.4	758.0	976.5	843.2	938.7	898.9
585	996.6	860.9	963.1	701.6	1007.7	974.5
586	896.4	820.5	920.8	888.9	921.6	907.3
587	957.3	811.5	958.0	831.5	993.2	924.4
588	891.4	820.6	850.5	713.6	1056.8	982.1
589	912.8	975.9	902.8	756.0	963.8	946.1
590	956.6	912.1	918.9	731.4	886.2	920.2
591	983.8	855.9	885.4	893.0	955.9	880.4
592	920.1	729.0	829.0	759.7	948.8	859.9
593	960.9	777.4	824.9	779.7	878.1	890.8
594	981.0	780.1	930.6	829.0	906.3	815.5
595	949.9	766.1	867.6	844.7	907.3	890.1
596	956.4	791.0	781.7	762.4	968.9	964.6
597	919.7	823.5	828.3	717.7	1001.6	888.6
598	861.2	837.3	802.9	750.9	864.6	822.2
599	873.5	847.2	780.0	883.7	899.2	863.6
600	979.0	752.8	929.4	811.7	902.6	862.9
601	945.7	804.4	846.6	805.9	859.9	882.4
602	883.5	654.5	868.1	656.4	984.6	880.2
603	922.9	757.0	836.9	753.6	979.7	761.7
604	925.9	774.1	849.1	843.7	869.7	893.5
605	909.8	749.0	741.4	763.6	955.2	846.1
606	907.3	796.3	898.4	813.9	974.1	891.5
607	938.1	861.1	825.1	791.7	953.5	846.6
608	870.5	795.9	834.4	809.3	899.5	826.6
609	901.4	790.5	847.4	681.1	846.2	888.8
610	920.2	758.5	787.5	764.6	914.2	872.8
611	904.7	832.3	863.2	823.4	938.2	848.6
612	944.0	764.1	688.7	728.5	909.3	946.8
613	937.5	858.5	789.3	785.1	906.1	935.5
614	911.9	737.8	831.5	785.8	921.8	827.9
615	900.4	852.1	864.4	761.7	927.7	842.4
616	942.4	764.0	863.2	806.8	937.3	907.3
617	892.2	895.1	907.2	787.8	893.6	796.0
618	889.3	862.7	876.7	825.4	985.6	851.1

cycle	Cylinder 1	Cylinder 2	Cylinder 3	Cylinder 4	Cylinder 5	Cylinder 6
619	951.7	812.3	883.2	773.6	921.6	994.0
620	830.1	861.7	876.7	698.9	989.8	863.4
621	974.3	845.7	848.3	786.3	1000.1	913.3
622	918.6	771.4	947.7	831.5	967.2	874.8
623	910.0	778.1	808.3	722.8	920.3	1016.0
624	1005.1	907.3	801.2	877.1	922.8	899.2
625	940.1	795.7	836.9	803.2	933.6	868.8
626	923.6	858.6	824.7	853.5	960.1	881.9
627	945.6	796.1	822.2	825.1	964.3	895.2
628	919.1	821.8	871.0	790.5	975.3	852.3
629	935.8	785.7	788.3	797.8	977.0	939.9
630	866.8	743.1	938.7	734.8	965.7	928.8
631	804.5	854.3	888.9	750.4	1020.7	941.7
632	914.6	883.8	861.5	786.6	1005.3	905.1
633	875.4	851.8	960.1	705.5	1021.5	856.0
634	871.1	800.6	833.9	757.5	958.4	913.0
635	954.7	873.9	840.0	878.6	992.0	823.4
636	945.8	739.9	990.4	921.3	1052.4	894.0
637	939.6	777.6	881.3	825.9	1002.1	770.6
638	866.9	920.0	941.6	921.8	978.8	909.8
639	899.7	797.8	947.7	752.9	952.7	924.9
640	865.1	821.8	771.4	808.0	963.5	920.4
641	925.3	865.2	793.9	803.9	1002.8	874.3
642	960.7	810.6	892.5	808.3	966.0	979.2
643	923.0	773.5	922.8	753.6	950.3	908.6
644	931.4	864.2	834.9	860.5	962.3	983.4
645	928.8	973.3	932.3	789.3	1046.8	928.8
646	961.8	906.3	946.7	881.8	1047.5	924.9
647	1009.1	850.2	903.0	704.8	1007.0	967.6
648	960.3	830.7	893.0	918.9	1066.2	937.0
649	925.8	859.7	957.5	906.9	992.5	951.5
650	888.2	910.2	778.5	765.6	1062.0	866.4
651	892.9	867.2	807.8	860.3	873.2	904.9
652	953.9	863.6	831.7	760.7	1034.5	910.3
653	951.4	857.5	827.6	883.0	940.9	911.8
654	1042.9	865.9	905.5	874.0	936.0	844.9
655	1055.3	830.7	866.4	771.2	1097.6	940.7
656	860.2	880.8	923.0	822.2	1000.1	945.6
657	1011.4	845.9	813.4	792.2	1036.9	934.5
658	948.8	759.0	862.5	833.7	1047.5	956.7
659	971.1	872.5	958.4	833.7	956.2	831.8
660	936.6	966.3	978.0	764.8	918.6	873.0
661	901.1	826.1	959.7	824.4	952.2	936.0
662	915.2	843.2	845.4	829.8	876.9	908.1
663	956.0	836.4	932.8	892.5	912.5	854.5
664	920.1	826.0	866.4	798.8	982.4	939.7
665	908.5	826.3	956.0	802.7	946.1	965.1
666	998.3	851.8	824.4	757.8	903.6	885.4
667	963.3	733.7	871.0	883.7	938.5	922.6
668	947.0	802.4	840.8	759.0	954.9	871.8
669	935.8	784.0	835.9	823.9	852.3	812.5
670	1009.5	842.2	785.3	835.9	860.7	740.5
671	904.6	789.4	742.1	798.3	848.6	911.8
672	956.4	808.6	859.8	793.2	885.7	896.7
673	958.6	777.0	902.5	717.5	898.7	818.5
674	909.9	799.8	817.1	830.3	850.1	847.8
675	848.5	804.7	822.5	766.3	891.1	859.0
676	803.2	849.3	893.0	700.9	920.3	792.5

cycle	Cylinder 1	Cylinder 2	Cylinder 3	Cylinder 4	Cylinder 5	Cylinder 6
677	913.7	737.6	874.7	672.1	1032.8	737.7
678	947.5	867.7	769.2	781.7	964.5	837.2
679	973.2	755.7	785.8	664.5	921.1	825.4
680	872.5	878.7	762.2	715.0	999.4	765.6
681	947.5	856.1	871.0	715.8	956.2	725.6
682	951.8	739.9	876.2	622.0	899.0	789.1
683	894.5	740.3	872.5	755.6	944.1	794.3
684	853.9	803.8	746.8	779.7	961.6	880.7
685	910.7	786.5	823.4	758.7	949.5	836.7
686	870.7	802.7	757.0	802.2	1014.4	888.3
687	875.5	971.7	903.3	832.0	975.6	790.1
688	875.5	859.2	776.8	815.1	899.7	804.2
689	932.2	858.1	786.1	786.8	926.7	929.1
690	958.6	786.4	806.6	727.7	979.7	841.2
691	868.2	855.6	841.5	749.7	924.3	886.4
692	935.5	815.5	898.9	814.6	955.9	905.1
693	871.2	832.3	915.7	771.7	936.5	929.1
694	957.8	834.2	891.5	867.9	980.0	882.9
695	895.8	842.2	837.6	741.2	908.0	905.6
696	812.0	786.7	922.8	896.7	956.9	884.6
697	877.6	793.5	892.3	802.9	998.2	863.6
698	1004.9	893.4	919.9	738.7	981.5	994.5
699	984.7	907.7	1008.2	814.2	990.0	912.3
700	970.9	780.6	734.8	736.0	946.3	929.3
701	874.6	882.5	867.1	741.6	1007.2	848.8
702	978.6	943.0	942.1	871.5	1023.2	884.9
703	896.9	868.3	816.6	803.2	973.6	912.5
704	928.5	756.0	698.4	714.3	1063.2	896.2
705	966.9	910.4	841.5	870.1	974.1	832.8
706	965.5	802.4	963.8	862.7	1006.5	934.7
707	860.8	860.8	872.7	879.1	943.6	957.0
708	1008.0	907.5	791.7	876.9	1063.7	1019.4
709	1027.3	848.5	954.3	824.2	958.1	846.9
710	976.2	831.9	967.0	763.4	1077.2	890.1
711	1002.3	741.5	803.4	803.9	1076.2	881.7
712	967.3	864.2	896.9	786.8	949.8	842.7
713	875.7	898.4	813.9	764.3	998.9	965.6
714	955.2	886.9	924.5	794.6	939.7	999.2
715	1029.3	851.8	887.2	838.3	934.6	813.5
716	925.1	786.0	836.4	847.1	977.8	882.9
717	947.4	875.8	987.2	712.6	960.1	976.5
718	1028.1	820.7	924.0	931.3	1007.5	972.3
719	868.9	862.1	876.7	867.4	968.4	875.7
720	1008.7	803.0	920.4	910.8	927.4	941.9
721	989.7	814.9	962.1	800.2	981.9	949.6
722	1013.3	848.9	899.4	774.1	971.4	842.7
723	993.9	850.6	855.4	791.9	991.5	863.4
724	1019.0	763.5	781.7	704.8	923.5	872.5
725	947.6	905.0	902.3	751.4	964.0	951.3
726	1004.9	825.1	913.8	786.8	1025.6	904.1
727	989.0	849.7	784.4	776.8	940.0	858.7
728	990.6	913.9	860.1	856.6	939.2	895.2
729	940.1	857.2	962.6	844.4	848.4	934.7
730	941.4	878.5	781.9	775.3	1014.8	821.2
731	1001.4	877.5	783.6	785.8	990.5	843.6
732	936.7	838.2	828.6	760.9	930.1	802.2
733	959.6	700.0	821.5	807.3	908.8	865.6
734	944.5	877.6	856.1	785.8	872.4	867.8

cycle	Cylinder 1	Cylinder 2	Cylinder 3	Cylinder 4	Cylinder 5	Cylinder 6
735	912.8	810.5	904.0	818.8	880.1	840.2
736	935.5	761.9	854.7	768.5	981.9	800.9
737	907.0	830.7	821.2	759.5	915.9	846.1
738	931.0	892.1	892.0	796.8	953.5	880.7
739	941.8	781.0	780.5	743.1	1022.7	902.7
740	930.5	821.5	818.8	835.4	926.5	954.7
741	882.7	826.1	752.4	818.5	909.5	913.8
742	900.5	817.8	811.0	818.8	881.5	820.0
743	919.0	773.2	763.1	756.0	896.3	883.6
744	883.3	794.5	908.4	736.0	851.3	786.4
745	930.3	718.9	799.0	770.0	879.6	873.0
746	900.9	783.5	807.1	742.1	899.9	860.4
747	941.0	812.2	899.4	698.4	924.0	936.7
748	941.0	840.9	899.6	767.0	861.4	851.3
749	891.8	825.3	804.1	694.3	941.9	716.8
750	950.9	699.8	707.7	688.7	879.8	785.9
751	847.9	646.5	830.0	782.2	977.5	837.7
752	958.2	829.8	861.0	745.5	906.3	867.6
753	888.0	850.7	822.2	766.3	873.9	921.4
754	948.6	858.1	929.4	749.5	934.6	840.9
755	948.8	807.8	939.6	793.9	878.6	841.4
756	962.2	910.2	873.0	777.0	912.5	882.4
757	897.8	845.7	893.7	747.5	920.6	891.3
758	943.5	901.8	952.3	839.5	987.6	848.8
759	852.9	867.7	816.8	859.8	1017.5	936.7
760	893.6	779.5	923.0	733.8	945.9	835.5
761	869.8	842.3	939.2	735.8	849.6	844.9
762	915.0	841.0	812.4	793.4	947.8	881.2
763	903.7	773.5	936.7	837.3	951.3	833.8
764	881.3	821.4	812.7	825.1	1028.1	898.7
765	824.6	862.5	855.4	779.7	999.6	835.0
766	918.5	769.3	903.0	779.2	1035.0	989.3
767	964.2	854.7	903.3	853.9	960.8	750.1
768	879.3	856.7	885.9	845.2	900.2	863.6
769	958.1	846.4	840.0	858.6	1073.5	817.5
770	916.9	863.0	857.9	773.9	1048.7	804.2
771	907.0	838.0	908.9	826.6	1002.8	946.1
772	923.8	890.1	844.4	906.4	982.7	925.4
773	949.5	813.4	918.6	819.5	963.8	881.9
774	970.8	822.1	790.5	822.2	933.1	896.0
775	936.6	855.9	817.6	900.6	870.0	910.8
776	942.6	786.3	928.2	748.0	1058.3	813.5
777	1034.6	880.1	958.2	785.8	1049.7	905.1
778	1003.0	879.2	868.6	822.7	919.1	920.2
779	871.8	776.0	812.7	866.2	911.2	851.8
780	952.9	872.7	884.2	710.9	992.0	974.0
781	978.6	837.3	926.2	786.3	944.9	973.7
782	989.8	861.5	772.9	749.2	979.7	950.5
783	1015.6	866.5	805.1	793.6	1072.5	884.1
784	926.3	810.2	896.7	897.9	1013.6	972.5
785	940.9	776.4	837.8	730.2	992.5	898.2
786	1020.7	852.6	877.9	804.1	1066.9	933.8
787	1022.8	815.5	861.8	868.8	908.3	965.6
788	1067.0	845.2	848.6	884.2	910.0	858.7
789	957.2	792.6	839.8	746.3	966.5	953.3
790	985.4	821.3	895.2	866.4	893.3	912.8
791	942.8	969.6	995.3	784.6	963.5	991.3
792	977.2	908.4	899.8	905.0	1046.5	925.4

cycle	Cylinder 1	Cylinder 2	Cylinder 3	Cylinder 4	Cylinder 5	Cylinder 6
793	1021.8	879.3	964.5	874.2	937.3	815.5
794	916.5	732.3	858.8	828.3	995.7	1002.6
795	945.8	891.4	819.3	882.0	936.8	840.7
796	885.2	905.0	876.2	747.0	880.8	821.2
797	965.5	808.6	866.6	828.8	1097.1	873.5
798	992.7	819.6	890.1	868.6	894.3	949.3
799	997.0	779.8	856.6	805.6	935.3	894.8
800	931.9	763.9	752.9	815.1	945.9	936.7
801	1015.5	875.2	807.6	728.9	903.1	844.4
802	886.6	806.1	873.2	788.0	923.0	846.1
803	884.7	886.2	900.3	868.8	1015.3	891.5
804	863.3	797.7	838.3	787.5	907.8	898.2
805	850.8	772.8	837.8	742.6	987.8	912.3
806	935.4	884.4	847.8	705.8	922.8	946.6
807	926.2	724.3	821.0	676.5	890.1	946.1
808	1025.7	810.3	878.6	814.4	924.5	815.3
809	856.1	782.7	833.2	782.4	909.0	887.3
810	906.4	870.0	833.4	734.1	968.7	828.6
811	943.7	778.5	868.1	865.7	929.7	915.7
812	917.1	733.5	872.5	763.6	941.9	862.9
813	861.1	668.9	871.5	721.9	950.8	893.5
814	900.7	872.1	679.4	739.4	899.5	904.1
815	897.3	772.6	804.9	728.7	989.3	803.2
816	960.1	752.2	766.8	807.1	948.1	811.3
817	876.3	777.0	807.1	751.4	907.6	879.2
818	858.2	862.1	938.4	833.4	969.4	870.3
819	821.4	728.5	758.5	803.4	976.1	876.2
820	885.3	798.8	880.8	775.1	925.5	868.8
821	938.8	738.7	934.3	837.1	905.6	813.5
822	874.2	834.6	791.7	833.4	966.7	887.3
823	932.4	794.5	785.1	885.0	928.2	845.9
824	940.8	803.1	837.3	771.4	1001.1	872.8
825	951.2	865.5	834.4	777.8	966.7	885.9
826	894.2	806.5	878.4	722.1	925.2	881.2
827	902.1	884.8	834.9	723.1	958.1	854.3
828	948.3	865.2	941.6	671.3	923.5	900.2
829	865.9	837.2	843.4	795.1	937.3	908.6
830	933.6	725.3	801.7	719.4	885.5	913.0
831	903.0	714.7	898.1	847.4	958.6	911.5
832	947.0	839.0	816.1	885.0	898.0	907.3
833	916.8	779.5	745.1	806.6	931.6	928.6
834	892.6	790.2	788.5	792.4	945.6	849.3
835	967.7	790.1	866.2	776.1	934.1	762.2
836	916.1	834.3	879.1	746.3	964.8	833.5
837	950.0	738.6	910.3	802.7	864.8	861.2
838	976.4	801.8	993.4	822.7	1050.2	882.2
839	960.1	876.2	843.9	786.1	1010.2	840.7
840	971.3	747.4	966.0	820.7	977.0	894.5
841	931.4	905.8	871.8	751.9	988.3	924.6
842	960.9	838.4	863.0	942.3	996.9	921.4
843	959.4	768.8	995.1	948.4	1030.6	949.1
844	883.2	783.9	873.5	839.5	994.7	911.0
845	954.2	918.8	904.0	850.5	975.1	958.4
846	980.2	863.5	922.8	888.1	981.7	887.8
847	947.6	838.2	938.7	859.1	974.8	945.6
848	953.1	882.7	936.7	765.3	985.9	934.7
849	956.0	910.6	787.8	851.0	1075.5	808.3
850	891.5	816.8	826.6	751.2	939.5	881.9

cycle	Cylinder 1	Cylinder 2	Cylinder 3	Cylinder 4	Cylinder 5	Cylinder 6
851	992.9	943.5	885.4	806.8	1040.1	887.1
852	875.8	886.3	905.5	841.7	977.3	941.2
853	921.4	892.5	778.8	843.7	979.2	851.8
854	931.9	858.1	901.6	843.2	1029.6	850.6
855	936.5	755.9	1011.9	741.2	982.9	978.4
856	968.9	876.0	869.1	812.9	954.4	915.0
857	1033.8	771.0	847.4	807.3	946.8	932.3
858	959.4	898.9	934.0	830.3	921.3	903.4
859	941.1	793.4	898.4	893.7	983.4	935.5
860	938.7	873.0	918.4	819.8	994.2	907.1
861	956.4	918.5	825.1	794.9	983.2	915.2
862	950.9	695.8	995.3	745.1	895.5	789.8
863	1016.6	834.2	822.2	741.9	988.3	926.4
864	929.7	836.9	847.6	784.1	985.4	876.7
865	932.6	840.6	889.3	849.8	1039.4	945.1
866	930.7	895.9	878.1	796.6	911.2	969.1
867	1018.8	908.3	877.4	874.2	905.6	1012.8
868	961.7	881.9	816.8	819.5	906.3	774.8
869	962.4	719.1	906.2	743.6	954.4	850.6
870	952.2	905.8	851.0	822.2	924.3	873.5
871	911.2	939.5	768.0	747.7	914.4	865.6
872	973.8	895.9	956.2	815.9	944.6	887.8
873	880.7	913.0	925.2	805.4	968.7	965.1
874	959.5	829.0	806.8	777.0	989.6	865.6
875	955.2	775.5	781.9	775.3	882.0	850.1
876	918.0	720.6	896.4	795.8	801.7	867.1
877	962.6	814.4	912.1	738.0	879.1	876.2
878	815.9	838.1	816.6	829.0	913.7	897.2
879	971.3	775.3	724.1	853.5	945.4	934.5
880	952.1	869.0	735.8	820.7	881.0	885.4
881	912.6	798.2	872.5	773.6	941.2	937.0
882	967.7	873.4	859.6	715.8	1000.4	853.0
883	909.0	790.9	771.7	711.1	917.6	900.4
884	1039.7	827.1	822.7	663.5	888.2	923.9
885	935.7	822.5	810.0	810.2	906.3	903.9
886	993.1	771.8	808.5	809.3	862.9	852.8
887	916.3	905.6	850.3	685.0	934.3	856.5
888	894.8	821.1	829.5	823.7	900.7	844.1
889	845.7	763.5	835.4	833.2	947.8	878.2
890	925.3	799.5	841.3	780.2	885.0	833.8
891	848.7	730.4	937.4	794.4	897.0	812.5
892	985.0	805.5	745.1	692.6	926.0	813.8
893	884.0	706.5	713.8	762.4	891.6	986.1
894	928.8	730.7	931.3	854.4	925.2	908.6
895	907.3	811.4	895.7	734.6	1006.3	817.2
896	902.4	870.0	937.2	756.3	953.5	797.5
897	898.6	816.1	888.4	812.9	974.8	891.3
898	948.6	947.1	787.3	744.1	996.9	896.2
899	854.6	920.2	836.9	745.1	939.5	717.0
900	983.4	724.5	793.9	714.5	1041.1	900.2
901	813.7	803.1	867.1	849.1	967.2	870.1
902	890.5	878.3	879.3	664.0	964.0	905.4
903	888.7	888.4	906.2	663.5	960.1	779.0
904	951.0	798.1	841.0	765.8	1086.5	838.0
905	966.0	875.6	812.4	794.6	868.3	899.2
906	852.4	804.8	869.8	782.7	885.2	900.4
907	939.2	849.3	839.8	787.8	897.7	744.2
908	895.1	880.8	797.8	750.7	928.9	824.9

cycle	Cylinder 1	Cylinder 2	Cylinder 3	Cylinder 4	Cylinder 5	Cylinder 6
909	935.8	805.5	842.7	779.5	983.4	981.2
910	1026.8	846.9	813.4	710.9	995.9	838.2
911	967.8	881.7	911.6	873.0	1021.2	878.2
912	933.7	855.2	909.1	832.0	963.8	928.8
913	866.0	870.0	827.8	804.4	1063.0	846.4
914	1024.8	865.4	916.9	836.9	986.1	898.7
915	996.9	822.2	962.8	830.3	921.6	971.3
916	916.7	861.3	851.5	866.6	1051.2	913.3
917	915.2	875.5	950.4	823.4	1017.1	883.6
918	963.3	780.3	876.2	807.6	927.4	853.0
919	970.7	832.5	962.8	803.7	956.7	940.4
920	903.0	850.9	867.9	756.5	881.8	863.2
921	988.5	780.5	839.3	862.7	994.7	898.2
922	956.0	882.7	855.7	844.7	882.8	982.4
923	997.2	876.2	895.9	804.4	1011.2	949.3
924	849.6	885.9	936.0	831.7	1017.5	937.2
925	958.6	832.6	953.1	860.8	985.6	988.6
926	1019.2	812.7	828.8	833.4	920.6	880.9
927	1029.3	863.8	967.2	820.5	957.2	931.8
928	1009.5	804.8	940.6	768.7	958.4	885.1
929	967.2	894.2	772.9	855.2	992.0	853.5
930	989.3	723.3	827.1	847.8	947.1	833.0
931	812.4	898.4	767.3	879.1	980.2	993.7
932	999.2	889.7	863.2	850.8	977.5	867.3
933	940.4	840.9	807.6	838.3	945.6	925.1
934	939.7	814.7	827.1	976.8	949.3	802.4
935	947.5	835.6	869.1	796.1	983.7	841.9
936	1002.7	877.6	996.0	801.5	919.6	889.1
937	968.0	887.2	901.3	826.8	886.4	936.7
938	958.6	748.3	895.0	804.9	879.8	977.7
939	910.8	930.2	803.4	878.6	974.8	898.2
940	973.4	817.2	962.1	837.6	990.5	862.9
941	979.0	864.0	806.8	680.1	934.8	863.9
942	990.0	901.8	829.8	741.2	928.9	945.4
943	880.7	812.1	905.9	749.9	931.1	963.1
944	904.0	876.9	912.3	698.4	878.1	922.9
945	966.5	862.6	862.7	776.8	945.9	901.7
946	975.0	780.1	820.3	780.2	790.2	949.8
947	933.1	795.7	859.3	767.3	996.4	843.6
948	1010.4	797.2	850.3	723.1	939.2	918.5
949	1006.4	785.3	908.6	693.8	923.5	885.9
950	964.7	883.7	860.1	809.3	943.9	796.0
951	892.6	795.5	905.0	771.7	923.3	918.0
952	904.7	891.0	892.0	853.9	875.6	918.0
953	965.4	855.7	805.4	805.4	980.5	914.3
954	912.2	778.6	846.9	875.7	785.0	884.4
955	953.2	792.0	913.3	826.8	912.0	905.9
956	944.7	869.2	879.3	845.2	844.5	939.7
957	894.5	765.9	847.6	707.0	877.4	888.3
958	892.1	862.6	809.8	757.5	880.8	854.3
959	922.3	807.2	790.2	734.6	1006.5	892.5
960	866.3	916.0	868.8	703.3	917.4	853.0
961	923.2	805.1	822.5	771.9	892.1	856.0
962	937.0	821.1	855.2	837.8	875.4	853.0
963	837.7	920.2	791.9	841.7	954.9	849.1
964	999.1	751.8	804.9	765.8	900.7	817.5
965	925.3	788.0	850.3	778.5	847.9	871.1
966	903.7	797.2	850.3	734.3	869.5	873.3

cycle	Cylinder 1	Cylinder 2	Cylinder 3	Cylinder 4	Cylinder 5	Cylinder 6
967	925.7	878.9	866.6	842.0	918.1	867.6
968	935.5	829.4	826.4	803.7	850.1	762.2
969	858.2	801.7	800.2	708.7	883.3	859.4
970	931.0	813.0	729.7	697.5	912.5	901.4
971	850.9	837.8	985.8	698.7	936.3	922.4
972	881.1	895.8	900.6	837.3	913.4	814.0
973	918.2	810.6	714.1	697.5	1012.9	947.6
974	962.6	819.3	882.0	793.9	952.0	808.1
975	910.7	786.5	823.2	779.0	1004.3	896.0
976	880.7	800.3	885.7	845.4	992.3	928.1
977	1031.1	687.1	825.4	719.4	961.1	959.9
978	852.4	819.3	891.3	695.3	992.5	890.1
979	903.1	864.8	852.7	793.4	1009.0	907.6
980	927.9	751.0	879.6	744.8	927.0	828.8
981	994.1	801.7	824.7	756.0	986.4	932.5
982	930.6	898.9	843.7	727.0	853.1	912.0
983	967.8	872.7	813.4	720.9	1084.3	924.6
984	966.5	804.4	937.2	908.1	1034.0	943.1
985	1042.9	918.8	820.3	857.9	937.3	889.3
986	1024.6	969.2	819.0	867.4	1029.3	863.4
987	906.1	804.9	1013.6	879.8	920.6	884.9
988	937.1	905.6	823.2	871.8	983.7	913.8
989	913.7	865.9	981.6	750.9	1000.4	839.9
990	1025.0	831.4	942.6	856.4	978.3	914.5
991	957.4	808.0	907.9	830.8	878.1	828.6
992	931.6	856.0	857.9	695.5	946.3	975.7
993	955.8	928.0	914.7	758.0	1002.8	947.1
994	931.5	935.9	962.6	856.6	1006.7	959.9
995	958.6	990.4	902.5	728.5	1032.8	921.4
996	939.2	789.0	861.3	831.2	1052.7	894.0
997	990.1	816.1	844.9	889.3	979.0	1006.6
998	965.1	887.6	880.8	750.9	1158.2	896.2
999	969.1	855.0	896.9	862.2	933.1	873.3
1000	983.3	818.4	985.1	879.3	1023.2	905.9

10/10/10